Electronic and vibrational properties of low-dimensional carbon systems

vorgelegt von
Diplom-Physiker
Patrick May
aus Albstadt-Ebingen

Von der Fakultät II - Mathematik und Naturwissenschaften
der Technischen Universität Berlin
zur Erlangung des akademischen Grades

Doktor der Naturwissenschaften
– Dr. rer.nat. –

genehmigte Dissertation

Promotionsausschuss:

Vorsitzender:	Prof. Dr. Michael Lehmann
Berichter:	Prof. Dr. Janina Maultzsch
	Prof. Dr. Konstantinos Papagelis

Tag der wissenschaftlichen Aussprache: 14.2.2012

Berlin 2012
D 83

Zusammenfassung – German abstract

Die vorliegende Dissertation untersucht mittels inelastischer Lichtstreuung sowohl die elektronische Struktur als auch die Schwingungseigenschaften von unterschiedlichen Kohlenstoffsystemen.
Die Dissertationsarbeit besteht aus zwei Teilen.
Der erste Teil befasst sich mit der Frage, inwieweit korrelierte Elektron-Loch Paare, sogenannte Exzitonen in ein-dimensionalen metallischen Kohlenstoffnanoröhren existieren. Exzitonen bestimmen die optischen Eigenschaften eines Systems, vor allem die Absorption und Emission, aber auch die Linienbreite sowie strahlende und nichtstrahlende Lebensdauern. Für gewöhnlich wird die Entstehung von Exzitonen in metallischen drei-dimensionalen Festkörpern auf Grund der Coulomb-Abschirmung verhindert. Diese Abschirmung ist stark reduziert in niedrigeren Dimensionen. Theoretische Rechnungen sagen eine Bindungsenergie von 50 - 100 meV voraus, folglich werden die optischen Übergänge selbst bei Raumtemperatur durch Exzitonen bestimmt. Mittels resonanter Raman Streuung kann der optische Übergang von spezifischen Kohlenstoffnanoröhren, insbesondere auch in einem Ensemble von unterschiedlichen Chiralitäten, bestimmt und einzelne Chiralitäten können unterschieden werden.
Der optische Übergang wurde als Funktion der Temperatur in einem Bereich von 300 bis 800 Kelvin für metallische und halbleitende Kohlenstoffröhren gemessen. Die Abhängigkeit des optischen Übergangs von der Temperatur ist unterschiedlich. Bei einer Temperatur, die der thermischen Energie der Exzitonen entspricht, konnte bei der metallischen Kohlenstoffröhre eine plötzliche Änderung der Übergangsenergie hin zu höheren Energien gemessen werden, während die halbleitende diese Änderung nicht aufweist. Dies erklärt sich dadurch, dass die thermische Energie zur Dissoziation der Exzitonen führt und folglich die exzitonische Oszillatorstärke vom Exziton in einen quasi Band-zu-Band Übergang übergeht. Es konnte nachgewiesen werden, dass die Bindungsenergie der korrelierten Elektron-Loch Paare in der Größenordnung von 50 meV liegt. Die Interpretation konnte weiterhin dadurch bekräftigt werden, dass die Ramanintensität beim Übergang vom exzitonischen zum Band-zu-Band stark einbricht.
Der zweite Teil der Arbeit beschäftigt sich mit Streuprozessen auf mikroskopischer Ebene der doppelresonanten Raman Streuung. Aufgrund der Impulserhaltung tragen üblicherweise nur Phononen am Γ Punkt zum Raman Streuprozess bei. Bei der Doppelresonanz, einem Raman Prozess zweiter Ordnung, hingegen tragen Phononen aus der ganzen Brillouin-Zone bei. Phononen, welche die Bedingung für die Doppelresonanz erfüllen, tragen hierzu verstärkt bei. Durch Variation der Anregungswellenlänge ändern sich die Bedingungen für die Doppelresonanz, weshalb andere Phononen beteiligt werden und folglich der Raman Peak seine Frequenz ändert. Somit lässt sich die Phononendispersion messen, sofern ausreichende Kenntnisse über die elektronische Struktur und die Streuprozesse auf mikroskopischer Ebene bekannt sind. Charakteristisch ist die sogenannte $2D$ Mode, die das Spektrum im Graphene dominiert

und sich auch zur Bestimmung der Anzahl der Atomlagen nutzen lässt. Allerdings sind die relevanten Streuprozesse, die zu dieser Mode beitragen derzeit in der Diskussion. Um die relevanten Streuprozesse herauszufinden eignen sich Methoden wie z.B. 'Strain'. Hier konnte in Experimenten und theoretischen Rechnungen aufgezeigt werden, dass die Streuprozesse aus unterschiedlichen Richtungen in der Brillouinzone stammen. Man unterscheidet hier zwischen *äußeren* Prozessen, bei denen die Elektronen zwischen dem Γ Punkt und dem K Punkt, und *inneren* Prozessen, bei denen die Elektronen zwischen dem M Punkt und dem K Punkt angeregt werden.
Zuerst werden die Beiträge der $2D$ Mode in freistehendem zweilagigem Graphen (sog. bilayer graphene) untersucht. Im Gegensatz zu 'Strain' Experimenten an Graphen wird hierbei hauptsächlich die elektronische Struktur verändert. Dies lässt sich auf die Kopplung der beiden Lagen zurückführen, die zu einer Aufspaltung der elektronischen Bänder führt. Es werden die Raman Frequenzen berechnet und mit dem Experiment verglichen. Darüber hinaus werden die Raman Spektren explizit ausgerechnet. Die relative Raman Intensität der unterschiedlichen Beiträge wird in Hinblick auf Elektron-Photon und Elektron-Phonon Matrixelemente diskutiert und es wird gezeigt, dass eine Reduzierung der Streuprozesse auf eine Dimension sowohl eine sehr gute Übereinstimmung der Frequenzen bringt, als auch die relativen Intensitäten reproduzieren kann. Eine anschließende kurze Betrachtung der Streuprozesse in zwei Dimensionen befasst sich mit den Begriffen des *innereren* und *äußereren* Prozesses und inwieweit sich die Begrifflichkeiten auf zwei Dimensionen ausweiten lassen. Es kann gezeigt und argumentiert werden, dass die gängige Notation unter bestimmten Voraussetzungen beibehalten werden kann.
Es wird schließlich noch eine Kombinationsmode untersucht, die sich aus einem transversal optischen (TO) und einem longitudinal akustischen (LA) Phonon zusammensetzt. Diese doppel-resonante Mode wurde in der Literatur bislang wenig untersucht. Es werden Raman Messungen an Graphene, Bilayer-Graphene und Graphite mit theoretischen Berechnungen verglichen. Aufgrund der Dispersion dieser Raman Mode kann sie eindeutig einem *inneren* Prozess zugeordnet werden, so dass hier gezeigt werden konnte, dass $innere$ Prozesse zum Raman Spektrum beitragen. Zudem ist diese Mode die einzige im Spektrum, die eine starke Asymmetrie zu höheren Frequenzen aufweist. Zudem nimmt die Raman Intensität stark ab. Die Asymmetrie lässt sich durch die Winkelabhängigkeit der LA Phononendispersion in der zweidimensionalen Brillouinzone erklären. Durch eine sorgfältige Analyse der Asymmetrie konnten die beteiligten Phononen in der zweidimensionalen Brillouinzone ermittelt werden. Die abklingende Intensität ist in Einklang mit der Winkelabhängigkeit des optischen Matrixelements. Hier konnte gezeigt werden, dass der Hauptbeitrag von *inneren* Prozessen aus der Hochsymmetrie-Richtung stammt. Die eindimensionale Betrachtung wird schließlich noch auf Graphit angewandt. Hier konnte die LA Phononendispersion gemessen werden. Die Dispersion der $2D$ Mode bei Anregungsenergien im UV wird danach betrachtet und ein-dimensionale Rechnungen werden mit experimentellen Daten verglichen.

Abstract

The present thesis studies the electronic and vibrational properties of carbon systems with inelastic light scattering. The work comprises two parts.
The first part addresses the question of the existence of correlated electron-hole pairs, so-called excitons, in metallic single-walled carbon nanotubes. Optical properties such as absorption, emission, the linewidth and radiative and non-radiative lifetimes are determined by excitons. However, excitons are expected to be prevented in metallic systems due to Coulomb screening at the Fermi level. However, this screening is strongly suppressed in lower dimensions such as the one-dimensional carbon nanotubes and excitonic binding energies on the order of 50 - 100 meV have been predicted. Here, the excitonic binding energy of metallic single-walled carbon nanotubes is measured with temperature-dependent resonant Raman spectroscopy. By changing the temperature in the range of 300-870 K, variations in the optical transition energy E_{ii} are observed between metallic and semiconducting nanotubes.
Both dependences are found to be different for semiconducting and metallic single-walled carbon nanotubes. This behavior is explained in terms of excitons dissociated into free electron-hole pairs at temperatures related to the exciton binding energy. The excitonic oscillator strength is transferred back to the band-edge and thus the optical transition is determined by a quasi band-to-band transition. The exciton binding energy was derived and found to be on the order of 50 meV for the metallic nanotube. The interpretation is further supported by the observation of a stronger temperature-induced decrease in the Raman scattering efficiency in case of the metallic nanotube compared to the semiconducting tube.
The second part addresses the question of scattering paths contributing to the double-resonant process. Due to momentum conservation only Γ point phonons contribute to the Raman spectrum. Double-resonant Raman scattering provides a powerful technique for probing the phonon dispersion of graphene and related systems. The double-resonant process, however, permits that phonons from the entire Brillouin zone contribute to the Raman spectrum. Double-resonant processes that satisfy the double-resonant condition are enhanced. By tuning the excitation energy this condition alters and changes the contributing phonons and hence the Raman frequency. An understanding of the scattering paths is essential, since by Raman spectroscopy it is possible to probe both the electronic structure and phonon dispersion. However, the contributing processes are under recent discussion. The dominant Raman feature is the so-called $2D$ mode, which also allows the determination of the number of graphene layers. Theoretical and experimental studies of strain in graphene gave first evidences for the contribution of phonons stemming from different sides of the K point. So-called $inner$ and $outer$ processes were distinguished. $Inner$ processes refer to the excitation of electrons between the K and M-point, whereas $outer$ processes refer to the electronic excitation of electrons between the Γ and K-point.

First, the double-resonant process is investigated in free-standing bilayer graphene. In contrast to strain experiments, mainly the electronic structure is changed in bilayer graphene. This is a consequence of the coupling between the two layers, which results in a splitting of the electronic bands. Experimental results are combined with a one-dimensional calculation along the high-symmetry line. Different scenarios of double-resonant scattering paths are probed, and a combination of both $inner$ and $outer$ processes is found to reproduce the experimental data very well. The Raman spectrum for different excitation energies is calculated and it is shown that a reduction of the double-resonant process in one-dimension provides very good agreement with the experiment. The relative intensities of the $2D$ mode is discussed in terms of electron-phonon and optical matrix elements. A brief consideration towards a two-dimensional calculation of the scattering processes indicate that the terms of $inner$ and $outer$ processes is not uniquely determined but can be maintained under certain aspects.
Then a double-resonant combination mode consisting of a transverse (TO) optical and a longitudinal acoustic (LA) phonon is investigated. By analyzing the dispersion, this mode is assigned to an $inner$ process. Further, the asymmetric lineshape is found to be a direct consequence of the strong angular dependence of the LA phonon branch. It is shown that the main contribution is due to a scattering process along the high-symmetry line. The decrease in intensity towards higher frequencies is explained by the angular dependence of the optical matrix element. The one-dimensional scattering paths of the double-resonance is then applied to graphite. Here the LA phonon dispersion is monitored by an analysis of the $2D$ and TO + LA mode.
The progress of the $2D$ mode towards the ultraviolet (UV) region is studied afterwards in graphene by means of a one-dimensional calculation and experimental data of graphene and graphite.

List of publications

Parts of the thesis have already been published:

1. F. Herziger, P. May, and J. Maultzsch
   Layer number determination in graphene by out-of-plane vibrations
   arXiv:1203.6043 (2012)

2. P. May, H. Telg, G. Zhong, J. Robertson, C. Thomsen, and J. Maultzsch
   Observation of excitons in metallic carbon nanotubes
   Phys. Rev. B **82**, 195412 (2010)

3. P. May, H. Telg, C. Thomsen, and J. Maultzsch
   Temperature dependent band gap behavior and excitons in metallic carbon nanotubes
   pss(b) **1-4**, 195412 (2010)

4. P. May, F. Herziger, F. Kadis, B. Mukhopadhyay, E. Malic, M. Mohr, and J. Maultzsch
   Double-resonant Raman scattering in free-standing bilayer graphene
   in prepration based on chapter 5.2

5. P. May, F. Herziger, and J. Maultzsch
   Origin of the TO and LA double-resonant Raman mode
   in preparation based on chapter 5.3

Contents

1 Introduction

Electronic and vibrational properties of carbon materials have been the focus of intense theoretical and experimental research [1, 2]. This interest has intensified since the discovery of graphene in 2004 [3].
The electronic properties of graphene are derived from graphite, whose electronic properties have been studied for decades. Graphite has been variously used as lubricants in the steel industry and in every day common use tools such as pencils. The theoretical description of the electronic bandstructure was first reported by P.R. Wallace in 1947 [4], which studied the electronic bandstructure in the Brillouin zone for a single hexagonal layer of graphite. Knowledge concerning the electronic bandstructure of graphite is useful as it can be applied to other carbon systems such as fullerenes, carbon nanotubes and other nano-carbon systems. Fullerenes were discovered in 1985 [5] and are classified as zero-dimensional systems. This discovery was the first important step in the breakthrough of carbon nanotechnology. Soon afterwards in the early 90´s single-walled carbon nanotubes were discovered by Iijima [6, 7].
Single-walled carbon nanotubes (SWCNT) belong to the most interesting and often investigated one-dimensional materials studied today as they exhibit exciting physical phenomena such as ballistic transport of electrons, high tensile strength and outstanding heat conduction [8,9]. Carbon nanotubes can also sustain high electronic currents and the scattering mean free path of the electrons is on the order of micrometers [10]. The beauty of carbon nanotubes lies in their geometry, which determines their electronic structure. By controlling the geometry or in other words depending on how the graphene sheet is rolled up, the electronic structure exhibits either a metallic or a semiconducting character; different chiralities yield different sized bandgaps. A variety of optoelectronic applications, such as nanoscale field effect transistors, electrically excited single-molecule light sources and nano sensors are promising [11–14]. Bound electron-hole pairs, known as excitons, determine the excited states within carbon nanotubes. Excited states can be either created by optical or electrical means [15]. These excited states are sensitive to its dielectric environment due to their single-atomic structure and permits so-called bandgap engineering.
Furthermore graphene is a single atomic plane of carbon atoms arranged in a hexagonal lattice. This two-dimensional form of carbon in a sp^2 configuration remained undiscovered until 2004 [3]. The discovery has attracted significant attention, due to the unique material properties of graphene [3, 16] which exhibits record values for thermal room-temperature conductivity ($\approx 5000\,\mathrm{W\,m^{-1}\,K^{-1}}$) [17], a breaking strength of ≈ 42 N/m, high Young's modulus of ≈ 1.0 TPa [18] and high electron mobilities of $15\,000\,\mathrm{cm^2\,V^{-1}s^{-1}}$ under ambient conditions [19]. The transport properties are sensitive to charged impurities introduced by the substrate [20], graphene without substrate-induced perturbations leads to improvements in device quality and electron mobilities exceeding $200\,000\,\mathrm{cm^2\,V^{-1}s^{-1}}$ [21–24].

Andre Geim and Konstantin Novoselov were awarded with the Nobel Prize in Physics in 2010 for "groundbreaking experiments regarding the two-dimensional material graphene" [25]. Graphene closed the gap between all other dimensions and is a semi-metal or zero-gap semiconductor and electronically behaves as a two-dimensional electron gas, which is described by the Dirac equation. This permits the investigation of phenomena related to quantum electrodynamics (QED). The material exhibits a number of unusual and exciting behaviors, such as the anomalous integer quantum Hall effect and Klein tunneling [26, 27].

The unusual electronic structure of graphene with its linear dispersion relation gives it exceptionally good transport properties, which in turn paves the way for applications such as integrated circuits, field-effect transistors (FETs) and chemical sensors. The integration of graphene in electronic circuits is one of the applications, which is followed up the most [28]. However, low ON/OFF ratios present issues that need to be overcome in order to use graphene in a field-effect transistor [29].

Stacking two layers of graphene on top of each other gives bilayer graphene. The bandstructure of bilayer graphene can be described by a zero-gap parabolic equation. It has been shown that by applying an electric field perpendicular to the graphene plane, a bandgap can be opened and even tuned [30]. Further, recent results showed evidence for light-plasmon coupling at terahertz frequencies [31]. This could lead to development of graphene-based metamaterials in the infrared regime [32].

The physical properties and the resulting application of graphene and carbon nanotubes are strongly related.

As outlined above, carbon materials exhibit a number of exciting electronic and vibrational properties.

Raman spectroscopy provides access to both the electronic and vibrational properties and has been widely used for the characterization of nanomaterials in the last decades. It is a powerful technique for monitoring strain [33–36], disorder [37], environmental [38, 39] and magnetic effects [40], functionalization and therefore charge transport phenomena [41] and diameter [42, 43] and many-body effects [44] in the case of carbon nanotubes.

Concerning many-body effects, one-dimensional carbon nanotubes have been predicted to show strong electron-hole interactions, so-called excitons. Excitons are already well understood from their usage in classical semiconductors. In semiconducting nanotubes, however, the binding energy is at least one order of magnitude stronger than in bulk materials. In general, metallic systems exhibit a very effective screening of the actual Coulomb interaction by free carriers. In lower dimensions, on the other hand, this screening is reduced and optical transitions in metallic carbon nanotubes produce excitons even at room temperature. In this work, temperature-dependent Raman scattering is applied for the determination of the exciton binding energy. The value of the exciton binding energy is approximately $50\,\mathrm{meV}$, which is in very close agreement to theoretical predictions.

Double-resonant Raman scattering permits scanning of both the electronic structure and phonon dispersion due to the contribution of large phonon wave vectors $\mathbf{q}$. In contrast to single-resonances, double-resonances mean that both the excited and scattered phonon make a real transition. By changing the excitation energy, the condition that satisfies the double-resonance alters and permits scanning of the

phonon dispersion on both sides of the K point. To achieve this requires a fundamental understanding of contributing scattering paths. In this work, the dominant scattering paths are investigated by means of so-called *inner* and *outer* processes referring to electronic excitations on different sides of the K point in the Brillouin zone.

The work is organized as follows. In Chapter 2 the fundamental properties of carbon materials are described. The understanding of electronic and vibrational properties is essential for the inelastic light scattering that will be introduced in Chapter 3. Here, also electron-photon and electron-phonon coupling are briefly introduced. Chapter 4 is devoted to the concept of excitons and the determination of the excitonic binding energy in metallic carbon nanotubes.

Scattering paths within the double-resonant process are addressed in Chapter 5; the double-resonant $2D$ mode of free-standing bilayer graphene is investigated and contributions from both sides of the K point are needed to explain the different intensities. The contribution of scattering paths of the entire Brillouin zone can be resolved with the TO + LA combination mode. Here, the dominant scattering paths can be directly extracted from the Raman spectrum. When progressing towards the ultraviolet (UV), the linear shift rate of the $2D$ mode changes and exhibits an exponentially progress which underlines the importance of so-called $inner$ processes.

2 Basic properties of carbon materials

In this chapter the electronic and vibrational properties of graphene and carbon systems that relate to this thesis will be reviewed. Concepts and ideas needed to contribute to an understanding of inelastic light scattering in carbon materials will be introduced. For a further and more detailed discussion the reader is directed to recent books by Reich *et al.* [1] and Jorio *et al.* [2] and the following review articles [45–48].

2.1 Graphene

Graphene has attracted substantial interest since its discovery in 2004 due to its unique material properties [3, 16]. For many years it was not believed to exist due to missing long-range order in two-dimensional systems [49–51]. The existence of graphene is explained due to finite-sized ripple formation [21, 52, 53].

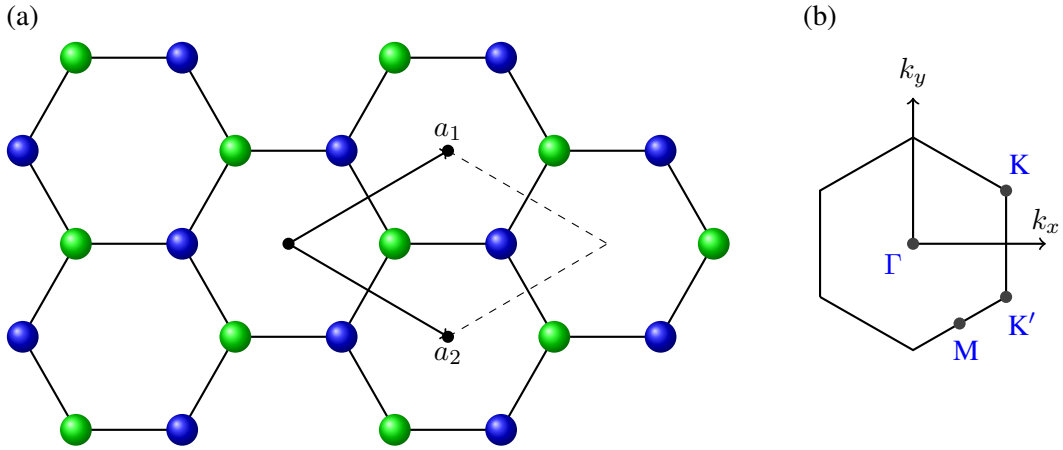

Figure 2.1: (a) Crystallographic structure of single layer graphene with the atoms of different sublattices marked with different colors. Unit cell of graphene with lattice vectors $\vec{a}_1$ and $\vec{a}_2$. (b) Brillouin zone of graphene with high symmetry points. The Γ point is in the zone center, the M point in the middle of two connecting hexagonal sides and the K and K' points are at the corners.

Figure 2.1 (a) shows the crystallographic structure of grahene including the unit cell with lattice vectors $\vec{a}_1$ and $\vec{a}_2$. The unit cell contains two atoms and the carbon-carbon distance is $a_{cc} = 1.422\,\text{Å}$. The two adjacent carbon atoms have strong covalent bonds. Three-dimensional graphite is obtained by the stacking of the hexagonal networks of individual graphene layers along the direction, perpendicular to the graphene layer. The stacking is usually an AB or so-called Bernal stacking, where atoms A are above each other and atom B is displaced with respect to each other as depicted in Fig. 2.4 (a). In Fig. 2.1 (b)

the high symmetry points in the Brillouin zone are shown. The Γ point is in the zone center, the M point in the middle of two connecting hexagonal sides and the K and K' points are at the corners. They are inequivalent since there is no reciprocal vector that connects them.
The electronic structure can be derived from the following expression [16]:

$$E_{\pm}(\mathbf{k}) = \pm\, t\, \sqrt{3 + f(\mathbf{k})}\; - t' f(\mathbf{k}), \tag{2.1}$$

with:

$$f(\mathbf{k}) = 2\cos(\sqrt{3}k_y a) + 4\cos\left(\frac{\sqrt{3}}{2}k_y a\right)\cos\left(\frac{3}{2}k_x a\right), \tag{2.2}$$

t is on the order of 2.8 eV and denotes the nearest-neighbor hopping energy between different sublattices and t' is the nearest-neighbor hopping energy in the same sublattice. The π^* bands are obtained by applying the plus sign and the π is obtained by applying the minus sign.

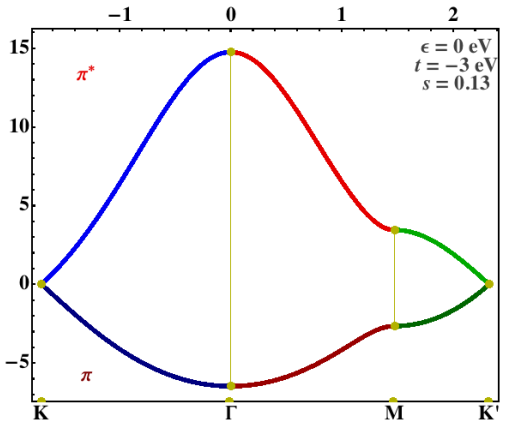

Figure 2.2: Energy dispersion along the high-symmetry direction K-Γ-M-K' obtained from Eq. 2.1 and 2.2. The notation of the high symmetry points is adopted from Graphite.

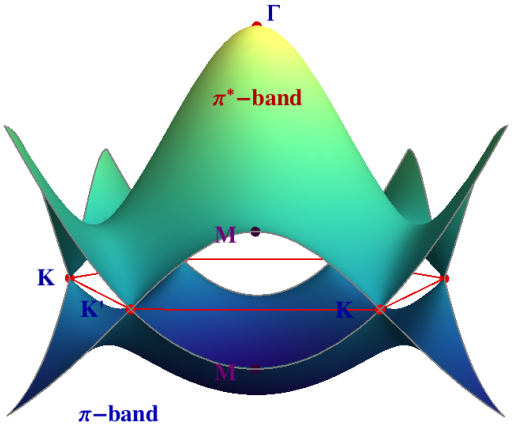

Figure 2.3: Energy dispersion relation for graphene in a three-dimensional contour plot obtained from Eq. 2.1 and 2.2. The valence and conduction band touch at high symmetry points K and K'.

Figure 2.2 shows the electronic energy dispersion along the high-symmetry direction K-Γ-M-K' and Fig. 2.3 depicts the three-dimensional contour plot. The metallic behavior of graphene is due to a crossing of the valence and conduction bands at the six corners of the hexagon referred to as K and K' points. In the vicinity of these points, the bandstructure exhibits an approximately linear energy dispersion. Thus, the electrons follow the Dirac equation at low wave vectors.
The electronic bandstructure is changing when additional graphene layers are added as in the case of bilayer graphene, which consists of two layers of graphene mostly arranged in the so-called Bernal-stacking (AB-stacking) [54]. The π orbitals in the visible energy range give rise to four bands (two valence and two conduction bands) close to the Fermi level, denoted as π_1, π_2 and π_1^*, π_2^*. The π_1

valence band and the π_1^* conduction band touch at the K point.

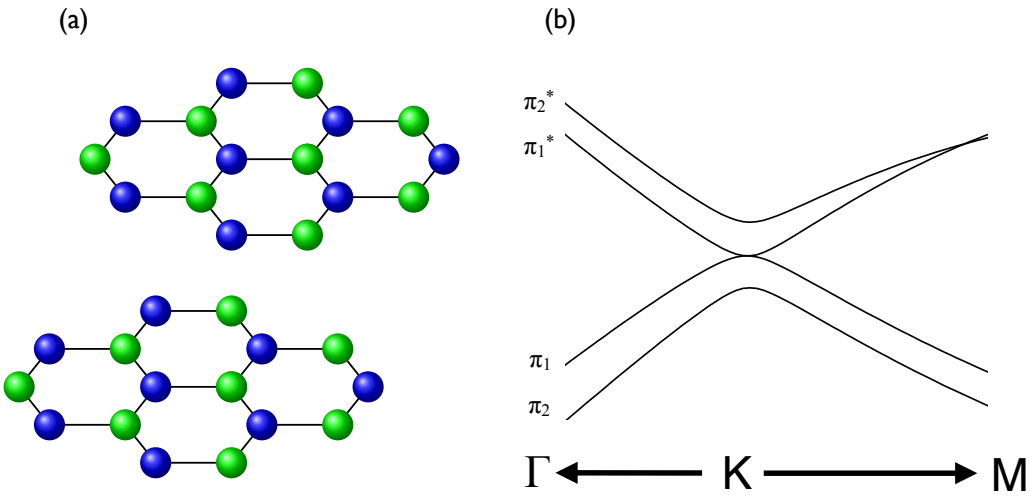

Figure 2.4: (a) Two layers of graphene in the so-called Bernal stacking which form bilayer graphene. A (green balls) and B (blue balls) atoms are above each other. (b) Bilayer graphene electron dispersion near the K point calculated with the *ab initio* QUANTUM-ESPRESSO code [55]

To analyze the Raman spectra it is essential to understand the phonon dispersion. The graphene unit cell contains two atoms and therefore six phonon branches separated in three optical (O) and three acoustic (A) branches are available. The space group of graphene is $P6/mmm$ in the Hermann-Mauguin or D_{6h} in the Schönfliess notation.

Figure 2.5 shows the corresponding phonon dispersion along the high-symmetry lines. The ZA mode is an out-of-plane acoustic mode, the TA mode is an in-plane acoustic mode, which is sometimes called SH mode (shear). The LA and LO branch is the longitudinal acoustic and optical mode, respectively. ZO and TO are out-of-plane and in-plane optical modes, respectively. Since the in-plane carbon atoms bonds are much stronger than the interlayer van-der-Waals interaction, it can be assumed that phonon modes of graphite are similar to that of graphene. The only difference is that the phonon modes split into in-phase and out-of-phase vibrations due to stacking of graphene layers. Especially for optical modes this difference is negligible small. At the Γ point, the TO and LO modes are degenerate belonging to the two-dimensional E_{2g} representation. The optical Γ-point zone center phonons are Γ = B_{2g} + E_{2g} and only the E_{2g} phonon is Raman active. It corresponds to vibrations of two sublattices against each other. This degeneracy is lifted for single-walled carbon nanotubes or by applying uniaxial strain to graphene. The TO phonon branch is of great importance in the vicinity of the K point, since the D and $2D$ Raman modes are related to this phonon branch (see below) [56].

The acoustic modes are decomposed into Γ = A_{2u} + E_{1u} [57]. When adding more layers to graphene,

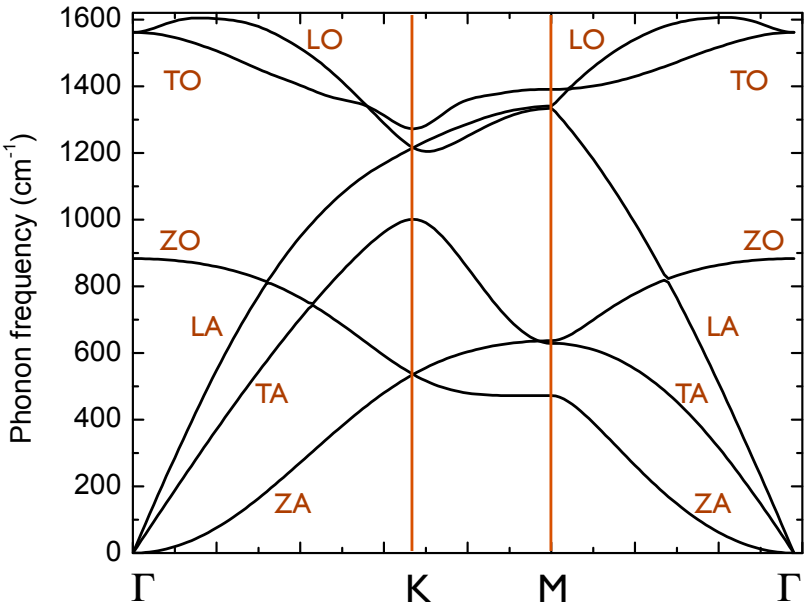

Figure 2.5: Phonon dispersion of graphene showing different phonon branches, derived with the *ab initio* QUANTUM-ESPRESSO code [55].

the acoustic phonon splits in one in-phase and one out-of-phase phonon. The out-of-phase phonon is observable and its frequency is around ≈ 40 cm^{-1} [58].

A Raman spectrum of graphene obtained at 2.33 eV excitation energy is depicted in Fig. 2.6. The so-called G mode stems from the Γ. The other modes stem from the vicinity of the K point and are activated due to the double-resonant process, which will be explained in the next chapter. The D mode with a frequency of approximately 1350 cm^{-1}, is activated by defects and provides information about the defect density. A very prominent feature, which is also used to characterize and to distinguish single-layer graphene from few layer graphene, is the $2D$ mode. The intensity is stronger than that of the G mode as a consequence of the double-resonant process and enhanced electron-phonon coupling [56, 59]. The mode in the vicinity 2450 cm^{-1} is also due to a double-resonant process, but involves a transverse optical (TO) and a longitudinal acoustic (LA) mode. This mode is often called G^*, however in this work it is called TO + LA mode. In combination with the $2D$ mode, which is due to two TO phonons, this mode allows to directly probe the LA phonon branch.

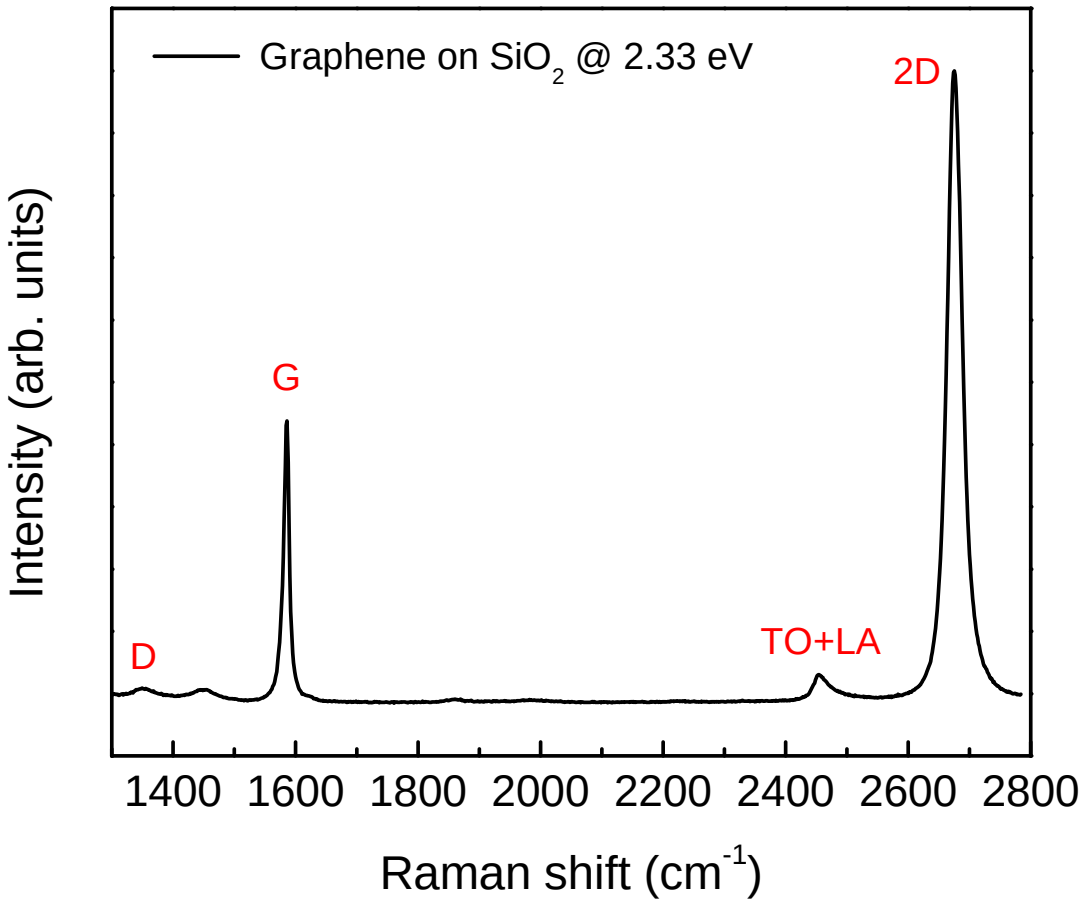

Figure 2.6: Raman spectrum of single layer graphene supported on SiO_2. The spectrum shows several Raman modes. The G (E_{2g}) mode and the $2D$ mode are the best investigated and most prominent features in the spectra of all sp^2 carbons, whereas the G mode is the only phonon stemming from the Γ point. The other features stem from phonons in the vicinity of the K point. The D mode is only activated if defects are present in the sample or near the edges, which can be treated as defects. The TO + LA mode is a combinational mode of the transverse optical (TO) and longitudinal acoustic (LA) phonon branch. It is often referred to as G^* mode.

2.2 Carbon Nanotubes

Carbon nanotubes are seamless cylinders and can be best described as rolled up strips of single or multi-layer graphene, which are then named single-walled or multi-walled carbon nanotubes. Typical diameters of single-walled carbon nanotubes are in the range of one nanometer. Their length can reach up to several micrometers. The ratio of length to diameter determines the treatment as quasi one-dimensional systems. The reduction in phase space due to their one-dimensional nature leads to a confinement of charge carriers, which are consequently only free along the axis of the nanotube. This behavior is interesting with regard to the investigation of physics in one dimension. Carbon nanotubes are versatile materials, since each particular carbon nanotube exhibits a different bandgap and has an explicit relationship between its structure and electronic properties [60]. Further this one-dimensionality leads to the formation of strong bound electron-hole pairs by Coulomb forces. These so called excitons, which will be discussed in Chapter 4, with binding energies of a fraction of eV, are much larger than in semiconducting bulk materials. Depending on the chirality, CNTs are either semiconducting or metallic. And even in metallic nanotubes there is a strong debate about the value of the exciton binding energy, which is expected to change for particular nanotubes and for higher optical transitions [61, 62].
By rolling up graphene into a carbon nanotube, a circumferential vector can be defined. This vector is also called the chiral vector and contains all information for the determination of the microscopic structure of carbon nanotubes. These two quantities are the diameter d and the chiral angle Θ. Fig. 2.7 shows the graphene lattice with chiral vector:

$$\vec{c}_h = n\vec{a}_1 + m\vec{a}_2, \tag{2.3}$$

with graphene lattice vectors $\vec{a}_1$ and $\vec{a}_2$. The diameter of a carbon nanotube can be derived from the length of the chiral vector $\vec{c}_h$

$$d = \frac{|\vec{c}_h|}{\pi} = \frac{a_0}{\pi}\sqrt{N} \tag{2.4}$$

with $N = n^2 + nm + m^2$ and $a_0 = |\vec{a}_1| = |\vec{a}_2| = 0.246$ nm is the graphene lattice constant.
The rolled-up graphene lattice with indices $(6, 1)$ is shown in Fig. 2.8. The indices n and m are used to define any particular single-walled carbon nanotube. There are two characteristic directions in the graphene lattice called armchair and zig-zag. These directions are adapted from the edges of a graphene sheet. Here the chiral angle is of importance and defined as the angle between the chiral vector $\vec{c}_h$ and the zig-zag direction.

$$\Theta = \arccos\frac{\vec{a}_1 \cdot \vec{c}}{|\vec{a}_1| \cdot |\vec{c}|} = \arccos\left(\frac{n + m/2}{\sqrt{N}}\right) \tag{2.5}$$

The indices (n,m) show a strong dependence on the electronic properties, e.g. while the $(12, 0)$ is a metallic nanotube, the $(12, 1)$ is a semiconducting tube with a bandgap E_g of 1.6 eV and the $(12, 2)$ exhibits a bandgap of 0.9 eV [63].

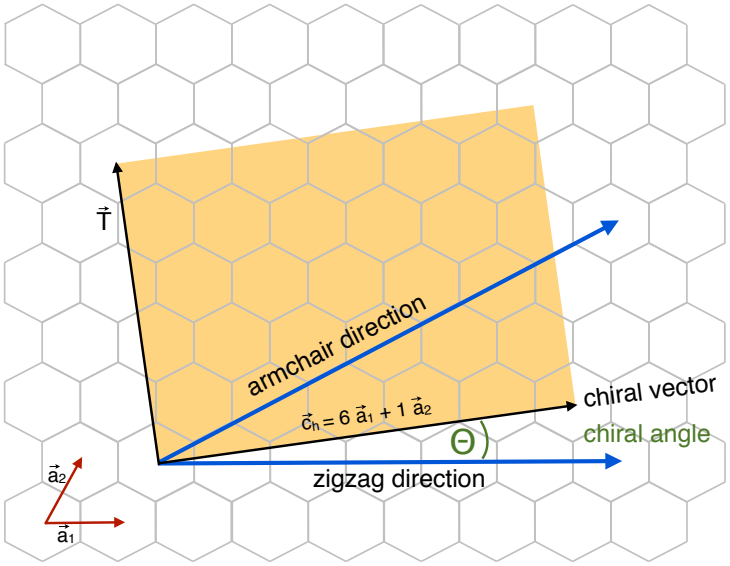

Figure 2.7: Schematic picture of a two-dimensional honeycomb graphene sheet with chiral vector (also referred to as roll-up vector) $\vec{c}_h$, which is decomposed by $\vec{c}_h = n\vec{a}_1 + m\vec{a}_2$ with lattice vectors $\vec{a}_1$ and $\vec{a}_2$. $\vec{T}$ is the basis vector perpendicular to the chiral vector $\vec{c}_h$ and parallel to the tube axis. The limiting case of $(n, 0)$ is called zigzag and (n, n) for $n = m$ is called armchair direction. These two main directions are indicated in blue arrows. The angle between the zigzag direction and the chiral vector is called the chiral angle of the specific nanotube.

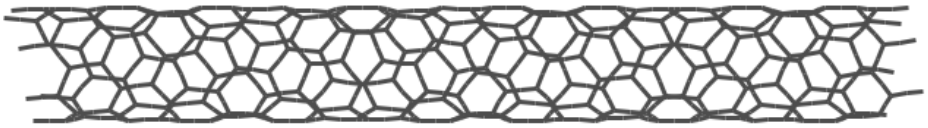

Figure 2.8: The $(6, 1)$ nanotube

In contrast to graphene, the electronic wave function in carbon nanotubes is only free in one dimension, which is along the nanotube axis. In the zone-folding approach one assumes an infinitely long tube, which then has a continuous component of the reciprocal vector along the tube axis $\vec{k}_z$ inducing a continuum of allowed wave vectors. However, along the circumference $\vec{c}_h$ one needs periodic boundary conditions for the wave function, unless they interfere destructively. The necessary boundary condition reads as follows:

$$\vec{c}_h \cdot \vec{k} = 2\,\pi\,m \quad (m \in \mathbb{N}) \tag{2.6}$$

This leads to a quantization of the wave function in the circumferential direction resulting in lines of allowed **k** values in the graphene **k** space with a distance depending on $|\vec{c}_h|$. These so-called cutting lines are shown in Fig. 2.9. The figure shows the two-dimensional Brillouin zone of graphene with the allowed **k** values for one metallic and one semiconducting nanotube. Each nanotube has a certain set of **k** states. The relative position of the K point to the allowed states determines whether the nanotube exhibits metallic or semiconducting character. On the right hand side the corresponding bandstructure of the particular nanotube is shown. The bandstructure was obtained by the zone-folding approximation on the basis of the tight-binding model. The semiconducting nanotubes exhibits a bandgap. There is an easy way for the determination of whether a nanotube exhibits metallic or semiconducting character. One defines ν, which is also called the family index as:

$$\nu = (n - m) \bmod 3, \tag{2.7}$$

where mod 3 is the modulus of 3. It follows that ν can only be -1, $+1$ or 0. The nanotubes is metallic, if $\nu = 0$, otherwise it is semiconducting.

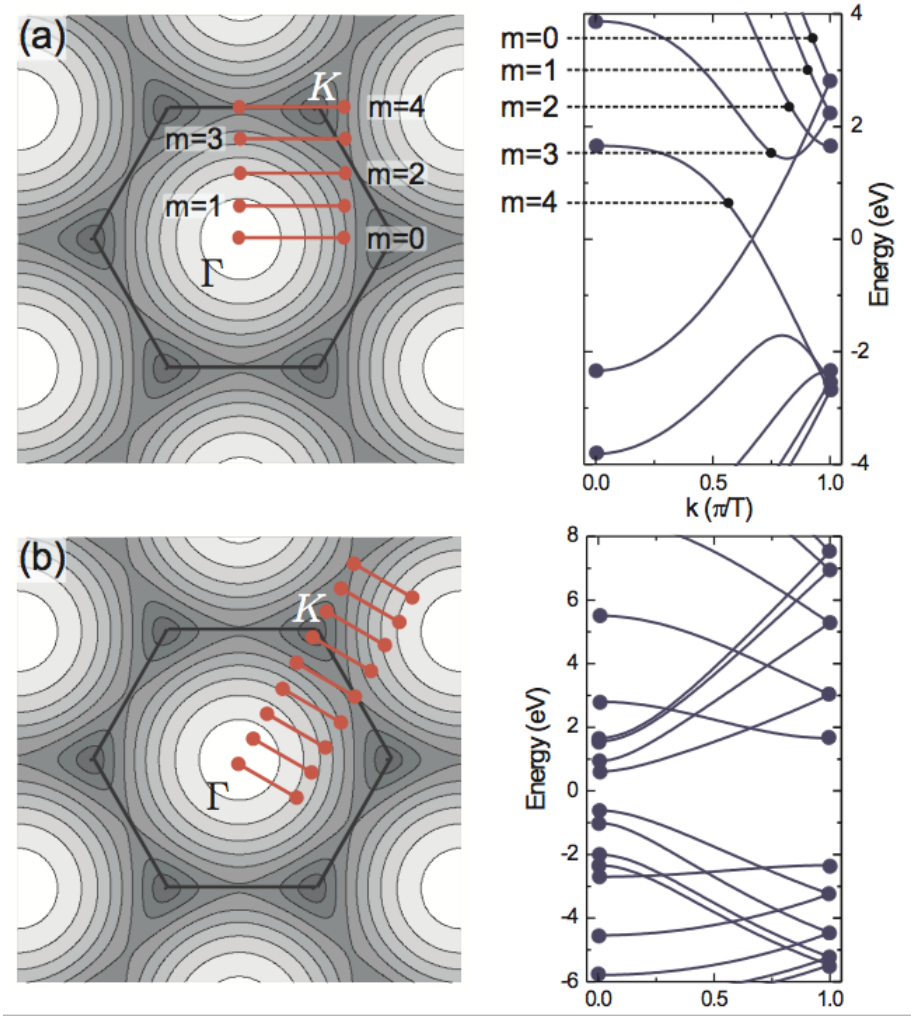

Figure 2.9: Two-dimensional Brillouin zone of graphene with the allowed **k** values for two different nanotubes on the left and the corresponding bandstructure of the particular nanotube on the right hand side. Figure (a) represents the (4,4) armchair nanotube, which is metallic and a consequence of the crossing valence and conduction band. Figure (b) is for the (8,0) zig-zag nanotube. This nanotube exhibits semiconducting behavior as a consequence of a bandgap. Image courtesy of Janina Maultzsch.

3 Introduction to inelastic light scattering

This chapter gives a brief introduction to the main concepts of light scattering in solids focused on the Raman scattering process. Raman scattering is an inelastic light scattering process, which is a very sensitive, versatile and powerful experimental probe used in a variety of fields such as physics, chemistry and nanotechnology. The term "scattering" can be classified into two processes after Ref. [64]:

1. Potentials that are constant in time, such as impurities in a crystal, which do not change the energy of the particle being scattered

2. Potentials that vary harmonically in time as $\cos(\omega_q t)$, such as phonons and photons, which change the energy of the particle by $\pm\,\hbar\omega_q$

Firstly the general concept of light-matter interaction is dealt with using the electron-photon interaction Hamiltonian in the semi-classical approach, before progressing to inelastic light scattering. Then the electron-phonon coupling is introduced within the Born Oppenheimer or adiabatic approximation. In addition to the electron-photon coupling, also the electron-phonon coupling is an important quantity for Raman scattering. The theory of Raman scattering is then briefly introduced together with the basic concepts and salient points of resonant Raman scattering and double-resonant Raman scattering. Here, the theory of Raman scattering is referred to the electron-photon and electron-phonon interaction. Two methods are of central importance to this thesis, resonant Raman scattering and double-resonant Raman scattering. The optical transition of carbon nanotubes as a function of temperature will be discussed in Chapter 4. Optical transitions are monitored via resonant Raman scattering. In Chapter 5 the phonon dispersion of bilayer graphene via double-resonant Raman scattering is examined. This introduction therefore gives an insight to the possibilities of Raman scattering and how information can be derived from it.

3.1 Electron-photon coupling

To obtain an understanding of inelastic light scattering the electron-photon interaction is reviewed within the microscopic theory of the dielectric function. In principle it is a semi-classical approach, where the electromagnetic field is treated as classical and the electrons are described within quantum mechanical wave functions. This derivation is discussed in many textbooks, such as Ref. [64–66]. According Ref. [65] the quantum mechanical Hamiltonian including the description of a charge -e in the presence of an external electromagnetic field is:

$$H = \frac{1}{2m}\left[\mathbf{p} + (e\,\mathbf{A}/c)\right]^2 + V(\mathbf{r}), \tag{3.1}$$

where the electron momentum operator $\mathbf{p}$ was replaced by $\mathbf{p} + (e\,\mathbf{A}/c)$ to take into account the motion of a charge in an external electromagnetic field. $\mathbf{A}$ is the vector potential and $V(\mathbf{r})$ is the potential of the crystal. Where the electron momentum $\mathbf{p}$ can be expanded and the square can then be written as follows:

$$\frac{1}{2m}\left[\mathbf{p} + (e\,\mathbf{A}/c)\right]^2 \rightarrow \frac{p^2}{2m} + \frac{e}{mc}\cdot[\mathbf{p}\cdot\mathbf{A} + \mathbf{A}\cdot\mathbf{p}] + \frac{1}{2m}\left(\frac{e}{c}\right)^2\mathbf{A}^2 \tag{3.2}$$

Since the coupling of light occurs via the gauge invariance of the Maxwell equations, $\mathbf{p}$ can be expressed with the definition of an operator. Substituting for the momentum as outlined in 3.2 yields:

$$\mathbf{p}^2 \rightarrow \frac{(\nabla - \frac{e}{c}\mathbf{A})^2}{2m} = \frac{\nabla^2}{2m} - \frac{e}{c}\frac{\nabla\cdot\mathbf{A}}{2m} - \frac{e}{c}\frac{\mathbf{A}\cdot\nabla}{2m} + \frac{1}{2m}\left(\frac{e}{c}\right)^2\mathbf{A}^2 \tag{3.3}$$

The first term is the Hamiltonian of the unperturbed system, the second and third term are identical in case of the Coulomb gauge ($\nabla\cdot\mathbf{A} = 0$) and linear in the vector potential $\mathbf{A}$. Gauge conditions are used as an additional condition since otherwise $\mathbf{A}$ and the wave function Ψ are not uniquely determined. The Coulomb gauge induces that the Coulomb field acts instantaneously. The last term exhibits a quadratic term in $\mathbf{A}^2$ and yields non-resonant inelastic light scattering. In most experimental situations however the use of resonance effects are available. These can be probed via second order perturbation using $H^{\nabla\cdot\mathbf{A}}$. Equation 3.3 can be simply written as follows.

$$H \rightarrow H_0 + H^{\nabla\cdot\mathbf{A}} + H^{\mathbf{A}^2} = H_0 + H_{int} \tag{3.4}$$

H_0 is the Hamiltonian of the unperturbed system and the remaining terms can be summarized in H_{int}, which is the interaction Hamiltonian.

By using the Coulomb gauge, and neglecting the quadratic term for the calculation of linear optical properties, the interaction Hamiltonian reduces to a term referred to as electron-radiation interaction Hamiltonian H_{er}:

$$H_{er} = \frac{e}{mc}\,\mathbf{A}\cdot\mathbf{p}. \tag{3.5}$$

This term describes the interaction between the electromagnetic radiation and Bloch electrons. However,

the expression of Eq. 3.5 depends on the chosen gauge. Another more commonly used expression of the electron-radiation Hamiltonian is in the following form:

$$H_{er} = (-e)\,\mathbf{r} \cdot \mathbf{p}. \tag{3.6}$$

These two expressions are equivalent when treating in the electric dipole approximation, which is the limit that the wave vector **q** is small.
The propagation of light is determined by the dielectric function. The dielectric function depends on both frequency and wave vector independently. The dielectric function for a classical, charged and harmonic oscillator can be according Ref. [65] expressed as follows:

$$\epsilon_r(\omega) = 1 + \frac{4\pi e^2}{4\pi\epsilon_0 m}\left(\sum_i \frac{N_i}{\omega_i^2 - \omega^2}\right) \tag{3.7}$$

The Fermi-Golden rule, which is commonly used for the calculation of transition rates, is given as:

$$T = \frac{2\pi}{\hbar}\,\langle f \,|\, H_{er} \,|\, i\rangle^2 \;\rho, \tag{3.8}$$

where $\langle f \,|\, H_{er} \,|\, i\rangle^2$ is the matrix element of a perturbation between the final state (f) and initial state (i). H_{er} is the electron-radiation Hamiltonian from Eq. 3.5 and 3.6 and ρ represents the joint density of states, which is the number of electronic states in the valence and conduction band at a certain energy. Now the Femi-Golden rule is applied to the Hamiltonian and an expression is derived for the dielectric function, which can then be compared to the dielectric function of Eq. 3.7. From this comparison a dimensionless quantity known as oscillator strength is obtained.
The matrix element of Eq. 3.5 can be written as follows:

$$\langle f \,|\, H_{er} \,|\, i\rangle^2 = \left(\frac{e}{mc}\right)^2 \langle f \,|\, \mathbf{A}\cdot\mathbf{p} \,|\, i\rangle^2 = \left(\frac{e}{mc}\right)^2 |A|^2 |P_{if}|^2. \tag{3.9}$$

$|P_{if}|^2$ is a constant and reflects that the momentum dependence on **k** is neglected due to a weak dependency [65]. The transition probability T is now obtained and the vector potential **A** is written in terms of the amplitude of the incident electric field $\mathbf{E}(\mathbf{q},\omega)$:

$$A = -E/2q(exp[i(\mathbf{q}\cdot\mathbf{r} - \omega t)]) + \text{complex conjugate} \tag{3.10}$$

and can then be written as:

$$T = \frac{2\pi}{\hbar}\left(\frac{e}{mc}\right)^2 \left(\frac{E(\omega)}{2}\right)^2 \sum_k |P_{if}|^2 \delta(E_i(\mathbf{k}) - E_f(\mathbf{k}) - \hbar\omega). \tag{3.11}$$

The δ term describes the emission process of the electron, which is excited from the initial state to its final state. This corresponds to an excitation of an electron into the conduction band. Then by using the power lost by the field in the absorption process and relating the energy density to the field amplitude, one

obtains the expression for the dielectric function. A more detailed derivation can be found in Ref. [65]. The dielectric function yields:

$$\epsilon_r(\omega) = 1 + \frac{4\pi e^2}{4\pi\epsilon_0 m}\left[\sum_k \left(\frac{2}{m\hbar\omega_{if}}\right)\frac{P_{if}^2}{\omega_{if}^2 - \omega^2}\right] \tag{3.12}$$

By comparing Eq. 3.7 with Eq. 3.12 a one dimensionless quantity, which is known as the oscillator strength, can be derived. When treating a number of oscillators in classical electrodynamics, the oscillator strength f_i is used as a statistical weight for the indication of relative numbers of oscillators, which are bound at each resonant frequency ν_i. In quantum mechanics, the oscillator strength has the meaning of relative strength of the electronic transition and is used for comparing transition strengths between different quantum mechanical systems. The oscillator strength reads as:

$$f_{if} = \frac{2|P_{if}|^2}{m\hbar\omega_{if}} \tag{3.13}$$

The oscillator strength can be derived from taking the square value of the optical matrix element.

3.2 Electron-phonon coupling

The electron-phonon coupling is a quantity that is important for Raman scattering and responsible for the electrical resistance of semiconductors at room temperature [67]. Further it determines phenomena such as charge transport, electron-hole lifetimes and superconductivity [9, 68]. The coupling strength is accessible via Raman scattering. In general, electrons screen phonons. In metals and semi-metals such as graphene, graphite and metallic carbon nanotubes the screening changes at certain points in the Brillouin zone. This occurs if the displacement of phonons disturb electrons at the Fermi surface. In consequence the electrons rearrange themselves and change their screening. A strong electron-phonon coupling softens the phonon frequencies in the vicinity of the K point and the Γ point. This abrupt change in the phonon dispersion is known as Kohn-anomaly [69]. The construction of the Fermi surface determines the occurrence of the Kohn-anomaly in a metal. A phonon wave vector $\mathbf{q}$ connects two electronic states k_1 and k_2 = k_1 + $\mathbf{q}$ so that both states are on the Fermi surface. Since graphene has two non-equivalent K points (K and K', with K' = $2K$), the Kohn-anomaly occurs for phonons where the following conditions are satisfied [56, 70–72]:

$$\mathbf{q} = K - K = 0 = \Gamma \text{ and } \mathbf{q} = K' - K = 2K - K = K. \tag{3.14}$$

It follows that one has two Kohn-anomalies at the Γ and at the K point and these can be probed via Raman scattering by measuring the G and D mode, respectively.

To obtain an understanding of the electron-phonon coupling, the Hamiltonian in the Born- Oppenheimer or adiabatic approximation is considered, since a full treatment of the many-body Hamiltonian is unsolvable [65]. The approximation is based upon the fact that electrons move much faster than the ions as a consequence of the mass difference. In this approximation, three Hamiltonian terms have to be considered. First two terms describing the motion of the ions and electrons, which are written as $H_{ion}(\mathbf{R})$ and $H_e(\mathbf{r},\mathbf{R})$. These two terms describe each motion separately. The last term treats the coupling among the electron and the ions and is written as $H_{e-ph}(\mathbf{r}, \delta\mathbf{R})$. The full Hamiltonian then reads as [65, 73]:

$$H = H_{ion}(\mathbf{R}) + H_e(\mathbf{r},\mathbf{R}) + H_{e-ph}(\mathbf{r}, \delta\mathbf{R}). \tag{3.15}$$

The electron-phonon Hamiltonian corresponds to the interaction of individual atoms at $\mathbf{r}$ and the electrons at $\mathbf{k}$ and can be written as:

$$\begin{aligned} H_{e-ph}(\mathbf{r}, \delta\mathbf{R}) &= \sum_{k,k',x} \langle \mathbf{k} | \, V \, | \mathbf{k'} \rangle \, c_k^\dagger c_k \\ &= \sum_{k,k',x} e^{i(\mathbf{k'}-\mathbf{k})\cdot(x+\delta R)} V_{k,k'} c_k^\dagger c_k \\ &= iN^{-1/2} \sum_{k,k'} ((\mathbf{k'} - \mathbf{k})\delta R \, V_{k,k'} c_k^\dagger c_k \end{aligned} \tag{3.16}$$

The term in brackets scatters an electron from state **k'** to **k** in the presence of a single ion potential V. The displacement of the ion is represented by δR and x denotes the equilibrium position. In the second line in 3.16 the potential was rewritten into the Fourier transform. Usually small displacements are described so that (**k** - **k'**) · δR is $\ll 1$. The last line in 3.16 is obtained by expanding:

$$\begin{aligned} e^{i(\mathbf{k}\,-\,\mathbf{k'})\delta R} &\approx 1 + i(\mathbf{k}\,-\,\mathbf{k'})\delta R \\ = 1 + iN^{-1/2}\mathbf{q}\cdot\sum(\mathbf{k}\,-\,\mathbf{k'})e^{i\mathbf{q}\cdot\mathbf{x}}\delta R. \end{aligned} \tag{3.17}$$

Only the second term has a dependence on the displacement of the ions and provides a contribution to the electron-phonon coupling. Within the harmonic approximation the displacement δR can written as:

$$\delta R = \sqrt{\frac{\hbar}{2M\omega_q}}(a^\dagger_{-q} + a_q)\hat{e}, \tag{3.18}$$

where the phonon frequency is denoted as ω_q, the mass of the ions is M and $\hat{e}$ describes the direction of the displacement.
The full Hamiltonian can also be written in terms of a second quantization:

$$H = \sum_k \epsilon_k c^\dagger_k c_k + \sum_q \hbar\omega_q a^\dagger_q a_q + \sum_{k,k'} M_{k,k'}(a^\dagger_{-q} + a_q)c^\dagger_k c_k\ , \tag{3.19}$$

with $c^\dagger_k$ and c_k for the creation and annihilation of electrons with energy ϵ_k. The phonon creation and annihilation operators with energy $\hbar\omega_q$ are denoted as $a^\dagger_q$ and a_q, respectively. The last red term corresponds to the interaction term consisting of two contributions, namely the emission and absorption of a phonon.
The matrix element $M_{k,k'}$ is defined by:

$$M_q = i\left(\frac{N\hbar}{2M\omega_{q,\hat{e}}}\right)^{\frac{1}{2}}\textbf{(k-k')}\ V_{\textbf{k-k'}}. \tag{3.20}$$

M denotes the mass of the unit cell, N is the number of units cells in the system and ω_q is the phonon frequency.

3.3 Theory of Raman scattering

Raman Scattering was discovered in 1928 by Sir C.V. Raman [74] who two years later, in 1930, received the Nobel Prize in Physics for this discovery. Raman scattering can be simplified when reducing it to a three-step process, see Fig. 3.1. The light enters the sample in the first step. Then the inelastic light scattering event occurs. In the third and last step, the inelastically scattered photons of step two emerge out of the sample. This is shown in Fig. 3.1 (a). A more quantitative picture of the interaction is shown in Fig. 3.1 (b) and (c). Figure 3.1 (c) is known as a Feynman diagram for the Raman scattering process. In both illustrations, Fig. (b) and (c), the process is initiated by the incoming laser light with frequency ω_i, momentum k_i and excitation energy E_i which is represented by the blue arrow. Then the interaction of photons and electrons from its initial state $|i\rangle$ to its intermediate state $|a\rangle$ takes place. This interaction is described by interaction the Hamiltonian H_{er}, which was derived in the previous chapter. In the picture of the Feynman diagram this excitation creates virtual electron-hole pairs. These virtual electrons or holes are then scattered creating (Stokes Raman scattering) or annihilating (Anti-Stokes Raman scattering) elementary excitations, such as magnons, plasmons or phonons. Then the virtual electron and hole recombine emitting a photon with frequency ω_s, momentum k_s and energy $E_s = E_i \pm \hbar\omega_{ph}$ depending on whether having created or annihilated a phonon. The red arrow represents the scattered light. In the following exclusively Stokes scattering will be discussed.

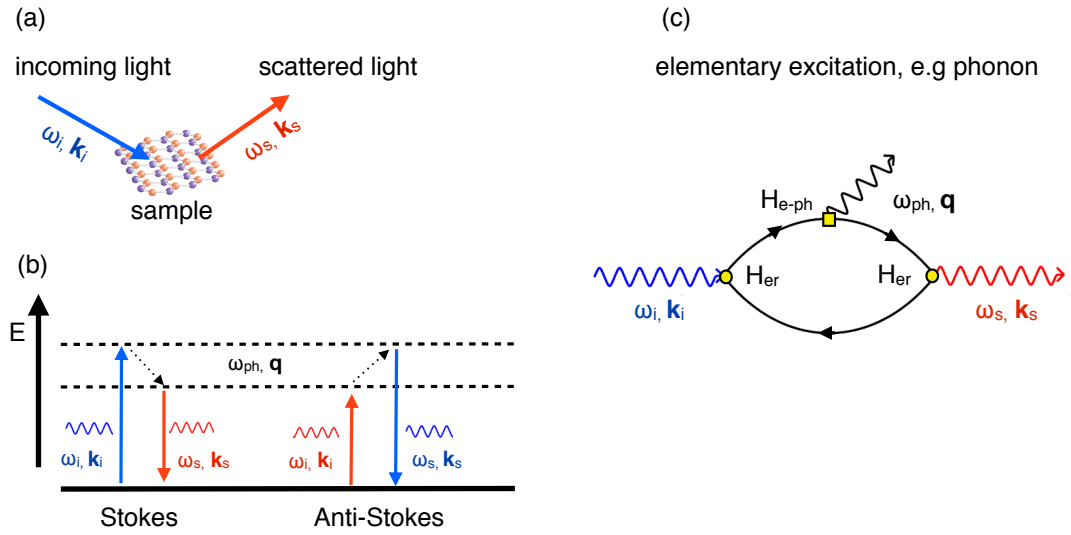

Figure 3.1: (a) shows a simplified sketch of the Raman process. (b) shows a scheme of Stokes and Anti-Stokes Raman scattering. (c) illustrates the Feynman diagram of the Raman process only representing the electron contribution. Here the process is clearly demonstrated as three-particle interaction with three vertices. The vertices of the interaction Hamiltonian H_{er} and H_{e-ph} are illustrated by two yellow filled circles and one yellow filled square,respectively.

It should be noted that Fig. 3.1 (c) illustrates the Feynman diagram of the Raman process representing the

electron contribution only. The process is demonstrated as three-particle interaction with three vertices. The vertices are illustrated by two yellow filled circles and one yellow filled square: , i.e. the coupling points where the interaction takes place. The incident photon leads to the transition to an intermediate electron-hole pair via the interaction Hamiltonian H_{er}. Then the electronic transition to another electron-hole pair takes place with the emission of a phonon (Stokes Raman scattering) with interaction Hamiltonian H_{e-ph}. Finally the scattered photon is created via a transition back to the ground state with the interaction Hamiltonian H_{er}.

In order to obtain an expression for the Raman scattering process shown in Fig. 3.1 (c) the three vertices are considered. The first contribution stems from the interaction Hamiltonian (H_{er}) with a first order perturbation term in the following form [65]:

$$\sum_{a} \frac{< a|H_{er}(\omega_i)|i >}{(\hbar\omega_i - (E_a - E_i)}. \tag{3.21}$$

Multiplying this expression with the second vertex, which is related to the interaction of electron and phonons, the following equation is obtained:

$$\sum_{a,b} \frac{< b|H_{e-ph}(\omega_0)|n > \ < a|H_{er}(\omega_i)|i >}{(\hbar\omega_i - (E_a - E_i))\ (\hbar\omega_i - (E_a - E_i - \hbar\omega_{ph} - (E_b - E_a))}. \tag{3.22}$$

This equation can be simplified in the denominator and written as:

$$\sum_{a,b} \frac{< b|H_{e-ph}(\omega_0)|n > \ < a|H_{er}(\omega_i)|i >}{(\hbar\omega_i - (E_a - E_i))\ (\hbar\omega_i - \hbar\omega_{ph} - (E_b - E_i))}. \tag{3.23}$$

The last term stems from the interaction Hamiltonian H_{er}. However due to the fact that the electrons are unchanged after the scattering process, the final electronic state $|f >$ is identical to the initial state $|i >$. The denominator represents the energy conservation of the process and is converted to a delta function otherwise the term would vanish.

Then the Raman scattering probability can be written as given by the Fermi Golden Rule [65]:

$$P_{ph}(\omega_s) = \left(\frac{2\pi}{\hbar}\right) \left| \sum_{a,b} \frac{< i|H_{er}(\omega_s)|b > \ < b|H_{e-ph}|n > \ < a|H_{er}(\omega_i)|i >}{(\hbar\omega_i - (E_a - E_i))\ (\hbar\omega_i - \hbar\omega_{ph} - (E_b - E_i))} \right|^2 \times \delta(\hbar_{\omega_i} - \hbar_{\omega_{ph}} - \hbar_{\omega_s}). \tag{3.24}$$

However Eq. 3.24 does not represent the complete scattering probability, since five more scattering processes need to be taken into account, and which contribute to one-phonon Stokes Raman scattering. These expressions are permutations of the above given equation and can be found in Ref. [65].

Two-phonon Raman scattering has to fulfill a necessary condition, that the momenta of the two phonons cancel for opposite phonon vectors. The condition $|\ \mathbf{q}_{\max}\ | = |\ \mathbf{q}_1 - \mathbf{q}_2| \approx 4n\pi\ /\ \lambda_i$, where n is the refractive index and λ is the wavelength of the incoming light, is fulfilled for light in the visible region.

3.3.1 Resonant Raman scattering

Resonant Raman scattering yields further information about the inelastic scattering process and reveals properties related to resonant behavior. Figure 3.2 shows the behavior of an electron excited in the Stokes Raman scattering process at different excitation energies.

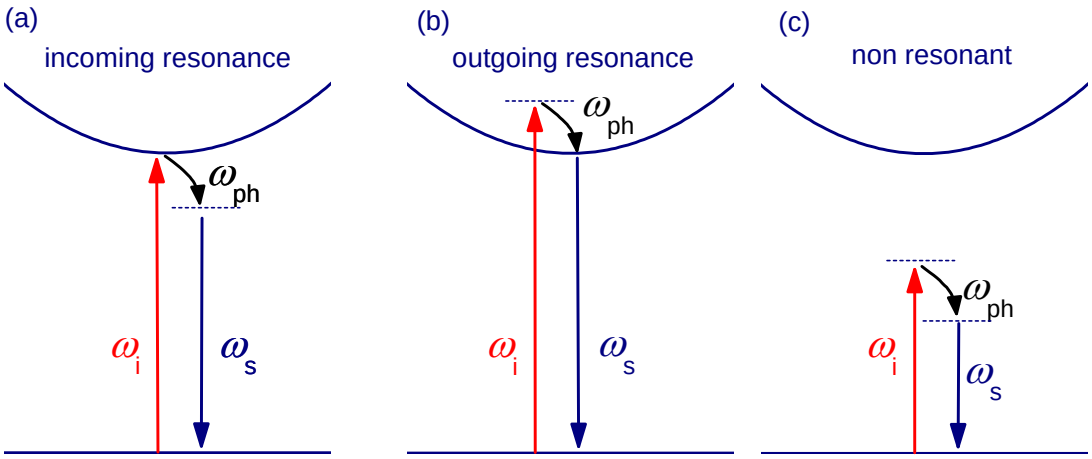

Figure 3.2: (a) incoming resonant Raman scattering process (when the energy of the incident light matches a real transition), (b) outgoing resonant Raman scattering process (when the scattered light matches a real transition) and c) non resonant Raman scattering process (neither incident nor scattered light matches a real transition). The red arrow (ω_i) indicates the incident light and the blue arrow (ω_s) indicates the scattered light. The dashed line indicate a virtual electronic transition of either the phonon (in the case of incoming resonance) or electron (in the case of outgoing resonance). There are no real transitions in the case of non resonant Raman scattering.

The resonance condition can be deduced from Eq. 3.24 and found in the denominator of this expression. The probability of Raman scattering is enhanced under the condition that the energy difference between the incident photon $\hbar\omega_i$ and the electron-hole energy (E_{ai} - E_i) or between the scattered photon ($\hbar\omega_s$ = $\hbar\omega_i$ - $\hbar\omega_{ph}$) and the electron-hole energy (E_{bi} - E_i) is zero [57]. The first case is also referred to as incoming while the second is referred to as outgoing resonance. The necessary condition for resonant enhancement is therefore a vanishing denominator in Eq. 3.24. Under this condition the sum of a states can be replaced by one term directly connecting the state $|a>$ to a photon energy $\hbar\omega_a$. To avoid non-physical situations a broadening parameter γ as a consequence of the finite lifetime of the excitation and therefore the natural linewidth has to be added. In resonance, the Raman probability of Eq. 3.24 can be written as:

$$P_{Raman} \propto \left| \sum_{a,b} \frac{< f|H_{er}|b >< b|H_{e-ph}|a >< a|H_{er}|i >}{(E_i - E_{ai} - i\gamma)(E_i - \hbar\omega_{ph} - E_{bi} - i\gamma)} \right|^2 . \tag{3.25}$$

Resonant Raman scattering allows the electronic structure of materials to be probed and thereby de-

rive information concerning various optical transitions. This is especially true in carbon nanotubes, as resonant Raman scattering has become a key method to determine the optical transition for particular nanotubes.

3.3.2 Double-resonant Raman scattering

Resonant Raman scattering refers to absorption or emission of photons between two real electronic states, introduced as incoming or outgoing resonances in the previous subsection. Double resonant scattering, on the other hand, means that both the excited electron and excited phonon (for Stokes scattering) make a real transition. Double-resonances are known from semiconductors between two electronic states, however they only occur under external perturbations such as strain, pressure or by applying external fields [75,76]. The interpretation of the dispersive behavior of the D mode and its overtone the $2D$ mode in carbon systems has been investigated for over 40 years. [77–90]. In 2000 the origin of this mode was correlated to the double-resonant process by Thomsen *et al.* [81]. In carbon-based materials the double-resonant process occurs under ambient conditions and is indispensable for the interpretation of Raman spectra. Further it proved to be a sensitive to tool for probing both the electronic bandstructure and phonon dispersion.

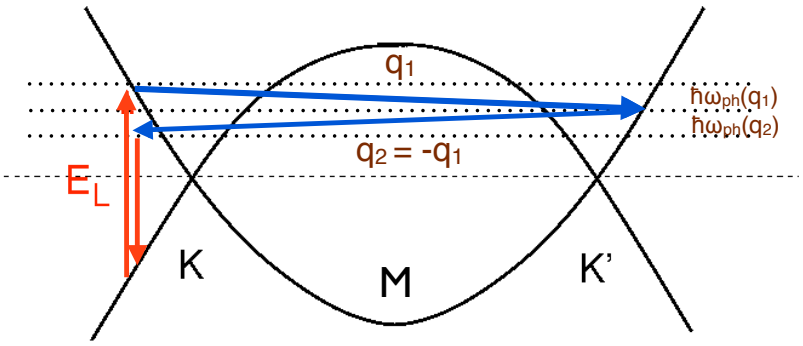

Figure 3.3: Illustration of the *outer* double-resonant Raman scattering process (electron scattering only) in the electronic bandstructure of single-layer graphene. As a consequence of the electronic bandstructure, any incident excitation energy $E_i = E_L$ finds an incoming transition.

The double resonance Raman process is depicted in Fig. 3.3, and has been shown to explain the dispersive behavior of several Raman modes in the spectrum of graphite [81]. Due to the unique electronic bandstructure, any laser energy finds an incoming real transition. The double-resonant process is initiated by the excitation of an electron-hole pair, then phonon assisted scattering of the electron (or hole) with a phonon wave vector $q_1 \neq 0$. For the disorder-induced D-mode, the electron (or hole) is scattered back by a defect, for the second order process the electron (or hole) is scattered back by another phonon with

$q_2 = -q_1$. Finally electron and hole recombine emitting a photon with an energy $E = E_l - 2\hbar\omega\,(q_1)$, where E_l denotes the excitation laser energy (corresponds to the incident excitation energy E_i) and $\hbar\omega\,(q_1)$ is the phonon energy. In graphene and graphite, the phonons contributing to this process stem from the fully symmetric TO-derived (transverse optical) branch near the K-point [37, 91].

Outer vs. Inner double-resonant Raman scattering

There is an on-going discussion concerning the relevant scattering contributions, namely the role of the so-called *inner* and *outer* processes, where *inner* (*outer*) refers to scattering by phonons with wave vector between Γ - K (K- M) [35, 86–88, 90, 92]. In other words, *outer* processes correspond to an electronic transition between Γ - K and *inner* processes correspond to an electronic transition between K- M. The *inner* double-resonant Raman scattering process is shown in Fig. 3.4. The scattering process is equivalent to the *outer* double-resonant process, however the electronic excitation takes place between the (K- M) direction in contrast to the Γ - K in *outer* processes. This discussion was first highlighted in a theoretical work of Mohr *et al.* [87] by pointing out that in strained monolayer graphene only the combination of both *inner* and *outer* processes can explain the strain-induced splitting of the Raman modes, in agreement with strain experiments [35, 36]. In the literature *inner* processes are very often neglected [93], based on a density of states argument of Ref. 94. However, if a full integration along the high symmetry directions of the graphene Brillouin zone is performed, both *inner* and *outer* contributions appear in the calculated Raman spectra [85].

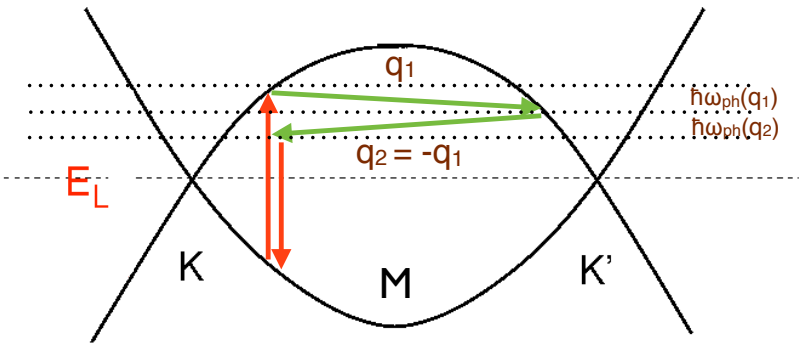

Figure 3.4: Illustration of the *inner* double-resonant Raman scattering process (electron scattering only) in the electronic bandstructure of single-layer graphene in addition to Fig. 3.3.

4 Excitons in single-walled carbon nanotubes

This chapter deals with optical transitions in carbon nanotubes and briefly addresses the general properties of excitons. The optical transitions in the single-particle picture are first introduced as they provide an intuitive description of the relationship of particular nanotubes, their electronic structure and consequently their density of states. Here resonant Raman scattering is a key technique in determining the optical transition for particular nanotubes, even in samples with a variety of chiralities. It was found that optical transitions arise from strongly bound electron-hole pairs (excitons), bound together by their mutual Coulomb interaction. They are a key factor in the understanding of optical transitions. Excitons are well known in bulk semiconductors with binding energies of the order of a few meV [65]. In one-dimensional systems such as carbon nanotubes the interaction is enhanced due to spatial confinement of the excited electron and the hole and decreased screening of the environment. Especially their sensitivity to external perturbations, such as the surrounding environment or external fields, permits to change and tune the optical properties [15].

The determination of the exciton binding energy is challenging, since in the optical spectra the absorption is fully restored in the excitonic transition and can hardly be distinguished from the continuum absorption [95]. In bulk materials, there is still a contribution from its continuum. However, this is strongly suppressed in semiconducting nanotubes due to very high binding energies up to $1\,\mathrm{eV}$. Theory predicts a variety of excitonic states with different symmetry as shown in Fig. 4.1. One-photon spectroscopy couples to optically active excitonic states with odd (u) symmetry with respect to rotations about the U axis [96]. The lowest lying dark state is dipole forbidden by symmetry [97]. The technique of two-photon photoluminescence spectroscopy was applied in order to obtain the binding energies of semiconducting carbon nanotubes by Wang *et al.* and Maultzsch *et al.* [98, 99]. Two-photon absorption occurs at the $2g$ excitonic state. Therefore by an analysis of one-photon and two-photon absorption, the exciton binding energy was determined. However, this technique is restricted to semiconducting nanotubes as a consequence of non-radiative decay in metallic nanotubes.

The screening of electrons is rather effective in metals and therefore, the formation of excitons is expected to be prevented. It has been a longstanding question to what extent optical transitions are dominated by excitons in metallic SWCNTs, though theoretical calculations predicted binding energies of the order of 50 - 100 meV. Wang *et al.* [100] discovered the first experimental evidence of excitons in metallic systems. Absorption spectroscopy was performed on individual metallic tubes and the absorption spectra were interpreted after a careful lineshape analysis. However, this technique is difficult to apply due to the necessity of measuring individual tubes. In contrast, resonant Raman spectroscopy can be applied to ensembles with many different chiral indices and additional information on specific chiral indices

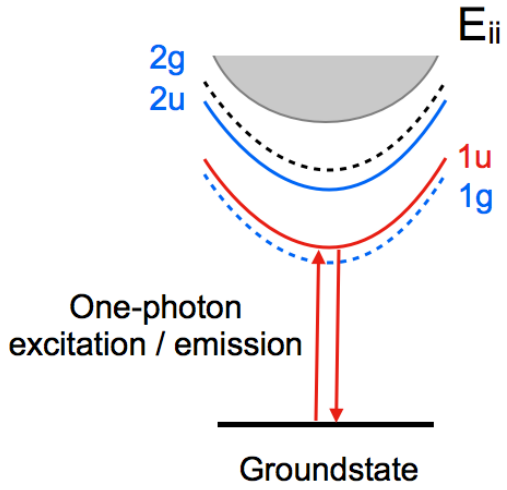

Figure 4.1

Excitonic states of a particular transition denoted as E_{ii}. The $1u$ and $1g$ correspond to the $1s$ excitonic state in the hydrogen model. The $2u$ and $2g$ transitions correspond to the $2p$ states. Only the odd states (u) are addressed by one-photon absorption, while with two photon absorption the even states (g) state are addressed. Adapted from Ref. [99]

(n,m) can be obtained. In this chapter an approach for the determination of the exciton binding energy is shown. Here, the optical transition is monitored by applying temperature. First, the influence on how the optical transition is changed by applying temperature is shown for one metallic and one semiconducting nanotube. The results are further compared to calculations and other experiments.
A sudden upshift in the transition energy is observed for the metallic nanotubes, which is attributed to the dissociation of excitons. The temperature dependence of the excitonic oscillator strength is further discussed and related to the measurements. A comparison to calculated absorption spectra including and excluding excitonic effects further supports the interpretation and explains the onset in the Raman intensity of the metallic nanotube, while the behavior of the semiconducting nanotube is explained with the temperature dependence of the oscillator strength. The last section deals with multiphonon scattering of the same sample. Higher order Raman modes are observed up to $6000\,\mathrm{cm}^{-1}$. These results are compared to measurements on individual carbon nanotubes and graphite. The strong overtones compared to graphite provide further evidence for transitions mediated by excitons.

4.1 Optical transitions in carbon nanotubes

Raman spectroscopy proved to be an important tool for the characterization of specific (n, m) nanotubes [101]. In addition to the modes present in graphene, carbon nanotubes exhibit a characteristic low-frequency mode, which is called the radial breathing mode (RBM). This mode arises from a radial, in phase vibration of all carbon atoms in the unit cell. The frequency is further dependent of the diameter and is increasing with decreasing diameter [102–106]:

$$\omega_{\mathrm{RBM}} = \frac{c_1}{d} + c_2. \tag{4.1}$$

A variety of values for c_1 and c_2 have been derived by several groups [42, 107–109].
For example Telg *et al.* [42] found $\omega_{\mathrm{RBM}} = 214.4\ \mathrm{cm}^{-1}\ \mathrm{nm}\ /\ d + 18.7\ \mathrm{cm}^{-1}$.
The resonance behavior of the RBM is used to obtain the optical transition energy of particular carbon nanotubes. Due to the diameter dependence of the frequency it is possible to measure optical transitions in ensembles of carbon nanotube samples.

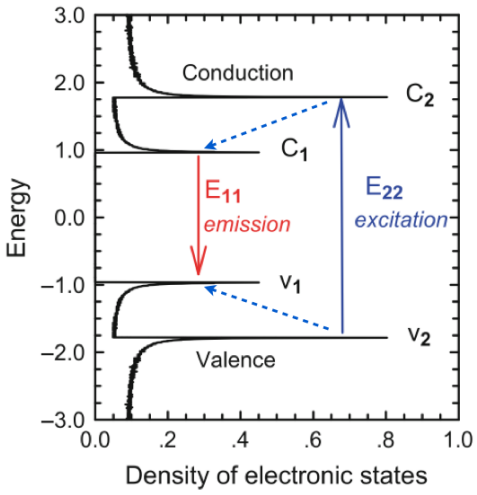

Schematic illustration of the electronic density of states. Excitation and emission of semiconducting single-walled carbon nanotubes in the picture of band-to-band transitions. Solid arrows depict the optical excitation and emission from and into the ground state, the dashed blue arrows indicate the non-radiative relaxation of the electron and hole, respectively. Taken from Ref. [110]

Figure 4.2

Optical transitions in carbon nanotubes were first believed to originate from band-to-band transitions. Band-to-band transitions mean the inclusion of self-energy effects (electron-electron interaction or renormalized free-particle) but the negligence of the interaction between electron and hole. This so-called single-particle picture gives an intuitive picture of optical transitions. Density of states (DOS) and optical selection rules can be derived from this approximation and later transferred to excitonic transitions. The consideration of the DOS provides an essential quantity in the experimental study of electronic properties. For bulk materials the DOS exhibits a square root dependence on the energy above the bandgap. In one-dimensional systems, however, the DOS is inverse proportional to the square root of the energy.

Therefore the electronic dispersion in carbon nanotubes can be simplified by considering the one-dimensional DOS with van Hove singularities for valence and conduction bands. What is referred to as van Hove singularity (vHs) is the divergence at the extreme of the conduction and the valence band as depicted in Fig. 4.2. Further characteristics are the decaying tails between the maxima. At the extreme, very strong absorption or scattering of phonons matching the particular transition is expected. Due to the quick fall-off, the electronic structure exhibits very strong resonance behavior, which permits the defining of particular nanotubes even in an ensemble. It should be noted that the vHs are based upon a treatment of free-carriers neglecting Coulomb effects. While the semiconducting nanotube exhibit zero DOS at the Fermi level, metallic nanotubes exhibit a non-zero DOS at the Fermi level due to the crossing of the electronic bands at the K point.
The optical transition is defined as E_{ii} with i denoting the order of valence and conduction bands. In the single-particle picture, the optical transition is expected to have a simple diameter dependence, which is $1/d$. Plotting the measured transition energy over the diameter or the RBM frequency one obtains the Kataura plot, which is then compared to theoretical results based on zone-folding or non-orthogonal tight-binding. Bachilo *et al.* [63] measured photoluminescence and absorption spectra of isolated carbon nanotubes. They found the optical transition to deviate from simple theoretical diameter dependence calculations and attributed this result to trigonal warping and excitonic effects. From tight-binding calculations one would expect that the ratio of the second and the first optical transition E_{22} / E_{11} should approach 2 in the limit of large diameters.

4.1.1 Concept of excitons and many-body corrections

In this section, the concept of excitons is introduced first for a typical three-dimensional semiconductor. The absorption of photons produces bound electron-hole pairs that have, in most cases, weak binding energies as a consequence of dielectric screening. In contrast to these so-called Wannier-Mott excitons, Frenkel excitons exhibit strong electron-hole interactions. Here, only weak binding energies are discussed for providing a general understanding of the concept of excitons.
The valence and conduction bands are assumed to exhibit a parabolic dispersion with isotropic masses m_e and m_h. The minimum and maximum of the two bands is at **k** = 0. The energy for the valence and conduction band can be written as follows:

$$\begin{aligned} E_v(\mathbf{k}) &= E_c(0) - E_{gap} - \frac{\hbar^2 k^2}{2m_h} \\ E_c(\mathbf{k}) &= E_c(0) + \frac{\hbar^2 k^2}{2m_e}, \end{aligned} \tag{4.2}$$

where E_g is the bandgap energy. Here, the motion of the two particles, i.e. the electron and hole is determined by the effective masses of the particular band.
The excitonic picture combines both the electron and hole wave vector to an exciton wave vector defined as **K** = k_e + k_h. The kinetic energy can then be expressed in terms of the exciton wave vector and the translational mass $M = m_e + m_h$ [65]:

$$E_{kin} = \frac{\hbar^2 K^2}{2M}, \tag{4.3}$$

describing the motion of a two-particle state. A very good approximation is the approach of treating the electron and hole similar to a hydrogen-like problem. The hydrogen atom exhibits a Coulomb potential term and a series of states below the bandgap. The dispersion relation of the excitons reads as follows:

$$E_{XB}(n, \mathbf{K}) = E_g + \frac{\hbar^2 \mathbf{K}^2}{2M} - Ry^* \frac{1}{n^2}, \tag{4.4}$$

where $n = 1, 2, 3...$ is known as the principal quantum number. Ry^* is the exciton Rydberg energy and defined as follows:

$$Ry^* = 13.6eV \frac{\mu}{m_0} \frac{1}{\epsilon^2}, \tag{4.5}$$

where m_0 is the rest mass of the electron and the reduced exciton mass μ is introduced and written as:

$$\mu = \frac{m_e m_h}{m_e + m_e}. \tag{4.6}$$

The dielectric constant ϵ enters with an inverse square dependence and actually has an impact on the binding energy [38, 39, 111].

In one-dimensional systems there are a number of theoretical papers introducing the importance of excitons in one-dimensional carbon nanotubes. T. Ando published the first in 1997 [112]. In this paper the exciton levels were calculated within the conventional screened Hartree-Fock approximation and a $\mathbf{k} \cdot \mathbf{p}$ scheme. Some years later Pedersen calculated the exciton binding energy depending on the nanotube diameter within a variational approach [113]. Kane and Mele followed a similar approach than that of Ando [112]. However, they focussed on the diameter dependence of the energy gaps [114]. An *ab-initio* symmetry based approached followed for a small diameter nanotube, namely the $(4, 2)$ [115]. Perebeinos *et al.* [111] demonstrated the importance of the dielectric environment. An *ab-initio* many electron approach including the method of Green's functions confirmed the existence of excitons for a small diameter $(8, 0)$ nanotube [116]. Further, Spataru *et al.* calculated the excitonic binding energy of a small $(3, 3)$ metallic nanotube to be of the order of ≈ 100 meV. As previously mentioned, the exciton binding energy of semiconducting nanotubes E_{XB} was experimentally determined to be of the order of 300-500 meV [98, 99]. In Chapter 4.2 excitons in metallic carbon nanotubes are considered. The exceptionally high binding energies in carbon nanotubes are a consequence of both the dimensionality and the screening. For example, bulk CdSe exhibits a dielectric constant of $\epsilon \approx 8.2$ resulting in an exciton binding energy of E_{XB}=15 meV compared to a bandgap of E_{gap} = 1.84 eV. Carbon nanotubes on the other hand have an intrinsic dielectric constant which is approximately three times less than CdSe also as a consequence of the low dimensionality [117]. It has been shown that the overall exciton binding energy scales with $1/\epsilon^{\alpha}$, whereas α has been found to be 1.2 in an experimental work of Walsh *et al.* in Ref. [38, 39] and 1.4 in a theoretical work of Perebeinos *et al.* in Ref. [111].

4.2 Observation of excitons in metallic carbon nanotubes

A direct measurement of the exciton binding energy in metallic carbon nanotubes is now presented and temperature-dependent measurements of the particular transition are performed.* The temperature-induced dissociation of excitons results in an increase in the transition energy when the thermal energy matches the binding energy of the excitons [118]. Assuming an exciton binding energy of ≈ 50 meV in metallic nanotubes, this method appears to be promising to enable access to a variety of chiralities and transition energies. In order to apply this technique to semiconducting nanotubes, temperatures of the order of at least 3000 K would be necessary. However, this is beyond the thermal stability of nanotubes. A schematic picture is shown in Fig. 4.3 which presents the Stokes scattering process in carbon nanotubes. Since excitons are stable at room temperature, the optical transition is determined by excitons (denoted as E_{exc} in Fig. 4.3) . At higher temperatures, when the excitons are dissociated one expects a quasi band-to-band transition (denoted as E_{gap} in Fig. 4.3) and an increase in the optical transition energy.

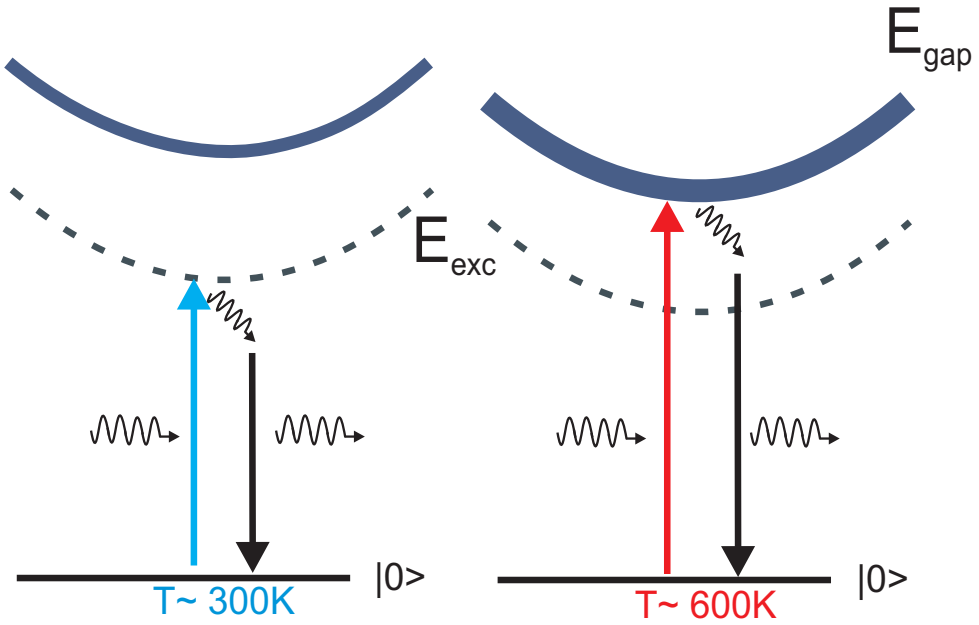

Figure 4.3: Schematic picture of the Raman process for excitonic (≈ 300 K) and quasi band-to-band transitions at higher temperatures (≈ 600 K). The dashed line represents an excitonic optical transition and the solid line represents a quasi band-to-band transition.

*P. May, H. Telg, G. Zhong, J. Robertson, C. Thomsen, and J. Maultzsch, "Observation of excitonic effects in metallic single-walled carbon nanotubes", Phys. Rev. B **82**, 195412 (2010).

4.2.1 Measurement and analysis procedure

Measurements were performed on vertically aligned single-walled carbon nanotubes. They were grown by chemical vapor deposition resulting in a diameter distribution between 0.5 and $2\,\mathrm{nm}$ [119, 120]. The excitation by dye lasers was carried out between 1.9 and $2.2\,\mathrm{eV}$. Within this range it is possible to use resonance effects for the determination of changes in the optical transitions as function of temperature. However, when acquiring Raman spectra with different excitation energies, the optical properties of the sample need to be taken into account, for example the reflection coefficients and changes in penetration depth. This is crucial in bulk materials particularly when progressing over a wide range in excitation energy. Since the excitation range is considerably small, it is sufficient to correct the acquired spectra by measuring $\mathrm{CaF_2}$. In the visible range $\mathrm{CaF_2}$ is non-resonant with a bandgap of $\approx 8\,\mathrm{eV}$. In a first approximation the determination of a resonance profile of $\mathrm{CaF_2}$ gives the response of the setup and compensates variations in the alignment. A more detailed analysis of the Raman susceptibility and its implications on the Raman intensity can be found in Ref. [121].
With the above mentioned excitation range it was possible to probe the first transition E_{11}^{M} of metallic nanotubes and the second transition E_{22}^{S} of semiconducting nanotubes. The according part of the Kataura plot is depicted in Fig. 4.4. The metallic and semiconducting nanotubes are highlighted in shaded red (metallic) and shaded blue (semiconducting) areas. By changing the excitation energy, resonance profiles are obtained when plotting the integrated area of each radial breathing mode.
The transition energies can be estimated by fitting the resonance profiles with [57],

$$I(E_l) = \left(\frac{\mathcal{M}c}{\hbar\omega_{\mathrm{RBM}}}\right)^2 \left| \frac{1}{(E_l - E_{ii} - i\Gamma/2)} - \frac{1}{(E_l - \hbar\omega_{\mathrm{RBM}} - E_{ii} - i\Gamma/2)} \right|^2 , \tag{4.7}$$

where $\mathcal{M}$ contains all matrix elements and c summarizes all remaining factors. E_l is the laser energy, E_{ii} is the energy of the allowed optical transition, and Γ the broadening of the intermediate electronic state. The first and second term represents incoming and outgoing resonance, respectively. Equation 4.7 describes Raman scattering for a single resonant intermediate state E_{ii}. This corresponds to an excitonic transition, where the wave vector of the optically created exciton $Q = k_e + k_h$ is fixed by the momentum of the incoming photon $k_i = Q \approx 0$ (k_e and k_h are the wave vector of the electron and hole, respectively).

4.2.2 Temperature dependence of the optical transition

The temperature dependence of the bandgap $E_g(T)$ has been investigated for years in classical bulk semiconductors and is one of the characteristic features of semiconductors [65]. $E_g(T)$ dependencies show a linear decrease at sufficiently high temperatures, whereas it is nonlinear at temperatures near $0\,\mathrm{K}$ [122]. The behavior of the temperature dependence of the electronic band is important for a variety of applications such as field electron transistors or optical emission devices [15]. Assignments of the nanotube chiral index *(n,m)* are often done by a comparison of experimental determined transition energies with theoretical predictions, which calculate the optical band-gap at zero temperature.

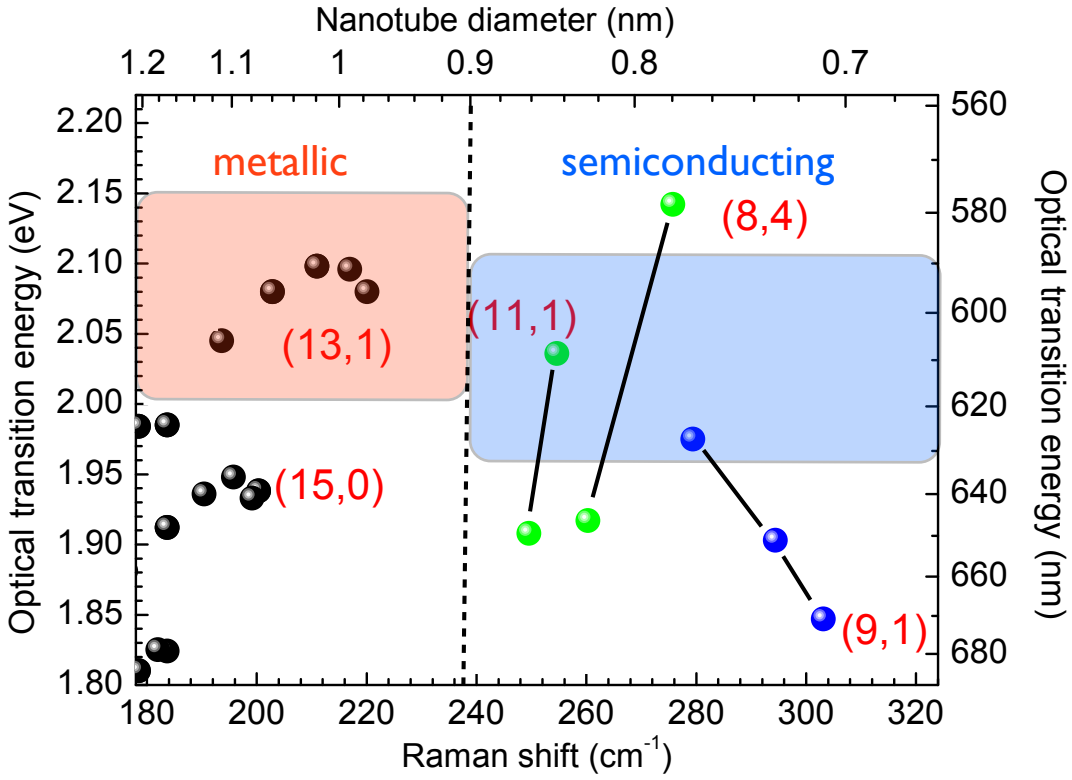

Figure 4.4: Relevant part of the Kataura plot, *i.e.* optical transition energies versus RBM frequency. The nanotube diameter is inverse proportional to the radial breathing mode frequency. The shaded red (metallic) and blue (semiconducting) areas show the approximate resonance windows, in which the resonantly enhanced Raman signal is expected.

In Fig. 4.5 the Raman spectra excited at 2.07 eV for three different temperatures is shown. The upper temperature limit was 770 K for the semiconducting tube. At higher temperatures, the intensity was too weak to resolve the RBM peaks separately.

Several radial breathing modes (RBMs) around $210\,\mathrm{cm}^{-1}$ and $250\,\mathrm{cm}^{-1}$ are observed. A first rough assignment can be made by considering the excitation energy and comparing it to the Katauraplot in Fig. 4.4. Thus, the first group of peaks can be assigned to metallic and the latter to semiconducting nanotubes [43]. Overall, the absolute RBM intensity decreases with increasing temperature. However, the relative intensities of different peaks change as can be seen at around $240\,\mathrm{cm}^{-1}$, where the relative peak intensity increases in comparison to peaks at around $210\,\mathrm{cm}^{-1}$. This variation is due to a change of the optical transition energy E_{ii} with temperature. In the following analysis this behavior is examined by studying resonant Raman profiles. Focus is applied to one RBM of each nanotube species, each with the strongest Raman signal, the metallic tube at $213\,\mathrm{cm}^{-1}$ and the semiconducting tube at $252\,\mathrm{cm}^{-1}$. Following the systematics described in Ref. [43], the RBM at $252\,\mathrm{cm}^{-1}$ is assigned to the semiconducting *(11,1)* tube

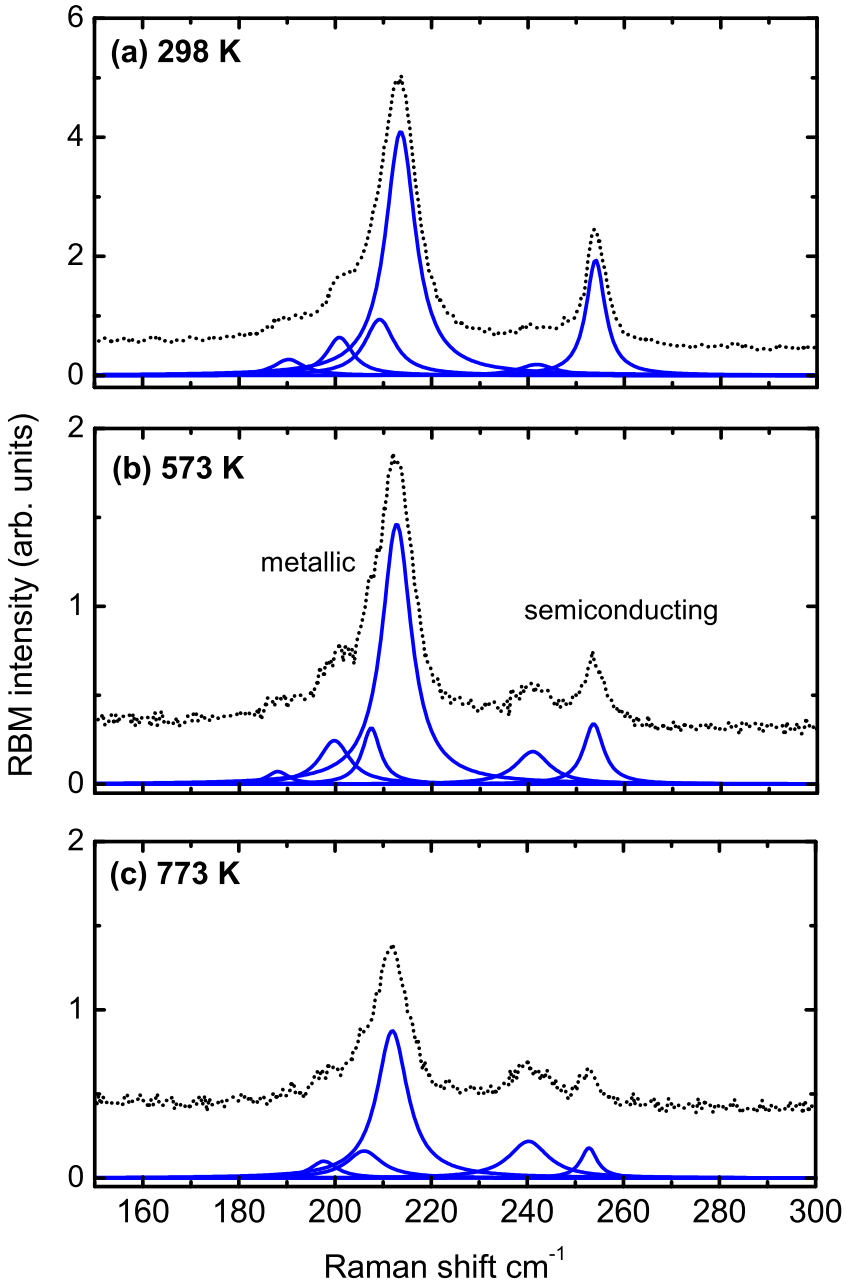

Figure 4.5: RBM spectra of single-walled carbon nanotubes for different temperatures excited at 2.07 eV. Solid lines indicate Lorentzian fits to the experimental data. The RBM intensity (intensity units between among the individual plots can be compared) decreases as the temperature increases.

excited into the second optical transition E_{22}^S. The *(11,1)* tube belongs to the $\nu = +1$ family with $\nu = (n-m)\,mod3$. The RBM at 213 cm^{-1} is assigned to the metallic *(13,1)* tube excited into the first optical transition E_{11}^M.

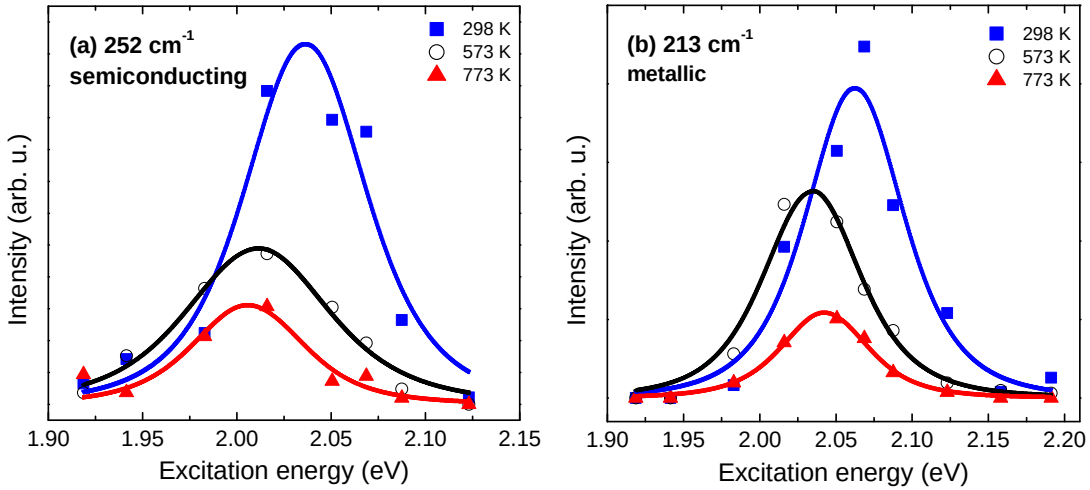

Figure 4.6: Raman resonance profiles of the radial breathing mode of a semiconducting nanotube (a) and for a metallic nanotube (b) at different temperatures. Solid lines are fits to the experimental data, which are represented by symbols.

Figure 4.6 (a) shows the resonance profile of the semiconducting *(11,1)* tube for three different temperatures. As expected for a semiconductor, a shift of the resonance profile is observed. The transition energy is shifted to lower energies as the temperature increases [122–124]. Figure 4.6 (b) shows the resonance profiles of the metallic *(13,1)* nanotube for the same temperatures. A monotonic shift similar to the semiconducting nanotube is observed. In order to study the difference between the temperature dependence of the transition energies in semiconducting and metallic nanotubes, resonance profiles from the *(13,1)* shown in Fig. 4.7 and the *(11,1)* nanotube shown in Fig. 4.8 at various temperatures are collected. While the semiconducting tube shows a monotonic downshift across the entire temperature range, the metallic tube shows a sudden upshift of the transition energy above ≈ 570 K. Below this temperature a monotonic downshift of E_{ii} for the metallic nanotube is also observed. The monotonic decrease of the transition energy with temperature in semiconducting nanotubes and in metallic nanotubes up to ≈ 570 K has been argued and a tentative linear fit to the data is possible, which yields a redshift of -6.38×10^{-5} eV K^{-1} for the semiconducting tube. The downshift of the transition energy can be explained by the temperature dependence of optical transitions and the softening of the bandgap at higher temperatures due to lattice expansion and electron-phonon coupling [125, 126]. Downshifts of E_{ii} in carbon nanotubes based on the electron-phonon coupling model were presented in Refs. [125] and [127]. In these calculations, however, excitonic effects and the characteristics of temperatures above 600 K were not shown. Table 4.1 shows a comparison of the results with other experimental and theoretical data. For the semiconducting tube, reasonable agreement with the predicted shift of approximately -4.4×10^{-5} eV K^{-1} for the E_{11} transition in the *(11,1)* tube [125] and with experimental data of Cronin *et al.* [126] is found. In Ref. [126] the experimental data were not assigned to a particular *(n,m)* tube. The calculated shifts in [126] for the

metallic nanotubes are in the range of -6.0 to -8.8×10^{-5} eV K^{-1}. The result of -9.30×10^{-5} eV K^{-1} up to 570 K is in reasonable agreement. The slightly different value can be attributed to the analysis of different chiral indices.

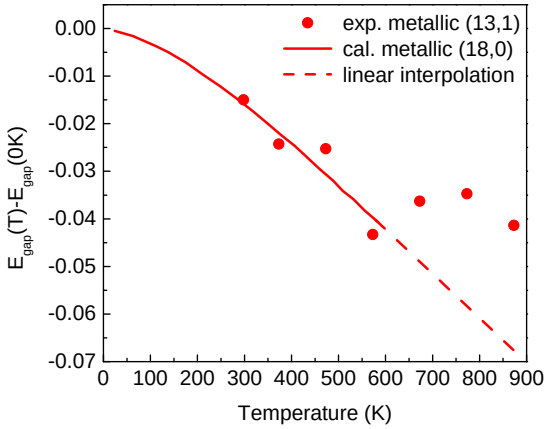

Figure 4.7: Temperature dependence of the optical transition for the metallic $(13, 1)$ nanotube. The dots are experimental data from the $(13, 1)$ nanotube, the solid line is a calculation taken from Ref. [126] for a metallic $(18, 0)$ nanotube for temperatures up to 600 K. The dashed line is a linear interpolation for higher temperatures.

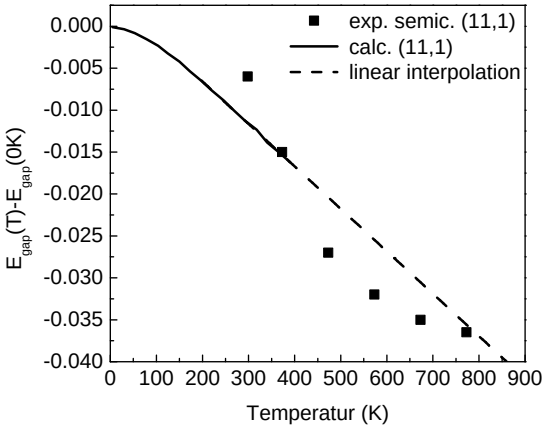

Figure 4.8: Temperature dependence of the optical transition for semiconducting nanotubes. The dots are experimental data from the $(11, 1)$ nanotube, the solid line is a calculation taken from Ref. [125] for the same nanotube for temperatures up to 400 K. The dashed line is a linear interpolation for higher temperatures.

In order to examine how thermal expansion contributes to the shifts, two scenarios are discussed. First, the case of non-isotropic expansion of the nanotube is considered, following Eq. (4.8) of Ref. [126] for the shift ΔE_{ii} in transition energy:

$$\Delta E_{ii} = -2E_{ii}\epsilon_r - 3\gamma_0(-1)^i(-1)^\nu(\epsilon_r - \epsilon_z)cos(3\Theta) \tag{4.8}$$

where ϵ_r and ϵ_z are the radial and axial strain, Θ is the chiral angle, γ_0 (2.9 eV) is the next nearest neighbour hopping matrix element of the tight binding model and ν is $+1$ for both the metallic and semiconducting nanotube in our case. If the values for radial and axial expansion of Ref. [128] are inserted for the metallic $(10, 10)$ nanotube a transition energy shift of 1.5×10^{-5} eV K^{-1} is obtained. This is approximately six times less than our shift and in the opposite direction. Second, an isotropic thermal expansion for the metallic tube with a (negative) thermal expansion coefficient similar to graphite (-1.0×10^{-6} K^{-1}) can be assumed. This would also result in an upshift of transition energy with increasing temperature, and the value of $\approx 4 \times 10^{-6}$ eV K^{-1} is one order of magnitude smaller than that measured. Indeed, the thermal expansion coefficient of graphite changes sign in approximately the same temperature range as the sign change observed in the E_{11}^M shift. However, the sign of the E_{11}^M shift observed in the experiment is opposite to what would be expected from the graphite thermal expansion.

Therefore, it can be assumed that the effect of thermal expansion is negligible for the interpretation of the experimental results. A similar conclusion was obtained in Ref. [125] for the bandgap of semiconducting tubes.

Now the question is addressed whether the assumption to directly compare the temperature dependence of E_{ii} and E_g is vindicated. The temperature dependence can be explained as follows: at room temperature optical transition in carbon nanotubes differ from the single particle energies due to bandgap renormalization [114] and excitonic effects. However, the bandgap renormalization and excitonic effects rather depend on the dielectric environment than temperature [38, 39, 126]. Therefore single particle energies are the determining factor in the behavior of $E_{ii}(T)$. Thus direct comparison between the temperature dependent shift of $\Delta\, E_{ii}(T) \,/\, \Delta\, T$ and $\Delta E_g(T) \,/\, \Delta\, T$ is applicable. All things considered the small shifts of $E_{ii}(T)$ do not strongly affect assignments of nanotubes to specific (n, m).

Table 4.1: Temperature dependence of the transition energy from experiments and theory. We assumed the shifts to be linear for the temperature region above 298 K, disregarding the non-linear behavior at low temperatures for the comparison with other results.

tube	range (K)	shift (eV K^{-1})	method
This work			
(11,1)	298 - 773	-6.38×10^{-5}	Raman
(13,1)	298 - 573	-9.30×10^{-5}	Raman
Ref. [125]			
(11,1)	0 - 600	-4.4×10^{-5}	calc.[a]
Ref. [126][b]			
$\nu = -1$	300 - 573	-11.7×10^{-5}	Raman
$\nu = -1$	300 - 573	-4.1×10^{-5}	Raman
179cm^{-1} (met.) [c]	300 - 573	-7.1×10^{-5}	Raman
160cm^{-1} (met.) [c]	300 - 573	-2.5×10^{-5}	Raman
(10,0)	300 - 573	-9.2×10^{-5}	ext.-TB [d]
(10,2)	300 - 573	-7.5×10^{-5}	ext.-TB [d]
(11,0)	300 - 573	-7.3×10^{-5}	ext.-TB [d]
(13,0)	300 - 573	-6.1×10^{-5}	ext.-TB [d]
(11,0)	300 - 573	-7.3×10^{-5}	ext.-TB [d]
met.E_{11}^{-} [e] (18,0)	300 - 573	-8.8×10^{-5}	ext.-TB [d]
met.E_{11}^{+} [e] (18,0)	300 - 573	-6.0×10^{-5}	ext.-TB [d]
Ref. [129][f]			
(7,6)	5 - 300	-5.0×10^{-5}	PL [g]
(9,8)	5 - 300	$\approx -1.1 \times 10^{-5}$	PL
(12,2)	5 - 300	-3.0×10^{-5}	PL

[a] Frozen-phonon calculation of the electron-phonon coupling for E_{11}^{S}.
[b] Experimental data from individual suspended nanotubes.
[c] The RBMs were not assigned to a specific nanotube, but to one out of $(18,0)$, $(19,1)$, $(12,12)$, or $(14,8)$ [126].
[d] Extended-tight binding calculation.
[e] Corresponds to the splitting of the first transition in metallic tubes.
[f] (7,6) and (9,8) are individual tubes; (12,2) is from a pillar suspended ensemble.
[g] Experimental photoluminescence data of E_{11}^{S}.

4.2.3 Determination of the exciton binding energy

In this subsection the exciton binding energy is determined. A closer look is taken at the increase in transition energy of the metallic nanotube above $\approx$ 570 K. This behavior is explained in terms of excitons which are dissociated into free electron-hole pairs at temperatures related to the exciton binding energy [118]. When the excitons dissociate, the excitonic transition is no longer dominant but that of the free-particles. After all excitons are dissociated, the optical transition again shifts down in energy due to electron-phonon coupling. The reason why an upshift for the semiconducting tube is not observed is that the thermal energy is not sufficient to break excitons, which have binding energies of several hundred meV [98, 99]. There are two possibilities to derive the exciton binding energy from the temperature-dependent shift of the transition energy. The first is the starting point of the blueshift at 570 K. This temperature corresponds to an energy of around 50 meV, which is in agreement with theoretically predicted values of the binding energies in metallic nanotubes [116, 127, 130].

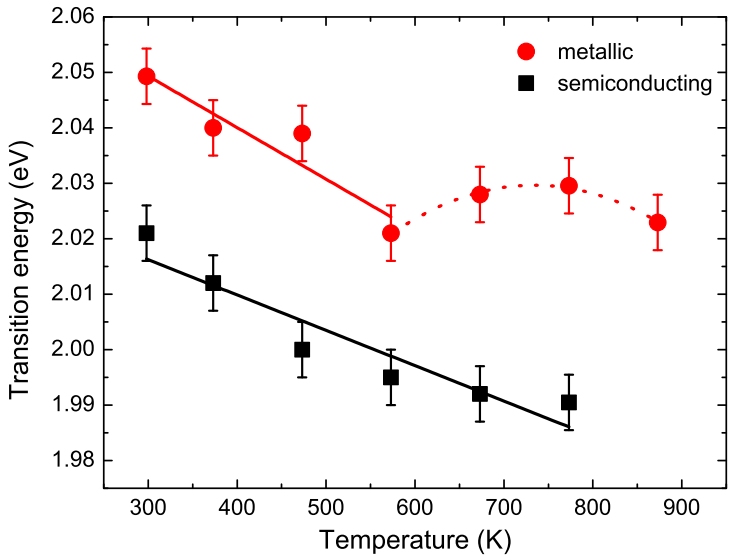

Figure 4.9: Experimental transition energies E_{ii} as a function of temperature for metallic and semiconducting nanotubes. The solid lines are linear fits to the data. The dotted line is a guide to the eye.

The value of 50 meV was also deduced from absorption measurements into the second optical transition E_{22} of an individual *(21,21)* nanotube [100]. However, this nanotube had approximately twice the diameter compared to the tube in the experiment. Since the exciton binding energy is predicted to be diameter dependent [97, 111, 114], even higher binding energies in the experiment should be expected. On the other hand, the development of the exciton binding energy in higher optical transitions is still under discussion. Refs. [130, 131] suggest increasing binding energy in higher optical transitions, while Refs. [61, 109] suggests different exciton behavior for E_{33} and E_{44} than for E_{11} and E_{22}. Therefore, the dependence of the exciton binding energy on the transition might partly compensate the diameter dependence of the exciton binding energy.

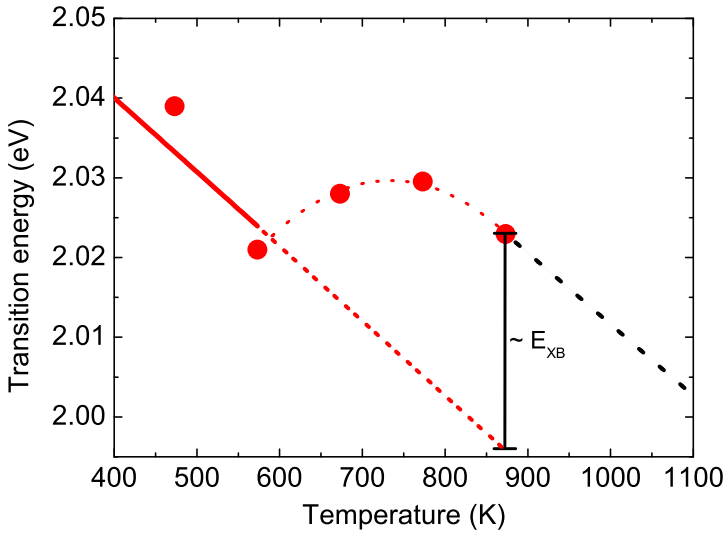

Figure 4.10: Extrapolation of the linear fit to the transition energies of the metallic tube from Fig. 4.9 (lower red dashed line) and estimation of the upshift of this line above 850K. The vertical bar indicates the exciton binding energy E_{XB}.

The other possibility to estimate the exciton binding energy from the data is the difference between the initial linear fit (red dashed line) of the metallic transition energy and the downshift at temperatures above 850 K (black dashed line), which is shown in Fig. 4.10. Without dissociation of excitons, a further linear downshift (red dashed line) would be expected at temperatures above 570 K. The difference between this line and the experimental data is therefore another measure for the exciton binding energy of the metallic nanotube. A binding energy derived from Fig. 4.10 is estimated to be approximately 27 meV. However, it is not known whether the temperature shift of the bandgap (non-interacting electron-hole pairs) and of the excitonic energies are the same.

4.2.4 Absorption spectrum of a metallic carbon nanotube

Here, calculations of absorption spectra are considered for the metallic $(13, 1)$ nanotube. The data were provided by E. Malic (TU Berlin) and published in Ref. [130]. The calculation method is based on a microscopic approach of density matrix theory and combining it with the zone-folded tight-binding wavefunction. The absorption spectra are shown in Fig. 4.11 for the metallic $(13, 1)$ nanotube. The blue spectrum includes all Coulomb interactions, i.e. electron-hole and electron-electron interactions, and the red dashed absorption spectra represents the behavior when the electron-hole interaction is eliminated. The spectra show both the first and the second optical transition. When the electron-hole interaction is missing, the optical transition shifts to higher energies. This is correlated to the dissociation of excitons in our experiment and strongly supports our interpretation. The absorption spectra are not symmetric, since they exhibit a contribution on the high-energy side. This is in agreement with Ref. [100] and can be attributed to an absorption of the continuum. The shift of the excitonic and single-particle absorption is ≈ 78 meV and in good agreement with our result. Further these calculations imply that the oscillator strength is fully restored in the continuum when excitons are dissociating. The absorption amplitude decreases by a factor of 1.62.

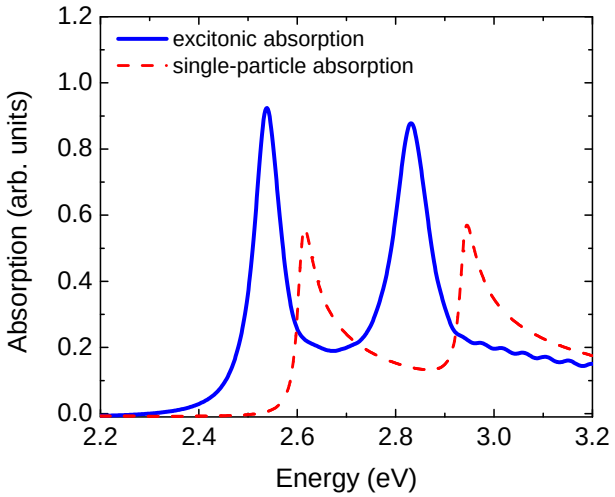

Figure 4.11

Calculated absorption spectra of the $(13, 1)$ metallic carbon nanotube. The blue solid line represents the absorption spectra including electron-hole and electron-electron interaction, the red dashed line shows the absorption spectra excluding excitonic effects. Data are provided from Ref. [130].

4.2.5 Correlation of Raman intensity and oscillator strength

To treat the behavior of the oscillator strength theoretically the following approach is considered. The exciton oscillator strength is inversely proportional to the intrinsic radiative decay rate w_{in} or directly proportional to the radiative lifetime τ_{eff}. The intrinsic lifetime τ_{in} and the effective radiative lifetime τ_{eff} are related for low temperatures by [132, 133]:

$$\tau_{\mathrm{eff}} \approx \frac{3}{4}\sqrt{\pi}\sqrt{\frac{k_B T}{\Delta}}\tau_{\mathrm{in}}, \tag{4.9}$$

where Δ is the maximum energy for a radiatively decaying exciton.

First, a look at the temperature dependence of the oscillator strength is considered. Perebeinos *et al.* [134] pointed out that the effective radiative decay rate w_{eff} can be approximated by $w_{\mathrm{eff}} \propto T^{3/2}$. Therefore the oscillator strength scales with $T^{3/2}$. This is valid under the assumption of optical transitions that are determined by excitons and was calculated for semiconducting nanotubes. Since at higher temperature the excitons dissociate one has to reconsider these discussions and treat the oscillator strength as function of temperature and exciton binding energy. In the case of metallic nanotubes, Wang *et al.* [100] showed in the analysis of the absorption measurements the existence of absorption of the continuum, which was not observed for the semiconducting tubes due to higher binding energies and consequently a full transfer of the oscillator strength to the exciton.

An approach is a scaling relation for the exciton oscillator strength: [111]:

$$\frac{I_1}{I_0} \propto \epsilon/Rm \tag{4.10}$$

where R is the exciton radius constant, m the effective mass and I_0 is the spectral weight of the first band for non-interacting particles. This indicates for $\epsilon \to \infty$ that the spectral weight of the first band for non-interacting particles (I_0), i.e. the band edge becomes infinite. Applied to the results of the metallic nanotubes it indicates, that the oscillator strength is transferred back to the band edge.

Further evidence for the dissociation of excitons in metallic nanotubes can be found within the temperature dependent Raman intensity, which is proportional to the square of the oscillator strength of the corresponding optical transition. The absorption calculation gives evidence for a decrease in intensity. In Fig. 4.12 the RBM intensity is plotted at the maximum of the resonance profile of the semiconducting and the metallic nanotube. In principle, the width of the resonance profiles should be taken into account, however, a systematic dependence of the broadening parameter Γ on temperature was not observed, as the values scatter widely. The values range from $85\,\mathrm{meV}$ to $110\,\mathrm{meV}$ for the metallic and from $90\,\mathrm{meV}$ to $140\,\mathrm{meV}$ for the semiconducting nanotube.

For both the metallic and the semiconducting nanotube a decrease of the maximum intensity with increasing temperature was noted. A general decrease can be explained by an increase of the lifetime broadening of the excitonic states [134]. The broadening, in turn, leads to a decrease of the maximum Raman intensity in the resonant Raman process [135]. This however does not explain the rapid decrease

of the maximum intensity of the metallic *(13,1)* tube, which was observed between 570 K and 670 K. Comparing the absolute values between 570 K and 770 K, the intensity of the metallic tube decreases by a factor of 2.92 while the one of the semiconducting decreases only by a factor of 1.60. It has been predicted that excitonic transitions in carbon nanotubes are in general stronger than band-to-band transitions [130, 136], i.e. excitonic effects enhance the optical matrix elements and thus the resonance Raman intensity. Therefore the rapid decrease of the Raman intensity of the metallic tube can be explained by the dissociation of excitons at $\approx$ 50 meV. The rapid decrease is further confirmed by calculated absorption spectra, which were shown in Fig. 4.11. The amplitude decreases by a factor of 1.62. Since the Raman intensity is proportional to the square of the absorption (if the strength of absorption and emission is assumed to be equally), the amplitude would decrease the intensity by a factor of 2.90, which is in excellent agreement with our value.

Next, the oscillator strength is related to the Raman intensity. The experimentally observed exciton oscillator strength is, as outlined previously, inversely proportional to the effective decay rate w_{eff} or directly proportional to the lifetime τ_{eff}. At low temperatures, the effective radiative lifetime in semiconducting carbon nanotubes has a square root temperature dependence [132, 133]. At higher temperatures (above $\approx$ 60 K), Perebeinos *et al.* [134] showed that the temperature dependence of the decay rate can be approximated by $w_{\text{eff}} \propto T^{3/2}$. As the Raman intensity is proportional to the square of the oscillator strength (f), it can be expected to depend as T^{-3} on temperature.

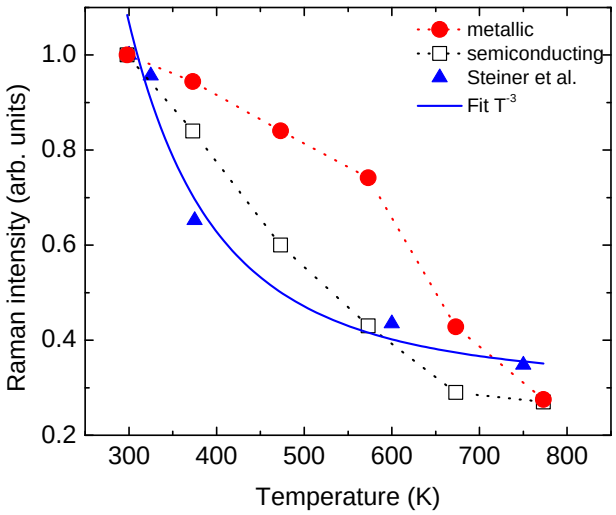

Figure 4.12

Maximum of the resonance profile (i.e. the areal intensity of the RBM peak in full resonance) as a function of temperature for semiconducting (black squares) and metallic (red dots) nanotubes. The semiconducting values are fitted with $f^2 \propto T^{-3}$ and compared with results of Ref. [137] (blue triangels). The values of the intensity are normalized to the intensity at 300 K for better graphical representation. Dashed lines are guides to the eyes.

In Fig. 4.12 a fit of $f^2 \propto T^{-3}$ to the RBM maximum intensity of the semiconducting tube is shown. Reasonable agreement is found although our data are less steep than the $f^2 \propto T^{-3}$ fit. This might be due to symmetry breaking resulting in scattering between optically allowed and forbidden exciton states [134]. In this case the temperature dependence of f deviates from the T^{-3} behavior [134]. Moreover, the calculations in Ref. [134] were done for the lower transition E_{11}^S of semiconducting nanotubes, whereas our measurements are for the second transition E_{22}^S. Due to additional decay channels [138], the

temperature dependence of the oscillator strength is expected to be different in E_{22}^S from that in E_{11}^S. The areal intensity of the RBM peak in full resonance with recent data on electrically induced heating of an individual tube (triangles in Fig. 4.12) is compared [137]. These data agree quite well with the T^{-3} fit. Possible reasons for the differences between this data and the data of Ref. [137] can be due to different conditions concerning the optical transition (E_{22}^S vs. E_{33}^S) and environmentally vs. electrically induced heating. Furthermore interactions among the tubes might change the oscillator strength. However, the RBM of Ref. [137] showed similar E_{ii} shift rates as the semiconducting nanotube investigate above.

4.3 Multiphonon Raman scattering in carbon nanotubes

In this section multiphonon Raman scattering in CVD-grown single-walled nanotubes up to 6000 cm^{-1} is considered. First, the measurement and intensity calibration procedure are explained and the results are compared to individual carbon nanotubes and graphite. The relative strengths of higher order modes compared to the G mode are found to be between individual carbon nanotubes and graphite. This is attributed to the one-dimensional excitonic enhancement of higher-order modes and ensemble effects.

4.3.1 Measurement and intensity calibration procedure

The multiphonon Raman measurements were performed using a Mc Pherson UT-3 triple monochromator setup at the Institute of Applied Physics at the University of Hamburg. This setup is located in a climate-controlled cleanroom to ensure stability during long time measurements [139]. The all-reflecting, fully achromatic objective consists of four on-axis parabolic mirrors with a large solid angle, which ensures the detection of Raman signal scattered in all directions. Most of the mirrors are off-axis paraboloids. This ensures small focuses and suppresses chromatic aberrations. The excitation at 357 nm (3.47 eV) was obtained with a Ti:sapphire laser with a repetition rate of 80 MHz. The Ti:sapphire is pumped by a diode laser with a wavelength of 532 nm and the spectral range is between 700 nm and 1000 nm. These wavelengths can then be doubled and tripled. The pulse width was ≈ 2 ps. Since the Raman spectrum was taken over a wide range covering $\approx 10000\,\mathrm{cm}^{-1}$, the spectra have to be normalized to the system response. The corrected and normalized intensity I_{raw} is given by:

$$I_{raw}(\omega) = \frac{\big(I_m(\omega, t_{int}) - I_{bg}(t_{int})\big)}{I_{cww}(\omega)} \quad \cdot \quad \frac{t_{norm} \cdot P_{norm}}{t_{int} \cdot P_m}. \tag{4.11}$$

The first term represents the correction, the second term the normalization of the measured intensity $I_m(\omega, t_{int})$ with integration time t_{int} and power P_m. First the background $I_{bg}(t_{int})$ is subtracted. This signal is due to noise of the CCD-sensor. Further the intensity requires to be normalized to the power P_m and the integration time t_{int}. The most important part is the white light correction $I_{cww}(\omega)$, which represents the sensitivity of the setup depending on the measured spectral range and polarization. The calibration were performed with two Ulbricht spheres covering the visible and UV range. The advantage of the Ulbricht sphere is that it generates a homogeneous radiation field. This analysis procedure ensures that the intensities of several peaks can be directly extracted from the spectra without any further normalization or correction.

4.3.2 Multiphonon analysis

Figure 4.13 shows the Raman spectra of the as-grown nanotube ensemble obtained with 357 nm excitation energy up to 10000 cm^{-1}. The figure shows two insets with zoomed areas of higher order Raman modes. Most of the peaks can be assigned to different combinations of either the G mode (Γ-point phonon) or phonons in the vicinity of the K-point or combinations of both. Several combinations are allowed under the condition that the total momentum in the Raman process is zero.

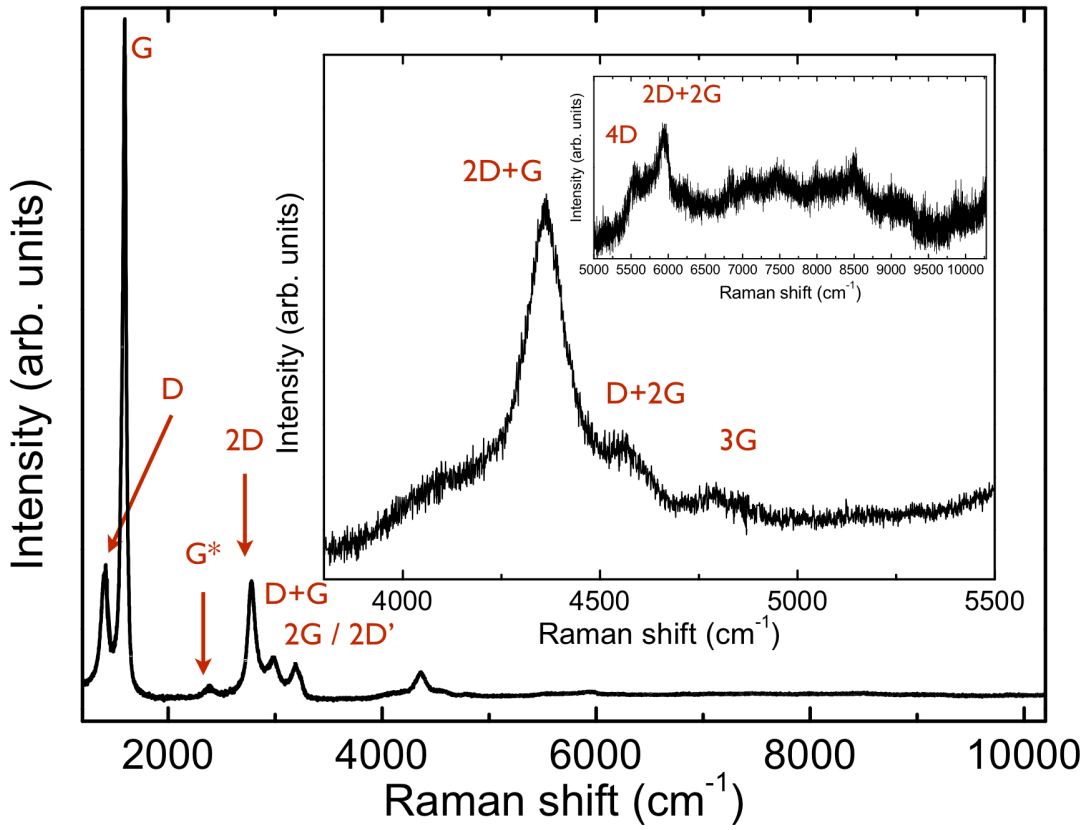

Figure 4.13: Multiphonon Raman spectra of as-grown single-walled carbon nanotubes.

Table 4.2 shows the experimental obtained frequencies of several multiphonon modes compared to what would be expected from combinations of the fundamental G and D mode. The work of Wang *et al.* found discrepancies in the frequency of up to 50 cm^{-1} due to an experimental resolution of $\approx 30\,\mathrm{cm}^{-1}$ [140]. The largest deviation is at combinations where a mixture of several combination modes and the G^- and G^+ mode, respectively, exist. Since the G^+ gives the dominant contribution the expected shifts of the G^+ combination modes were analyzed. Overall an excellent agreement of the measured and expected

Table 4.2: Combinations of the fundamental G and D mode. The G mode is splitted into G^- and G^+. The experimental shifts are compared to the expected shifts, which were calculated from the fundamental modes. However, at higher frequencies only the stronger G^+ mode is assigned to contribute to the modes.

Raman mode	Experiment (cm^{-1})	Expected multiphonon shift (cm^{-1})
D	1390	-
G^-	1570	-
G^+	1595	-
$2D$	2780	2780
D+ G^+	2990	2985
$2G^+$	3190	3190
$2D$+ G^-	4360	4350
$2D$+ G^+	4360	4375
D+$2G^+$	4570	4580
$3G^+$	4788	4785
$4D$	5558	5560
$2D$+$2G^+$	5939	5920

multiphonon frequencies was obtained.

Now turning to the discussion of relative intensities of the G^+ mode, where the absolute Raman intensity will be considered and discussed. Figure 4.14 compares the relative strengths of several multiphonon modes in as-grown (this work), individual carbon nanotubes [140] and graphite [141]. Figure 4.15 shows the same data, but averaged in case of the individual carbon nanotubes for better graphical representation. The work of Wang *et al.* [140] investigated the multiphonon features with individual carbon nanotubes at two different wavelengths. The relative intensities of individual carbon nanotubes are in general higher than that of the as-grown carbon nanotubes. The relative high strength in higher order Raman modes was attributed to enhanced one-dimensional excitonic transitions compared to optical transitions in three-dimensional graphite. The different intensities of different chiralities can be attributed to different resonance conditions of higher order Raman modes. This is ruled out in the as-grown carbon nanotube sample, since one probes a variety of different chiralities. One would expect a falloff in intensity when progressing to higher order modes. This falloff is different for the three samples, weak for individual carbon nanotubes and strong for graphite. The as-grown nanotubes are in between the two. However, the characteristics when progressing to higher orders and different combinations are similar.

To get a more quantitative understanding of the Raman probability and the influence of the matrix elements is discussed. The Raman scattering probability is recalled from Eq. 3.24 and simplified to the process of a phonon in the vicinity of a single exciton state [65]:

$$P_{ph}(\omega_s) = \left(\frac{2\pi}{\hbar}\right) \left| \frac{< 0|H_{er}(\omega_i)1 >< 1|H_{e-ph}|1 >< 1|H_{er}(\omega_s)|0 >}{(E_1 - \hbar\omega_{i,0} - i\Gamma_1)(E_1 - \hbar\omega_{s,n} - i\Gamma_1)} \right|^2, \tag{4.12}$$

where H_{er} and H_{e-ph} is the electron-photon and the electron-phonon coupling, respectively. E_1 is the

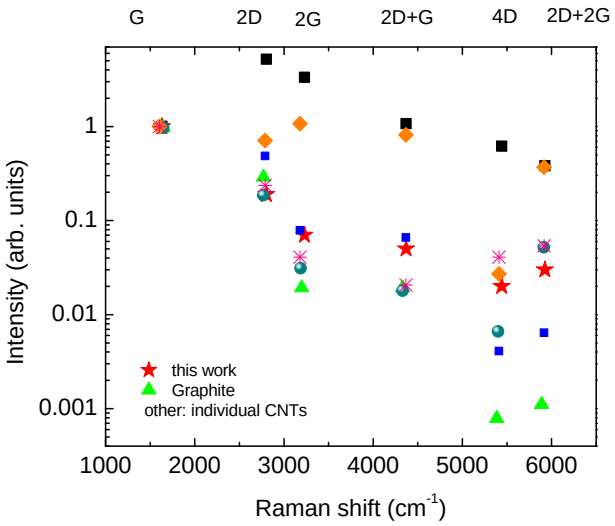

Figure 4.14

Comparison of relative strengths of several multiphonon modes in as-grown (this work), individual carbon nanotubes [140] and graphite [141]. The G mode intensity is normalized to 1.

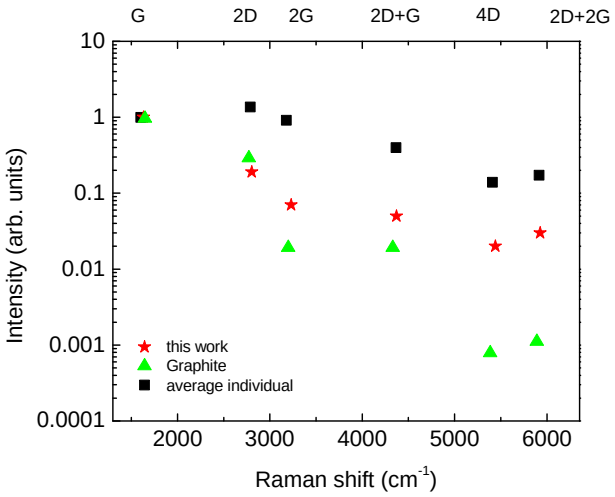

Figure 4.15

Comparison of relative strengths of several multiphonon modes in as-grown (this work), individual carbon nanotubes [140] and graphite [141]. The G mode intensity is normalized to 1. The intensities of five different chiralities is averaged for comparison and better graphical representation.

excitation energy and $\hbar\omega_{x,n}$ describes the energy of the electronic excitation with n phonons. This equation illustrates the importance of resonance factors contributing to the Raman intensity. In carbon nanotubes one has sharp electronic van-Hove like transitions in the single-particle picture or strong excitonic transitions in the case of semiconducting nanotubes. Excitons have been shown to be the dominant transition in single-walled carbon nanotubes [44, 98–100]. In graphite on the other hand, optical transitions are not determined by sharp transitions. Therefore this should find expression in the matrix elements of Eq. 4.12.

Further the relative strength of the Raman modes is proportional to the exciton-phonon coupling. The measurement of ensemble nanotubes at a certain excitation energy provides only access to some chiralities which are in the particular resonance window of the transition. This is also the reason for the

strong deviations among different individual carbon nanotubes from Ref. [140]. The ratio of fundamental Raman modes to its overtones depends strongly on the exciton-phonon coupling [142]. However, this coupling deviates largely as function of the chirality (n, m) of the corresponding nanotube [121, 136, 143, 144]. Therefore the results of as-grown nanotubes provide information about averaged exciton-phonon coupling effects. Results shown in Fig. 4.15 imply that excitonic effects are relevant in ensemble nanotubes. These effects seem to be stronger for individual carbon nanotubes and absent in three-dimensional graphite underlining the importance of excitons. However, in order to draw strong conclusions from the multiphonon Raman spectra, one needs to perform temperature dependent measurements on individual carbon nanotubes. Thereby, definite conclusions concerning the coupling strengths of the exciton-phonon coupling can be derived.

4.4 Summary

The excitonic binding energy has been determined in metallic carbon nanotubes. For this purpose, a new sensitive technique was applied in an ensemble of carbon nanotubes. By monitoring the optical transition as a function of temperature, contrasting behaviors of semiconducting and metallic nanotubes were observed. The dependence on the optical transition of the metallic carbon nanotube showed an increase in energy. This was attributed to the dissociation of excitons. The value of the exciton binding energy was found to be $50\,\mathrm{meV}$ and is in close agreement with theoretical calculations and absorption measurements. The oscillator strength was discussed in the context of the results. For metallic tubes, to the best of our knowledge, no temperature dependent calculations of the oscillator strength in E_{11}^{M} have been reported so far. It has been shown in Ref. [100] that due to their reduced exciton binding energies, metallic tubes exhibit a contribution of continuum transitions in their absorption spectra. The oscillator strength is thus distributed over both the excitonic and the continuum transition. The results suggest that at temperatures above 570 K, the oscillator strength is fully restored in the continuum transition. The results underline the crucial importance of considering excitonic effects in the optical spectra of metallic single-walled carbon nanotubes. At temperature above the thermal stability of the exciton the optical response ought to be analyzed in consideration of uncorrelated electron-hole pairs, i.e. band-to-band transitions instead of excitons, since the optical oscillator strength is transferred back to the ”band edge”. Multiphonon Raman spectroscopy gave further evidence for an enhanced exciton-phonon coupling compared to graphite. Here, enhanced Raman overtones were found compared to graphite and attributed to the strong excitonic transitions.

5 Double-resonant Raman scattering in graphene

This chapter deals with the double-resonant process in graphene and few-layer graphene. The double-resonant Raman process reveals insights into the electronic bandstructure and phonon dispersion of carbon systems. However, the contributing scattering paths are currently under discussion in literature about whether so-called $inner$ or $outer$ processes are dominant. When considering scattering paths along the high-symmetry direction, $inner$ processes yield electronic excitations between the K-M direction, whereas $outer$ processes yield electronic excitations between the Γ-K direction. In the first part the dominant electronic transitions in the $2D$ mode of free-standing bilayer graphene are studied.
Free-standing graphene allows to probe the intrinsic bandstructure and phonon dispersion without the influence of the underlying substrate. Taking into account the $inner$ and $outer$ processes, one would expect at least four distinct peaks to appear in the spectra for the $2D$ mode. In Ref. 145 the dispersion of the $2D$ mode on supported bilayer graphene was investigated and interpreted as a result of symmetric and antisymmetric transitions of $outer$ processes [145]. In Ref. 92 the data of Ref. 145 were then reanalyzed assuming only $inner$ symmetric and antisymmetric processes. Very recently, full two-dimensional integrations including matrix elements were reported for single-layer graphene, emphasizing the relevance of contributions from different directions in the Brillouin zone [89,90] or of dominant contributions from $inner$ processes [88]. Hence, the role of different contributions to the double-resonance process is still under discussion and needs further investigation.
Bilayer graphene exhibits a different electronic structure and therefore provides another excellent referencing system for studying the scattering processes. Both the Raman frequencies and the relative intensities for different excitation energies are discussed. Reasonable explanations for the contributions made by both $inner$ and $outer$ processes are found when assuming contributions along the high-symmetry line. In addition, the strengths of the measured Raman intensity is explained. The discussion is further extended to a two-dimensional calculation of the Raman cross section, discussing the terms of $inner$ and $outer$ processes.
Then the origin of the transverse optical (TO) and longitudinal acoustic (LA) combination mode is investigated with regard to the asymmetric lineshape, the evolution with the number of layers and excitation energy. It is shown that this mode allows the direct measurement of dominant electronic transitions in the two-dimensional Brillouin zone and addresses the question of dominant scattering paths. Then the $2D$ mode is investigated over a broad range of excitation energies exceeding the ultraviolet (UV) region and is compared to a one-dimensional calculation of the Raman cross section.

5.1 Introduction and theoretical framework

In this section the underlying procedural methods for the substrate and sample preparation are explained. Further the theoretical methods for the determination of the electronic structure and the phonon dispersion are presented, which are used for the calculation of the Raman cross section.

5.1.1 Exfoliation of free-standing graphene

The free-standing bilayer graphene sample was produced by micro-mechanical cleavage of graphite on a 10×10 mm^2 Si/SiO_2 substrate. Before, arrays of trenches were fabricated into p-doped Si [(100) orientation, $(525 \pm 25)\,\mu$m in thickness] covered with 100 nm thick SiO_2 layer. In a first step the Si-wafer was treated with a photoresist. The trenches were then obtained by conventional ultraviolet lithography and surface etching with reactive-ion etching. This process guarantees that etching occurs vertically anisotropically through the substrate. A high ratio between the depth and the width of the trench is therefore obtained. The width of the trench is $3\,\mu$m, the depth about $25\ \mu$m; the trenches are separated by $60\,\mu$m from each other. Graphene was identified first by optical contrast as shown in Fig. 5.1 [146]. The flakes of bilayer thickness were then confirmed through Raman measurements of the $2D$ mode [93,147]. Raman spectroscopy was performed under ambient condition in backscattering geometry at 441 nm (2.81 eV), 488 nm (2.53 eV), 532 nm (2.33 eV), 633 nm and (1.96 eV) with a $100\ \times$ objective and NA of 0.95. The spectra were obtained with a spectral resolution of $\approx 1\text{cm}^{-1}$. No laser induced shifts were observed up to $500\ \mu$W laser power on the free-standing sample. Nevertheless, in order to eliminate temperature-induced effects by the laser, the power was kept below $200\,\mu$W throughout the entire study. The intensity of the $2D$ mode on the suspended bilayer graphene sample was 2.8 times weaker than that of the supported sample in close agreement with the calculated enhancement factors of 100 nm SiO_2 around 2.75 [148]. This can be interpreted as clear evidence for free-standing graphene.

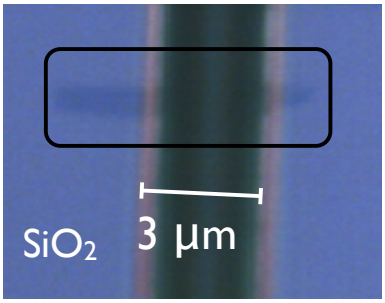

Figure 5.1: Optical image of exfoliated bilayer graphene over a $25\,\mu$m deep and $3\,\mu$m wide trench. The bilayer graphene is highlighted in the black frame. The supported bilayer graphene can be clearly identified due to optical contrast, while the suspended region does not show this contrast.

5.1.2 Theoretical analysis

Electronic structure and phonon dispersion

The electronic structure of single and bilayer graphene was calculated with the *ab initio* QUANTUM-ESPRESSO code [55]. The code is based on a plane-wave basis set, RRKJ pseudopotentials [149] and the generalized gradient approximation in the Perdew, Burke and Ernzerhof parametrization for the exchange-correlation functional [150]. The integration over the Brillouin zone was performed on a $42 \times 42 \times 1$ sampling grid. A Methfessel-Paxton broadening with a width of 0.02 Ry was used to occupy the electronic eigenstates [151]. Valence electrons were expanded in a plane wave basis with an energy cutoff at 60 Ry. For the geometry of the bilayer graphene, the experimental values of graphite were used, *i.e.*, a lattice constant of $a = 2.463\,\text{Å}$ and an interlayer distance $c/2 = 3.356\,\text{Å}$ [152]. In general, the calculated electronic energies are underestimated. This results from an underestimation of the fundamental bandgap, known in semiconductors as a result of a discontinuity in the exchange correlation functional [153]. This was accounted for by scaling the optical transition at the M-point to 4.7 eV as measured by optical conductivity and optical transmission spectroscopy [154, 155]. The phonon dispersion, which is used throughout the entire study, was obtained by fitting the experimental data from inelastic X-ray measurements in graphite [91, 152]. In this fit, the frequency of the K-point phonon with A_1 symmetry is in agreement with GW calculations of Ref. [156]. Figure 5.2 shows the comparison of our fit to recent data of Grüneis *et al.* [157]. The correlation of the two TO phonon dispersions is very good.

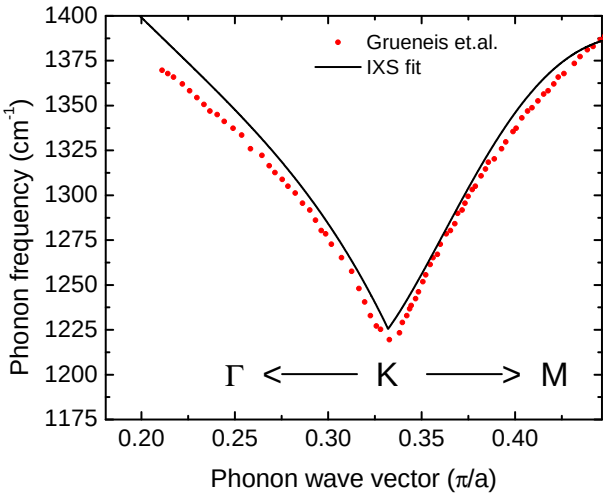

Figure 5.2: Phonon dispersion of Graphite. Black solid line is obtained by fitting the experimental data from inelastic X-ray measurements in graphite [91, 152] and red points are extracted experimental data from Ref. [157].

Notation of inner and outer processes in one dimension

In this chapter the question of $inner$ and $outer$ processes is applied to graphene and bilayer graphene. For this the notation is introduced in Fig. 5.3. In most notations $inner$ ($outer$) processes refer to excitations of electrons between the K-point and the M-point (Γ-K) as depicted for the electronic energy cones in graphene in 5.3 (a) and (b). In a one-dimensional consideration the contributing phonons are uniquely defined along the high-symmetry direction whereby $inner$ ($outer$) processes reveal phonons with wave vectors between the Γ-K (K-M) direction, respectively. 5.3 (c) and (d) depict the scattering processes in the graphene lattice. For $outer$ processes, the electrons are scattered by a phonon with wave vector $q = \overline{KK'} + 2\Delta k$ and the scattering path is along the Γ-K-M-K'-Γ direction. $\overline{KK'}$ denotes the distance between the two inequivalent Dirac points.
For the determination of the phonon frequencies, the wave vector is translated to the Γ point and yields a phonon frequency between the K-point and the M-point. For $inner$ processes as illustrated in 5.3 (d), the electron is scattered by a phonon with wave vector $q = \overline{KK'} - 2\Delta k$ and yields a phonon frequency between the Γ-point and the K-point. Assuming round equienergy contours, which is valid for low excitation energies below 2 eV, these two scattering processes yield the same phonon frequency.
In bilayer graphene more scattering processes are available, including so-called symmetric and antisymmetric processes. Figure 5.4 (a) and (b) show the symmetric and antisymmetric processes, respectively, for the π_1 and π_1^* band. Antisymmetric processes refer to scattering into a different electronic sub-band (e.g. excitation into π_1^*, scattering into π_2^* and backscattering into π_1^*); for this process the abbreviation OP12 for $outer$ and IP12 for $inner$ processes is introduced. Symmetric processes refer to scattering into the same electronic band. The processes for π_2 and π_2^* can be obtained accordingly. Symmetric processes therefore involve electrons with the same symmetry, while antisymmetric processes involve electrons with different symmetry. For optical transitions in the visible, in this model four symmetric and four antisymmetric processes for bilayer graphene are obtained. The contributing phonons are also of different symmetry, *i.e.* symmetric and antisymmetric phonons with respect to inversion symmetry.

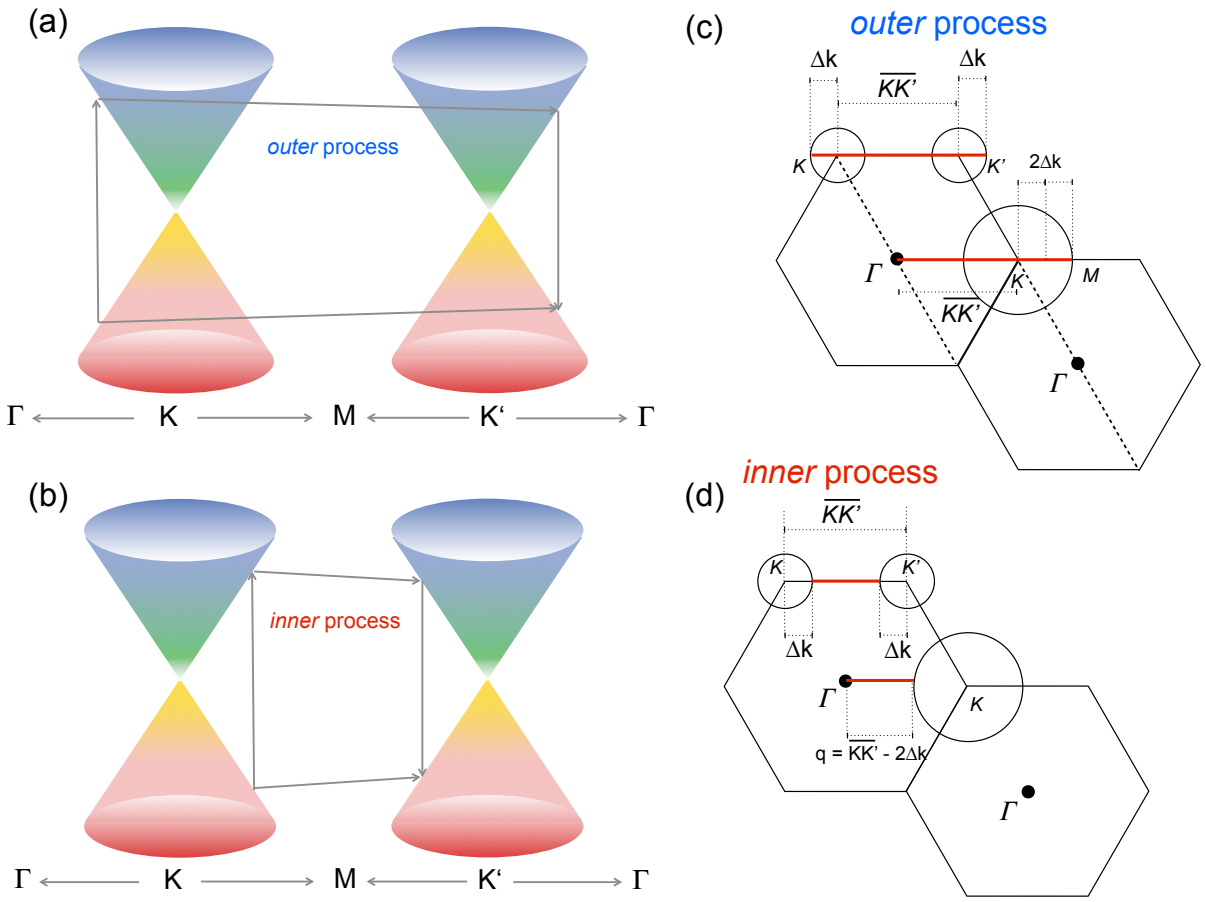

Figure 5.3: Notation of *inner* and *outer* scattering processes. (a) and (b) illustrate the one-dimensional *outer* scattering process. The scattering paths is along the Γ-K-M-K'-Γ direction and yields phonons between the K-M direction. (c) and (d) illustrate the one-dimensional *inner* scattering process. The scattering paths is along the K-M-K' direction yielding phonons between the Γ-K direction.

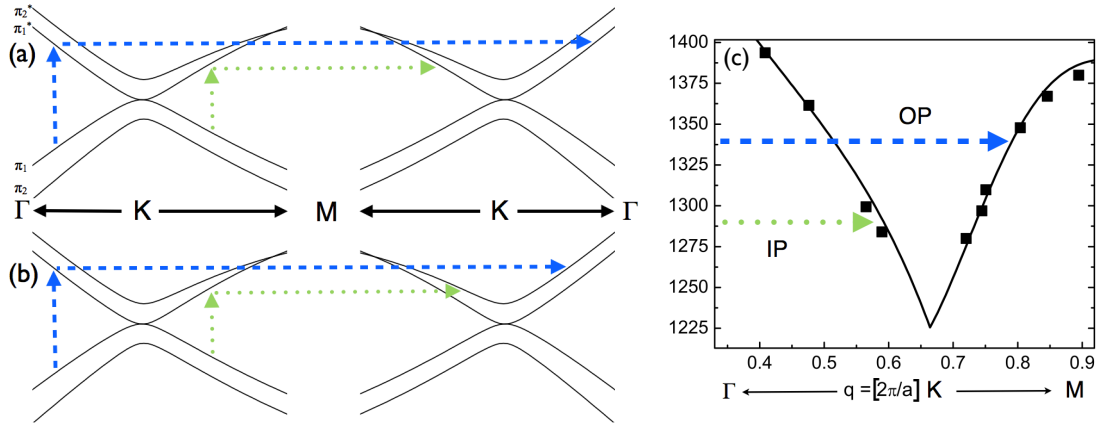

Figure 5.4: (a) Symmetric and (b) antisymmetric *inner* (green dotted arrow) and *outer* (blue dashed arrow) scattering mechanisms of the double resonance plotted in the electronic bandstructure of bilayer graphene along Γ - K - M for the π_1 valence band and the π_1^* conduction band. The processes for π_2 and π_2^* can be obtained accordingly. The backscattering and the recombination is omitted for clarity. (c) shows the contributing TO phonon branch along Γ - K - M. The squares are experimental IXS measurements from Ref [91, 152]. The solid line is the corresponding fit. The phonon wave vector corresponding to symmetric *inner* (IP) (green dotted arrow) and *outer* (OP) (blue dashed arrow) is shown.

Current discussion

A commonly easy method for a first determination of the phonon wave vectors is the so-called $q \sim 2k$ rule. This is a simplified approximation for fully symmetric bands involving the approximation of zero phonon energy $\hbar\omega(\mathbf{q}) \approx 0$. This approximation means that the double resonant phonon wave vector $\mathbf{q}$ is approximately twice the wave vector of the excited electron $\mathbf{k}$ at the resonant optical transition.

Within the $q \sim 2k$ approximation, the double-resonance is commonly reduced to one single scattering process [93, 145], well describing the narrow peak shape of the $2D$ mode in single-layer graphene compared to bilayer graphene. Usually, this approximation included only the *outer* process, based on the strength of electron-phonon-coupling [56] and an argument concerning the density of states in the two-dimensional Brillouin zone [94]. The calculations of Ref. 94 presented the first *two-dimensional* calculation of the double resonant D mode in carbon nanotubes, based on zone folding from graphene.

In contrast to Ref. 94, when performing a full integration of all possible scattering processes along the high-symmetry directions in the graphene Brillouin zone, contributions from both sides of the K-point (*inner* and *outer* processes) appear naturally [85]. Their frequencies though may be very close, depending on excitation energy. Recent calculations [87] and experiments [35, 36, 158] on uniaxially strained graphene revealed that indeed the restriction to only *outer* processes are not able to explain the

large strain-induced splitting of the $2D$ mode, nor its polarization dependence. Instead, phonons with wave vector between Γ-K ($inner$ process) must be involved. Very recently, calculations were reported including the entire two-dimensional Brillouin zone of graphene and the wave vector dependence of the matrix elements [88, 90]. In Refs. 89 and 90, the terms $inner$ and $outer$ are revoked as it is shown that the contributing phonons have wave vectors not just along the high-symmetry lines but are highly anisotropic. The frequencies of the contributing phonons, however, are very similar, giving a single $2D$ mode in single-layer graphene [90]. Reference 88, in contrast, states that the main contributions still come from the high-symmetry lines, with the largest intensity for the $inner$ processes. However, as shown in Ref. 85 and by strain calculation in Ref. 87, the differences in resulting frequencies between a one-dimensional and two-dimensional calculation are negligible.

5.1.3 The G mode and strain in free-standing bilayer graphene

Before analyzing the different scattering paths of the double-resonant process, the freestanding bilayer graphene is investigated in terms of defects and strain. The free-standing bilayer graphene and the G mode (E_{2g} symmetry) is shown in Fig. 5.5 (a) and (b), respectively, for the supported and the suspended sample. Spectra from the supported and suspended sample are indicated by the dashed and solid line, respectively. The G mode of the supported bilayer is broadened on the higher frequency shoulder compared to the one of the suspended sample. This broadened G mode might either consist of a single component or arise from a splitting of two contributions.

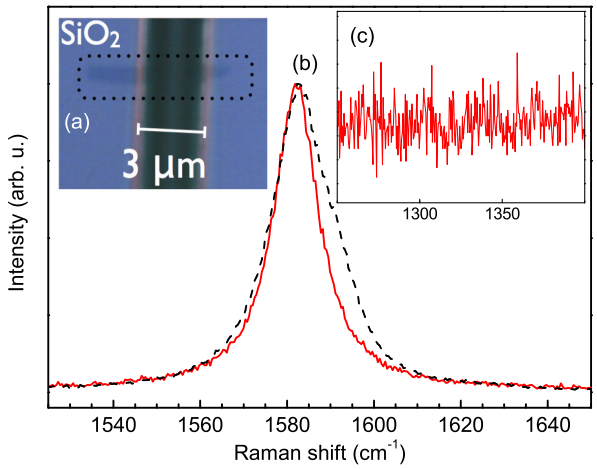

(a) Optical image of exfoliated bilayer graphene over a $25\,\mu$m deep and $3\,\mu$m wide trench. The bilayer graphene is highlighted in the black frame. The supported bilayer graphene can be clearly identified due to optical contrast. (b) Raman spectra of the G mode of the supported (black dashed line) and the suspended bilayer (red solid line). The intensities are normalized for better graphical presentation. (c) Raman spectrum of the free-standing bilayer in the D mode region.

Figure 5.5

Assuming a splitting of the G mode and comparing the frequencies and linewidths of the two components with results from gated bilayer measurements [159], the first component would arise from an undoped area at 1582.5 cm^{-1}, while the second component arises from a hole doped area at 1591.8 cm^{-1}. This might be due to differences in interaction between the two graphene layers with the substrate [160]. Second, uniaxial strain could be the reason for the splitting and would mean that the supported bilayer graphene is exposed to strain. However, this would further imply a red-shift of the G and $2D$ mode, which was not observed as outlined in the previous section [33, 161]. Also the G mode did not depend on the polarization direction of the incoming and outgoing light both in the supported and suspended bilayer sample [33]. In the alternative scenario, assuming a single contribution to the G mode, no change in frequency was observed but a broadening of the phonon linewidth. This can also be explained by slight doping and is in agreement with measurements from Ref. 159. The linewidth in bilayer graphene is more affected by doping than the frequency. This result would indicate that the suspended bilayer graphene exhibits a slight intrinsic electron doping. Another explanation might be the existence of additional decay channels of graphene phonons by the substrate resulting in a shorter lifetime and hence broadening of the G mode phonons. However, this is in contradiction to experiments in single layer graphene, where a broadening and shift of the G mode in the suspended region was observed [162]. Overall, the effect

of different substrates on the Raman process in graphene is not yet fully understood and requires further investigation. The inset (c) shows the frequency region where the disorder-induced D mode is expected for the suspended sample; the absence of the D mode indicates a nearly defect free sample.

Polarization dependent measurements of free-standing bilayer graphene

To demonstrate that the free-standing bilayer graphene is not subject to strain, polarization dependent Raman measurements are performed. A 100 x objective was used at 532 nm (2.33 eV) excitation energy. The spectral resolution was approximately $2\,\mathrm{cm}^{-1}$. A polarizer was used to control the angle of the incident light. An analyzer was placed before the grating and was fixed for light polarization parallel to the estimated strain direction. The power on the sample was below 0.5 mW in order to rule out temperature-induced shifts of the Raman peaks. A sketch of the geometry of the polarization measurements is shown in Fig. 5.6 (a).

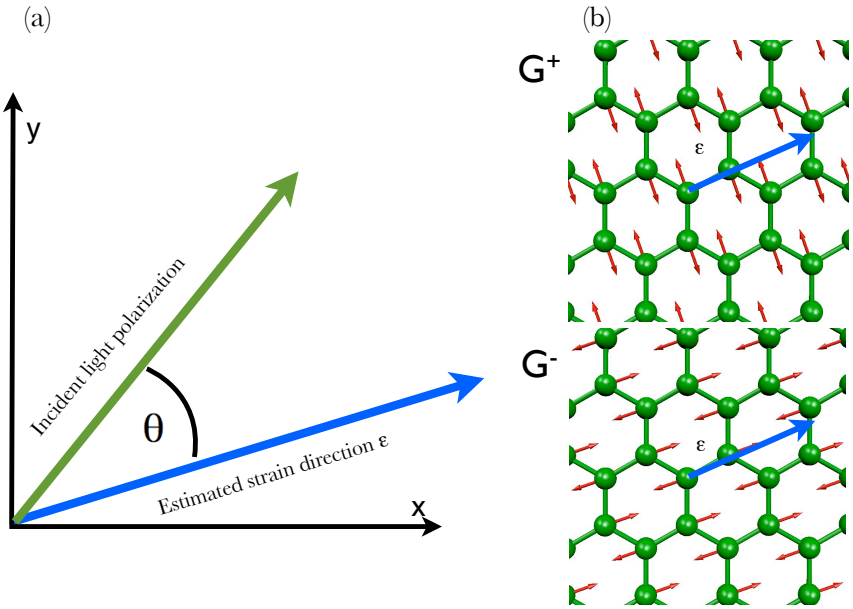

Figure 5.6: (a) Polarization geometry to determine potential strain. The estimated strain direction is chosen by the orientation of the sample. The analyzer was fixed and the incident light was rotated. In case of uniaxial strain, the G^- and G^+ modes can be resolved by rotating the polarization of incident light. (b) Eigenvectors of the degenerate G^- and G^+ modes. When strain is applied (indicated by the blue arrow) a frequency splitting between G^- and G^+ can be observed.

Fig. 5.6 (b) shows the vibration patterns of the graphene G mode. The (blue) arrow in Fig. 5.6 (a) and (b) indicates the estimated strain direction. The G mode has E_{2g} symmetry and is two-fold degenerate for unstrained graphene. The symmetry is reduced by applying uniaxial strain which in turn leads to a lifting of the degeneracy. Therefore the G mode splits into two peaks, so-called G^- and G^+ modes possessing eigenvectors parallel and perpendicular to the strain direction. As the incident light polarization is rotated, either the G^- or G^+ mode intensity is enhanced. This was shown experimentally in

Ref. [33] and theoretically confirmed in Ref. [161]. Figure 5.7 shows the polarization measurements of the G mode of the free-standing bilayer sample. No splitting of the G mode nor any changes in lineshape when rotating the incident light is observed. The intensity does not exhibit any changes in intensity. This is a consequence of the isotropy of graphene and an evidence for having an unstrained free-standing bilayer sample. Figure 5.8 shows the polarization dependence of the $2D$ mode. Again no changes in lineshape are observed. The Raman intensity achieves a minimum when the incident light and the scattered light detection are perpendicular to each other. The intensity of parallel polarization $I_{\parallel}$ with θ = 0° is less intense than than the intensity of crossed polarization $I_{\perp}$ at θ = 90°. A ratio $I_{\parallel}$ / $I_{\perp}$ = 2.95 is obtained. This polarization dependence reflects the inhomogeneous optical absorption and emission due to electron-phonon interactions [163].

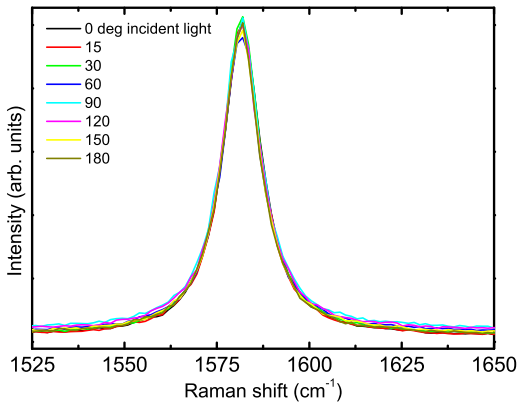

Figure 5.7: Polarization dependent measurements of the G mode with rotating incident light. Within our resolution no shifts or changes in lineshape are observed. The frequency of the G mode is at $1581.8\,\mathrm{cm}^{-1}$ and the FWHM is $12.6\,\mathrm{cm}^{-1}$

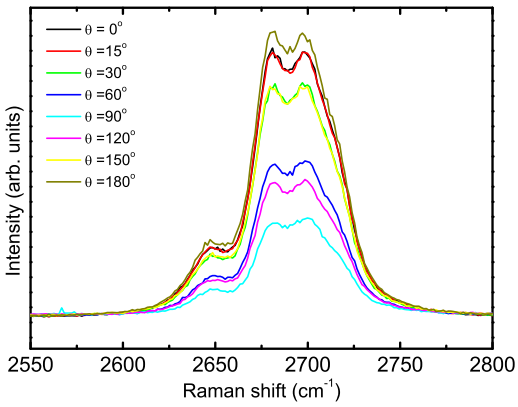

Figure 5.8: Polarization dependent measurements of the $2D$ mode. Within our resolution no shifts or changes in lineshape are observed. At θ = 90°, when the incident light is perpendicular to the detected light (crossed polarization) we observe a minimum in intensity.

5.2 Dominant scattering paths in bilayer graphene

5.2.1 The 2D mode in free-standing bilayer graphene

The electronic structure of bilayer graphene provides an excellent reference system for the investigation of scattering paths within the double-resonance. Figure 5.9 shows the $2D$ mode of the suspended bilayer graphene at 2.33 eV excitation energy. The $2D$ mode is due to a double-resonant process. As a consequence of the unique bandstructure, four distinct peaks are clearly visible and fitted by Lorentzians. The four peaks are numbered as shown from P_1 to P_4. Possible scattering processes of the four peaks are depicted in Tab. 5.1. Different combinations are considered including both symmetric / antisymmetric *inner* and *outer* processes. In the following, the different scenarios are analyzed and the dispersion with excitation energy and the relative strength in intensity are studied.

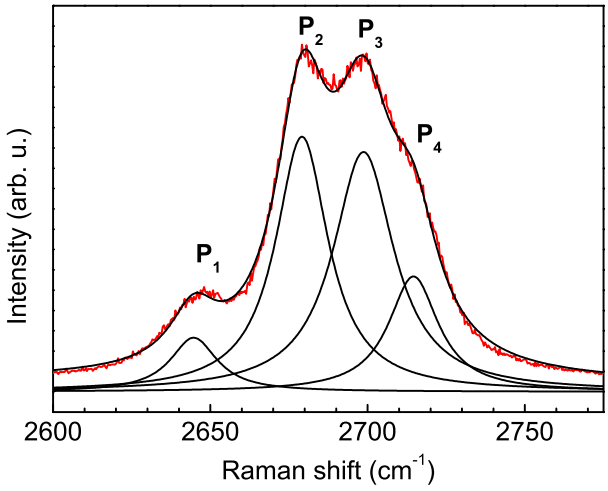

Figure 5.9

Raman spectrum of the $2D$ mode of suspended bilayer graphene with Lorentzian fits at 2.33 eV. The Lorentzian fits are numbered from P_1 to P_4.

Table 5.1: Four scenarios of *inner* and *outer* symmetric (S) and antisymmetric (AS) processes contributing to the $2D$ mode at excitation energy 2.33 eV.

experimental	P_1	P_2	P_3	P_4
(a) inner and outer S	OP22	IP22	IP11	OP11
(b) outer S and AS	OP22	OP21	OP12	OP11
(c) inner S and AS	IP22	IP21	IP12	IP11
(d) inner and outer AS	OP21	IP21	OP12	IP12

The $2D$ mode from 1.96 to 2.81 eV excitation energy for the suspended and the supported bilayer graphene is depicted in Fig. 5.10. In contrast to the suspended part, the four peaks in the supported part are broadened and partly merge into each other. The FWHM of the four peaks in the suspended bilayer ranges from 19 cm^{-1} to 23 cm^{-1} and is smaller than in the supported part, where it ranges from 25 cm^{-1} to 30 cm^{-1}. Similar behavior of the $2D$ FWHM was also observed by Berciaud *et al.* [162]

for a single suspended monolayer of graphene. Based on the clearly visible four peaks of the $2D$ mode in the suspended bilayer, the following part will show that the different contributions to the $2D$ mode can very well be assigned to contributions from different sides of the K-point. In the further analysis the focus is applied to the four peaks of the suspended bilayer graphene and the discussion will address both the dispersive behavior and the Raman intensity of the different contributions. In order to understand the physical origin of the four peaks (P_1,P_2,P_3 and P_4), the $2D$ mode Raman frequencies are calculated including $inner$ and $outer$ processes in combination with symmetric and antisymmetric processes.

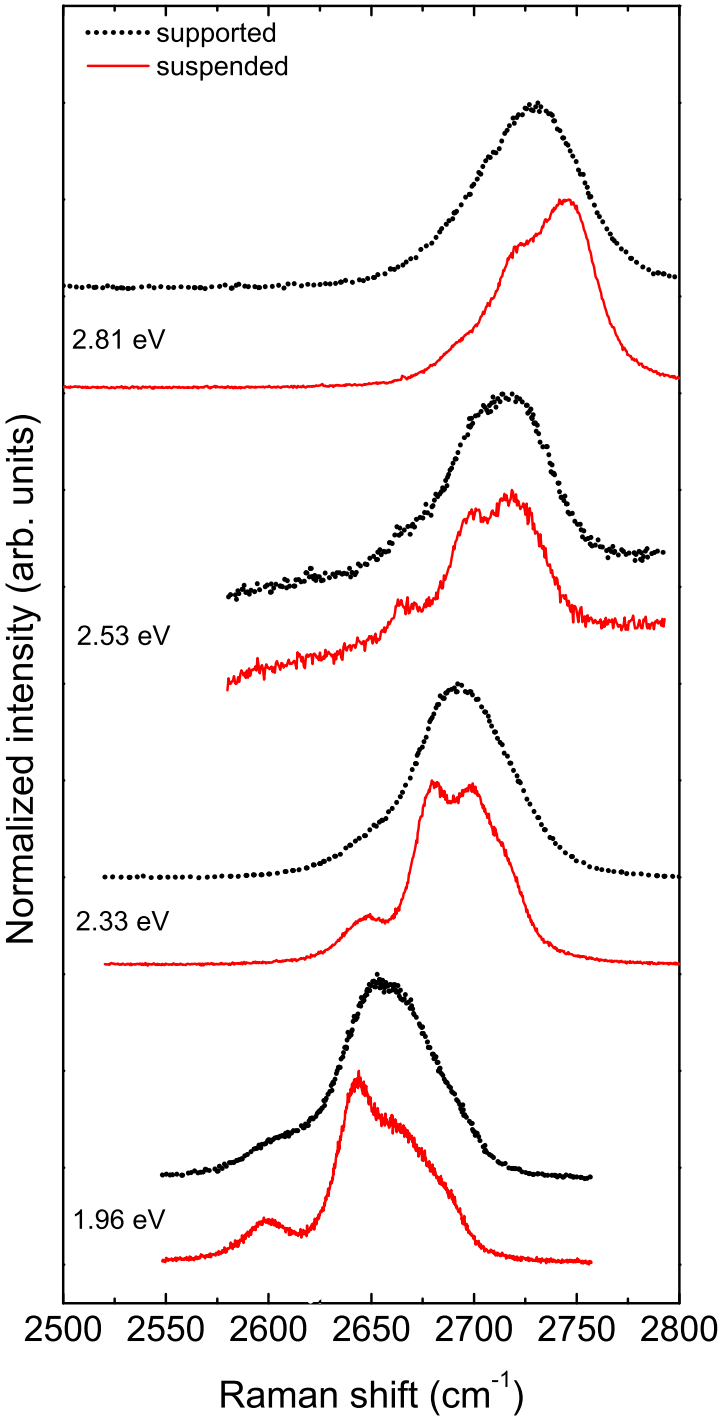

Figure 5.10: Raman spectra of the $2D$ mode for supported and suspended bilayer graphene at different excitation energies. The spectra are normalized to 1 and offset for clarity. One can clearly see the difference between supported and suspended bilayer graphene, since the four components of the lineshape of the suspended graphene are more distinct.

5.2.2 Simulation of the double-resonant Raman process in bilayer graphene

In order to acquire a more quantitative picture of both the different processes and Raman intensities in bilayer graphene, a one-dimensional integration of the Raman cross section along the high-symmetry line Γ-K-M is performed. The one-dimensional integration reveals insights to the contributing processes and phonon frequencies. The Raman cross section is proportional to $|K_{2f,10}|^2$, where the higher order matrix element $|K_{2f,10}|$ is defined as follows:

$$K_{2f,10} = \sum_k \frac{\mathcal{M}}{(E_l - E_{c_\mathbf{k}} + E_{v_\mathbf{k}} - i\gamma)(E_l - \hbar\omega_{\mathbf{qc}} - E_{c_{\mathbf{k+q}}} + E_{v_\mathbf{k}} - i\gamma)(E_l - \hbar\omega_{\mathbf{qc}} - \hbar\omega_{\mathbf{qv}} - E_{c_{\mathbf{k+q}}} + E_{v_{\mathbf{k+q}}} - i\gamma)}$$
$$= \sum_{a,b,c} \frac{M_{cf} M_{bc} M_{ab} M_{ia}}{(E_l - E_a - i\gamma)(E_l - \hbar\omega_\mathbf{q} - E_b - i\gamma)(E_l - 2\hbar\omega_\mathbf{q} - E_c - i\gamma)}. \tag{5.1}$$

The numerator consists of four matrix elements (summarized as $\mathcal{M}$ in the first expression), whereby in the second expression the notation M_{xy} indicates the matrix element for the scattering of the intermediate states x and y. M_{ai} is the matrix element, which describes the absorption of light, M_{ab} and M_{bc} are the scattering of electrons and holes mediated by phonons. M_{cf} is the matrix element for the recombination of the excited carriers and corresponds to the emission. The second line of Eq. 5.1 is a simplified expression of the first line. The first line corresponds to electron and hole scattering, while in the second line the intermediate steps can be interchanged. E_l is the energy of the incoming light. In consequence, the incoming and outgoing photon is expressed in E_l and E_l - $2\hbar\,\omega$, respectively. The electron and phonon wave vectors are expressed by **k** and **q**, respectively. The first term in the denominator articulates the initial state at wave vector **k** with energy $E_{c\mathbf{k}} + E_{v\mathbf{k}} = E_a$, where the indices c and v represents the conduction and valence band. The second term describes the scattering of the electron in the conduction band, which is scattered with a phonon with energy $\hbar\omega$ and wave vector **q** to a state with wave vector **k + q** and energy $E_{c\mathbf{k+q}} + E_{v\mathbf{k}} = E_b$. The last term represents the scattering of the hole to the state with wave vector **k + q** and energy $E_{c\mathbf{k+q}} + E_{v\mathbf{k+q}} = E_c$. The broadening parameter γ was set to $40\,\mathrm{meV}$; the matrix elements are taken as constant. The incident photon energies were set to the experimental energies. Scattering of those phonons is enhanced which satisfy the double-resonant condition. This is the case if the denominator of Eq. 5.1 vanishes and is obtained for those combinations of phonon wave vector **q** and phonon energy $\hbar\omega(\mathbf{q})$ that satisfy the double-resonance.

The evaluation of $|K_{2f,10}|$ takes into account symmetric $inner$ and $outer$ processes and includes both the electronic and phonon density of states. The sum is performed in one dimension along the high symmetry direction over all possible **k** points. The Raman intensity is obtained as follows:

$$I_{\mathrm{Raman}} = \left| K_{2f,10} \right|^2. \tag{5.2}$$

This calculation of the Raman intensity simulates the Raman frequency and the intensity of the different

contributions.

Wave vector dependence

The wave vector dependence is studied and permits to visualize and assign the origin of the contributing processes along the high-symmetry direction. The calculated contributions of both $inner$ and $outer$ processes are depicted in Fig. 5.11 as function of the phonon wave vector $\mathbf{q}$. In (a) the TO phonon branch is illustrated, (b) and (c) show the phonon contributions of $inner$ and $outer$ processes, respectively, for different excitation energies. Each calculation of symmetric and antisymmetric processes shows four different peaks in different directions of the Brillouin zone. The solid line indicates the calculation of symmetric processes, the dashed lines represent antisymmetric processes. The phonon contributions can be directly assigned in the phonon dispersion of the TO phonon branch. The intensities arise from exclusively electronic density of states in one dimension. Though not the entire Brillouin zone was integrated, the relative intensities are comparable to calculations of a two-dimensional integration including all matrix elements with stronger intensities for $inner$ processes [88]. As mentioned in Ref. [88] the electron-hole broadening increases towards higher excitation energies, which in fact lowers the absolute intensity. Here, this behavior can be neglected since the relative strengths of the four contributions at a given excitation energy are considered. Figure 5.11 (c) also implies that a combination of only $outer$ processes, *i.e.* symmetric and antisymmetric is not able to reproduce the measured intensities, since one would observe two dominant peaks at the exterior of the $2D$ mode, *i.e.* the lowest (P_1) and highest peak (P_4) frequency and hence there would be a dip in the $2D$ mode of bilayer graphene.

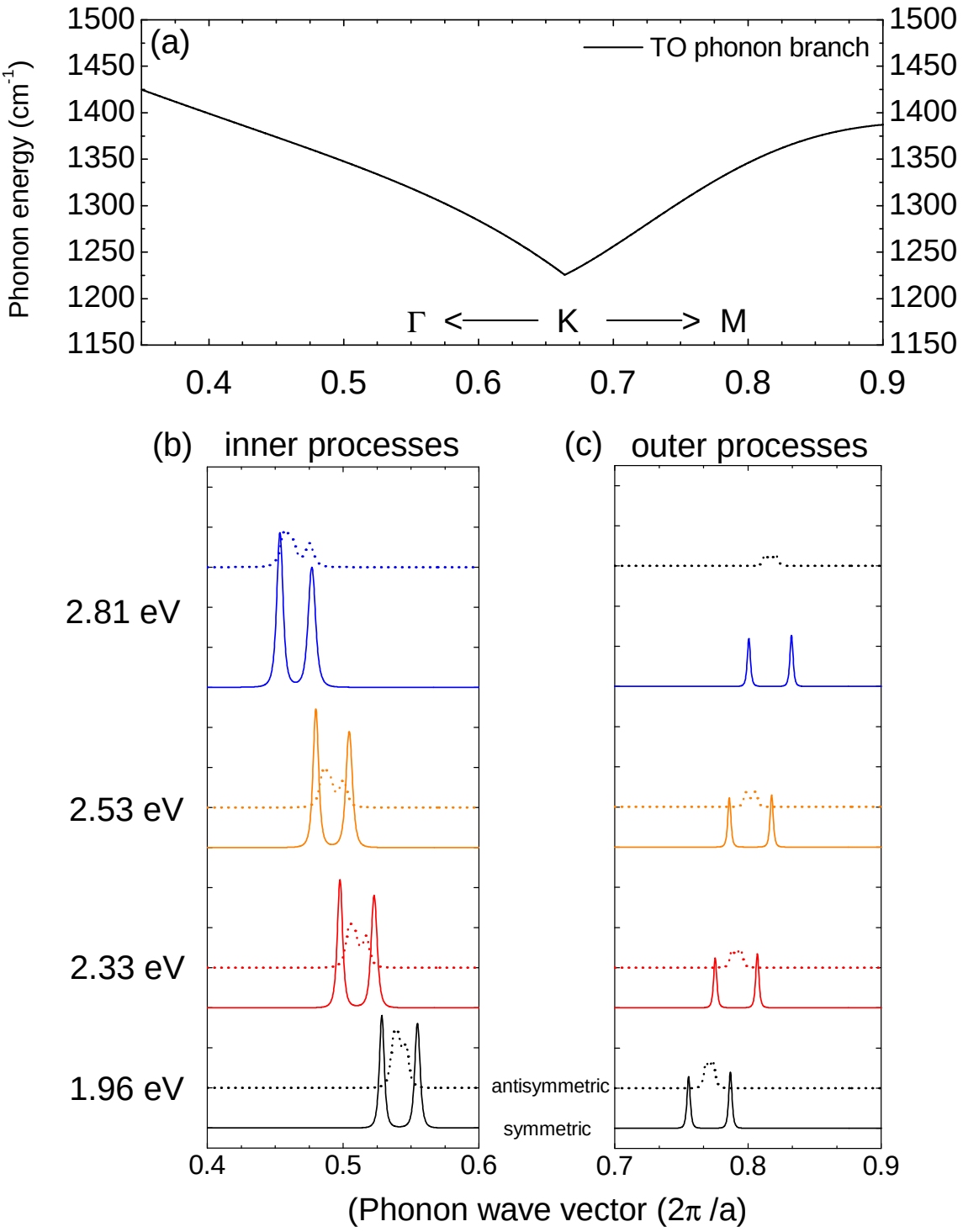

Figure 5.11: (a) shows the transverse optical (TO) phonon branch in the Γ-K-M direction. (b) and (c) shows the contributing phonon wave vectors of *inner* and *outer* processes for different excitation energies. The lower solid spectra of each excitation energy denotes symmetric processes, the upper dashed spectra denotes antisymmetric processes. Intensities are unscaled and can directly be compared.

Evolution with excitation energy

The dispersion with excitation energy is considered in this subsection. Fig. 5.12 shows a comparison of the experimentally obtained Raman frequencies (black plus signs) and calculated frequencies of four different scenarios. Each graph in Fig. 5.12 (a) - (d) depicts one of the four scenarios summarized in Tab. 5.1 and denoted as follows:

- (a) Symmetric *inner* and *outer* processes
- (b) Symmetric and antisymmetric *outer* processes
- (c) Symmetric and antisymmetric *inner* processes
- (d) Antisymmetric *inner* and *outer* processes

Each of the processes follow a smooth curve as a function of the excitation energy. The scenario, which is depicted in Fig. 5.12 (a) is in close agreement with the experimentally obtained data. Scenario (b) shows good agreement with slight deviations at higher excitation energies. A scenario considering exclusively $inner$ or antisymmetric processes as shown in (c) and (d) shows large deviations to the experimental data, since the phonon frequencies are in a very narrow range. In Fig. 5.12 (d) one would even observe a single peak at low excitation energy, which is in contrast to the experimental data. Therefore scenario (a) is favored, since scenario (b) yields wrong intensities as was shown in Fig. 5.11. The only strong deviation is the low frequency contribution. The low frequency contribution, *i.e.* P_1, can be reproduced very well above $2.33\,\mathrm{eV}$ but the deviation gets larger at lower excitation energies. In Ref. [164] the softening of the first peak was attributed to the Kohn-anomaly at the K-point [56]. The softening of the TO phonon branch near the K-point is however included in the calculation according GW calculations of Ref. [156] and in agreement with recent inelastic x-ray measurements [157]. This effect is therefore not caused by an uncertainty in the calculation.
One should note that within the model the estimated frequencies match the experimental data very well without any rescaling.

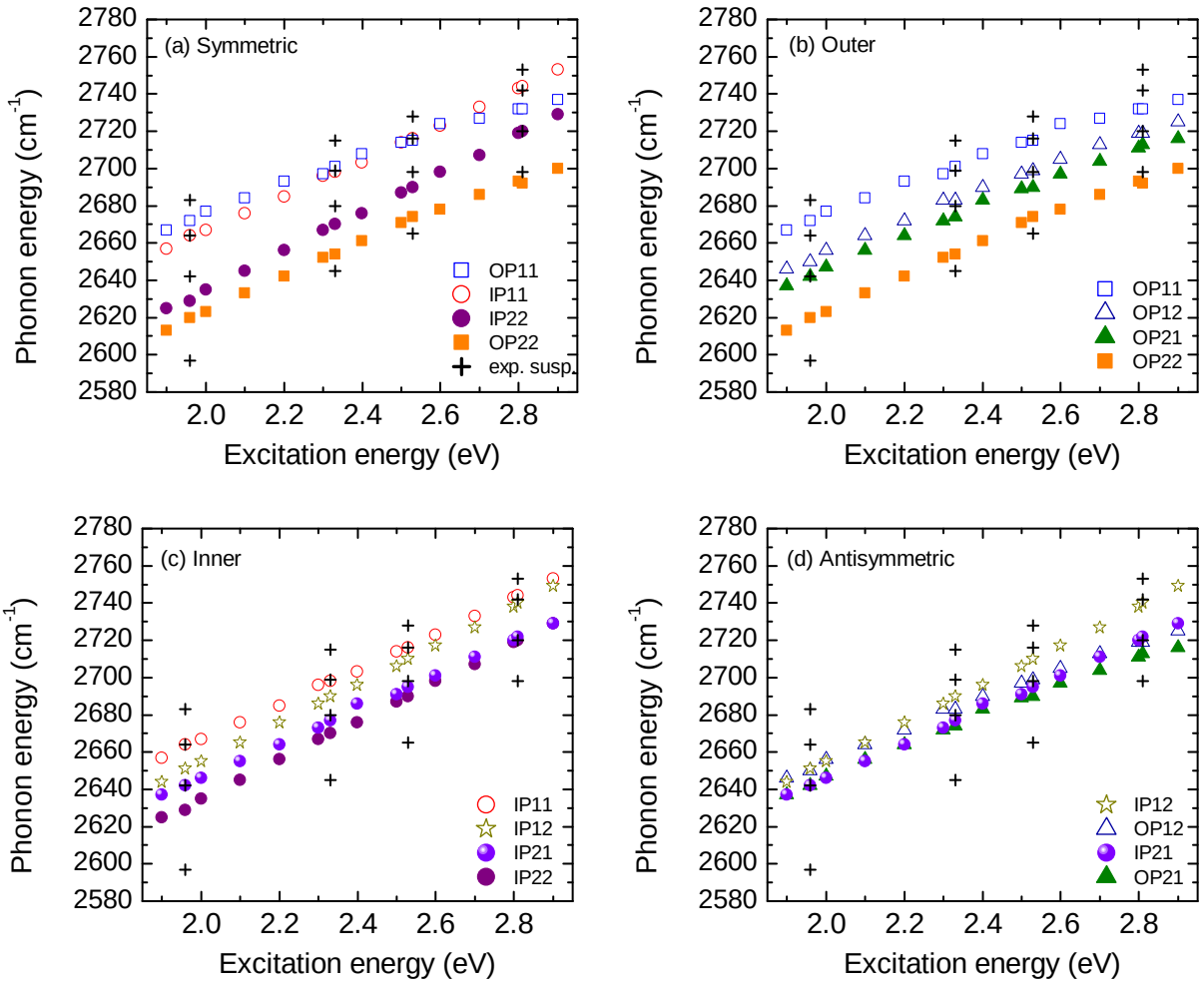

Figure 5.12: Calculated shifts of different scattering scenarios and experimental obtained shifts of the $2D$ mode. Symmetric *inner* and *outer* processes are shown in (a). Exclusively *outer* and *inner* processes are depicted in (b) and (c), respectively. Antisymmetric *inner* and *outer* processes are shown in (d). The experimental data points are represented as black plus signs.

Raman spectra

The relative strength of the $2D$ mode intensity is discussed. The calculated Raman spectra is shown in Fig. 5.13. In contrast to Fig. 5.11 which only included the electronic density of states, here also the phonon density of states is included in the calculation. Further in order to obtain a spectrum, the contributions are broadened by a Lorentzian profile with a linewidth of $15\ \mathrm{cm}^{-1}$. This is below the experimental value, but allows the determination of the different contributions.

The experimental spectra are characterized by four distinct peaks with two main contributions, which change the relative strength when progressing towards higher excitation energies. The first peak possesses a varying spacing to the main contributions. The last peak merges into the third peak towards higher excitation energies.

The overall agreement of the calculated Raman spectra with the experimental data is excellent. The lineshape and relative intensities are very well reproduced. The two main contributions (P_2 and P_3) are very well reproduced both in intensity and the absolute Raman frequency and stem from $inner$ processes. P_1 and P_4 are due to $outer$ processes.

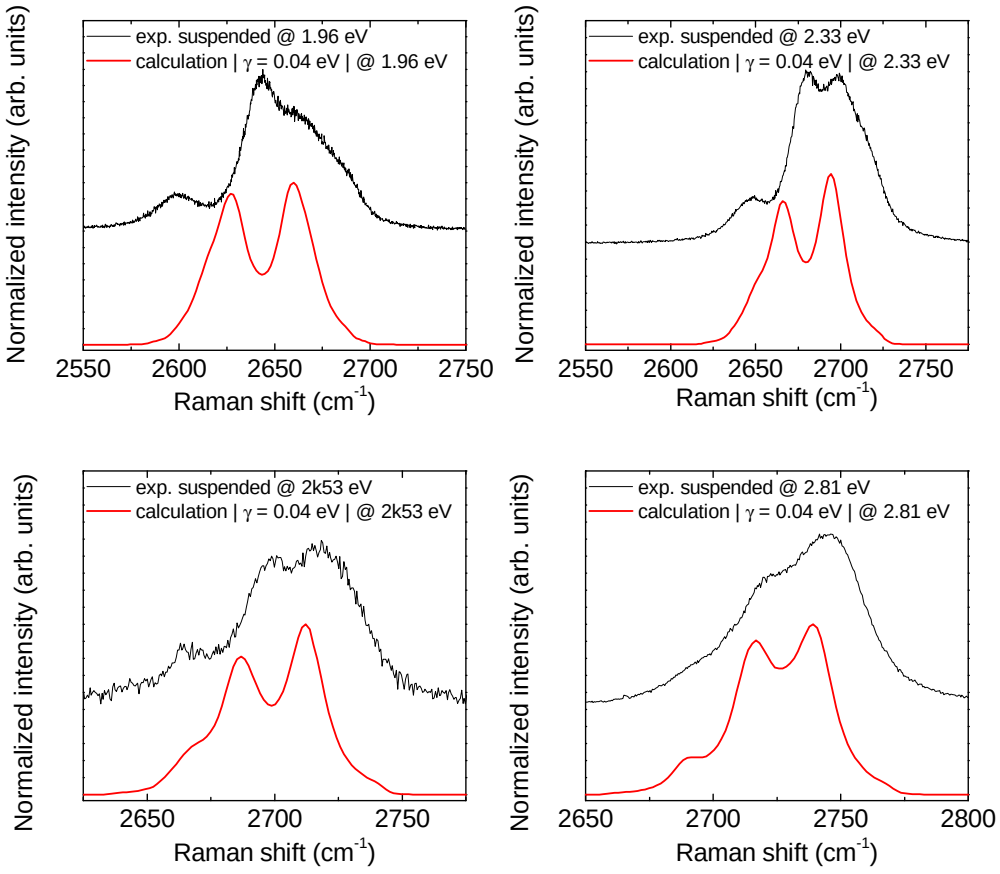

Figure 5.13: Raman spectra of the $2D$ mode of suspended bilayer graphene at different excitation energies compared to the one-dimensional calculation. The spectra are normalized to 1 and offset for clarity. The lineshape and intensities are very well approximated by this calculation.

5.2.3 Relative strength of the Raman intensity

The measurements of free-standing graphene and the theoretical analysis showed strong evidence that a combination of symmetric $inner$ and $outer$ processes can reproduce both the Raman frequencies and intensities, whereas $inner$ processes give rise to the dominant peaks in the Raman spectra. As can be seen in the measured Raman spectra, the two main contributions (*i.e.* P_2 and P_3) change their relative intensities slightly when progressing to higher excitation energies. This behavior is reflected in Fig. 5.11 (b) for the symmetric processes, which included the evolution of the electronic density of states. The contribution with smaller wave vector (*i.e.* P_3) has a similar intensity at low excitation energies and increases for higher excitation energies. This is reflected in the electronic density of states, since the π_2^* band exhibits a less pronounced slope after the crossover with the π_1^* bands. This results in a higher density of states and provides a higher contribution in the calculation. The one-dimensional calculations neglected a few important contributions such as the scattering rate, electron-phonon coupling and the optical matrix element. This is discussed below.

Scattering rates

The intensity of the $2D$ mode is dependent on the scattering rates and has been shown to obey the following equation [88, 165]:

$$I(2D) = c\left(\frac{\gamma_K}{\gamma_{tot}}\right)^2 = c\left(\frac{\gamma_K}{\gamma_{ep}+\gamma_{ee}+\gamma_{ed}}\right)^2 \tag{5.3}$$

In this equation the constant is denoted as c. The phonon emission rate is given by γ_K and the electronic scattering processes are summarized in γ_{tot} and consist of the electron-phonon scattering rate γ_{ep}, electron-electron scattering rate γ_{ee} and the electron-defect scattering rate γ_{ed}. The electron-phonon scattering rate is the dominant factor in this equation and only dependent on the excitation energy E_l [88, 166]. Since only the relative strengths within an excitation energy are compared, the scattering rates can be neglected. In the following the electron-phonon coupling and the optical matrix elements are discussed since they directly enter the Raman cross section.

Contribution of the electron-phonon coupling

One may argue that the electron-phonon coupling change the relative strength of the particular contributions, since there is a strong angular dependence [164]. However, in a one-dimensional integration there is no such angular dependence. It has been shown that in addition to the angular dependence a **k** dependence of the electron-phonon coupling is present. Piscanec *et al.* [56] showed that the strength of the electron-phonon coupling can be approximated from the measured dispersion of the D mode in excellent agreement to calculations. Further only the relative intensities at a given excitation energy are compared yielding quite similar **k** values. Since the dispersion is straight linear for our favored processes, taking the electron-phonon matrix elements as constant provide a very good approximation.

Contribution of the optical matrix element

Here the contribution of the optical matrix element is discussed.* The calculation of the matrix element is based on an analytically evaluation using the tight-binding description [167]. The carrier-light interaction is determined by density of the states and the optical matrix element [167, 168]. The matrix element can be analytically evaluated for bilayer graphene using tight-binding wave functions which are linear combinations of the atomic orbital functions.

The matrix element describes the direct optical transitions between the valence π_1 and π_2 and the conduction band π_1^* and π_2^*, since the momentum of photons is negligibly small. The coupling strength is the same for the transitions $\pi_1 \rightarrow \pi_1^*$ and $\pi_2 \rightarrow \pi_2^*$ in the bilayer graphene.

Figure 5.14 (a) illustrates the square of the optical matrix element as a function of k_x and k_y along the entire Brillouin zone. A highly anisotropic coupling with maximum values at the M-points is observed. Plotting $|M^{vc}(\mathbf{k})|^2$ along the high-symmetry line Γ-K-M, the carrier-light coupling is found to be stronger on the K-M than on the K-Γ side, as shown in Fig. 5.14 (b). Furthermore, in contrast to graphene, the matrix element goes to zero around the K and K'-points in bilayer graphene. Finally, in Fig. 5.14 (c), the angle dependence of the optical matrix element around the K'-point is shown in a distance of $k = 2$ nm^{-1}. It has a maximum at the K-M side corresponding to the angles $0°, 120°$, and $240°$ and a minimum at the K-Γ side ($60°, 180°$, and $300°$). This consideration of the matrix element further supports the idea of dominant $inner$ processes in the one-dimensional approach.

*Calculations of the optical matrix element were performed and provided by E. Malic (TU Berlin)

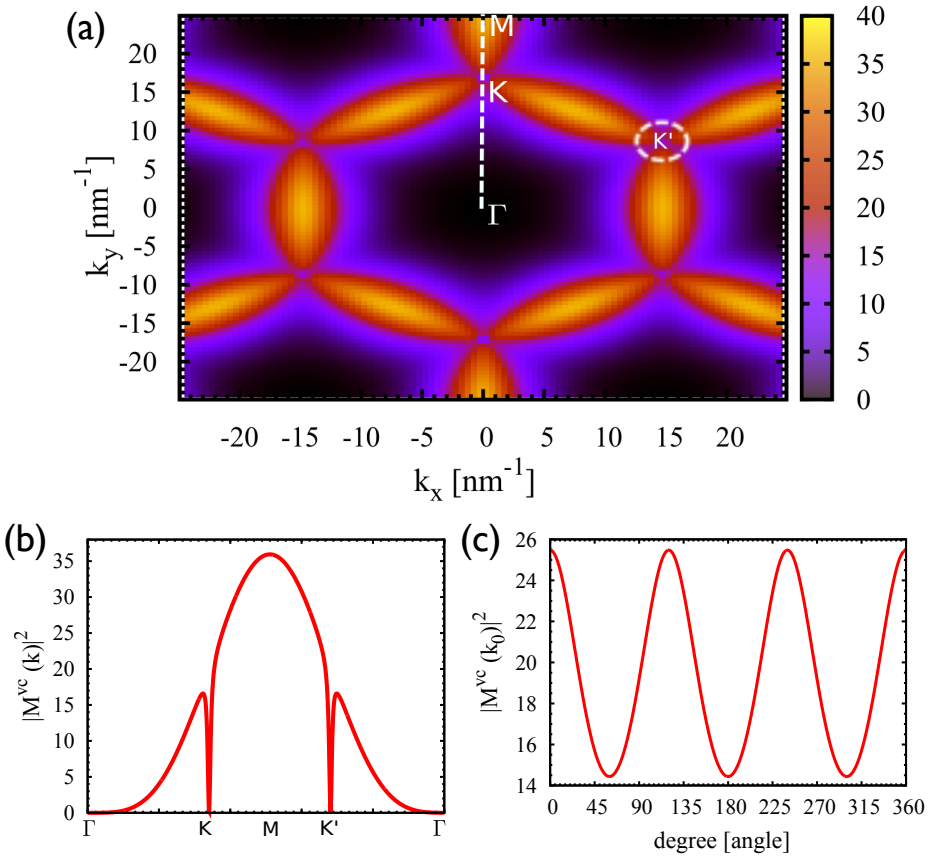

Figure 5.14: (a) The contour plot of the square of the optical matrix element $|M^{vc}_{k_x,k_y}|^2$ for bilayer graphene along k_x and k_y directions illustrating that the carrier-field coupling is highly anisotropic with maxima at the M-points of the Brillouin zone. (b) The matrix element along the high-symmetry line Γ-K-M (cp. the dashed line in the contour plot above) suggesting that the carrier-light coupling will be stronger on the K-M than on the K-Γ side. (c) Angular dependence of the optical matrix element around the K'-point (with $k_0 = 2$ nm^{-1}), cp. the dashed circle in the contour plot. Here, angle $0°$ corresponds to the K-M- and $180°$ to the K-Γ-direction. All values are in eV^2.

5.2.4 Summary and outlook towards a two-dimensional calculation

Here, a summary of the double-resonant process in bilayer graphene is provided. Further, the terms of $inner$ and $outer$ processes and a comparison between an one-dimensional and a two-dimensional calculation is discussed. The one-dimensional analysis showed that the $2D$ mode in bilayer graphene exhibits contributions of both $inner$ and $outer$ processes, *i.e.* phonon contributions from parts of the Brillouin zone on both sides of the K-point. The combination of $inner$ and $outer$ processes can qualitatively explain the relative strength of the Raman intensity of the $2D$ mode contributions. The results have also impact on the analysis of the lineshape of the $2D$ mode in single-layer graphene, since it means that $inner$ and $outer$ processes can be resolved in experiment by tuning the excitation energy. This is due to a different change in the phonon wave vector $\mathbf{q}$ between $inner$ and $outer$ processes when approaching the M-point, *i.e.* excitations towards the UV.
However, only in one-dimension the terms of $inner$ and $outer$ processes are uniquely determined and different expressions are used simultaneously;
for $inner$ processes:

- electrons between the K and M direction
- phonons between the Γ and K direction,

for $outer$ processes:

- electrons between the Γ and K direction
- phonons between the K and M direction

Next, the validity of these different expressions is discussed in terms of a two-dimensional consideration of scattering paths and contributing phonon wave vectors.

When performing a two-dimensional calculation the electronic scattering paths do not lie along the high-symmetry lines for *outer* processes as shown in Fig. 5.15 in the electronic contour plot of graphene [89]. Seemingly *outer* scattering paths possess an offset and the excitation takes place rotated by a certain angle. This is due to the enhanced optical matrix element between the M-point and the K-point as outlined in the previous section.

The discussion about the intensity of the contributing processes and the optical matrix elements, which was conducted above, is in contrast to this scattering paths, since this scattering *outer* process yields the same optical matrix element as *inner* processes. This would result in equal contributions of *inner* and *outer* processes. However, the angular dependence of the electron-phonon coupling may also change this. When considering two-dimensional scattering paths it is at first sight not clear to distinguish between *inner* and *outer* processes as in the case of a one-dimensional consideration. In the two-dimensional calculation one could argue that the excitation of the former *outer* process is now between the K-M direction yielding an *inner* process. On the other hand, the electron scatters across the K- and M-point, which yields a so-called *outer* process as depicted in Fig. 5.15.

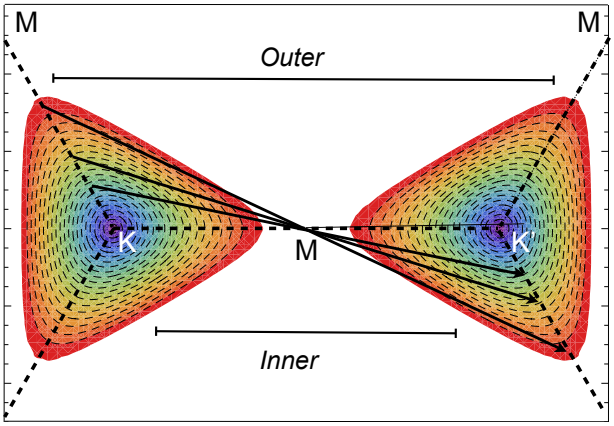

Figure 5.15: Electronic energy contour of single-layer graphene and scattering paths in two-dimensions according the dominant transitions between the K-M direction. The one-dimensional scattering path is omitted for better graphical representation.

It can be shown by simple geometric considerations that the above mentioned seemingly *outer* process is equivalent to an *inner* process as discussed in the introductory part of this thesis. Further two limiting cases are considered. Figure 5.16 (a) and (b) depicts the *outer* scattering path in the limiting case of isotropic equienergy contours (no trigonal warping) and strongly anisotropic equienergy contours (strong trigonal warping). The first scattering path possesses a phonon wave vector of $\overline{KK'} + \Delta k$, while the second scattering path possesses a phonon wave vector of $\overline{KK'} + 2\Delta k_{Tr}$. These two scattering paths are different for isotropic energy contours and they are converging for the limiting case of strong triangularly shaped energy contours. These scattering paths might explain the nonlinear softening of the first peak

P_1, which could not be unraveled by the one-dimensional calculation.
5.16 (c) illustrates scattering paths between electronic states with strong optical matrix elements; i.e. scattering in two-dimensions. The scattering paths possess an offset and the excitation occurs where the optical matrix element is strongest, i.e. along the K-M direction and both the electron and phonon wave vectors do not lie along the high-symmetry line. The phonon wave vector is obtained by a translation of the electron wave vector. However, it can be shown that the scattering process as depicted by the red line in Fig. 5.16 is equal to an $inner$ scattering process as shown in Fig. 5.3. The corresponding phonon frequency has a distance of $2\Delta k$ from the K-point or $\overline{KK'} - 2\Delta k$ from the Γ-point, which already has been assigned to be an $inner$ process. This result even holds under strong trigonal warping effects of both the electronic and phonon structure, since in both cases the excitation is along the K-M direction yielding exactly the extent of the trigonal warping. This further supports the approximation of considering scattering paths in one-dimension.
To sum up the conclusion: The meaning of *inner* and *outer* processes should be extended to *different sides of the K point* in the Brillouin zone. Further it should take into account the scattering paths. Then the terms of $inner$ and $outer$ processes are uniquely defined in one-dimension.
Indeed, the one-dimensional approximation along the high-symmetry line as previously outlined give excellent agreement with experimental data. Further the intensity is in close agreement with a two-dimensional calculation of Ref. 88. In the next sections, the one-dimensional consideration of the double-resonant process is followed up.

(a) *Outer scattering* process

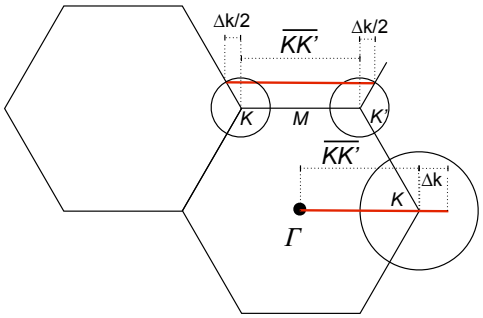

(b) *Outer scattering* process (trigonal warping)

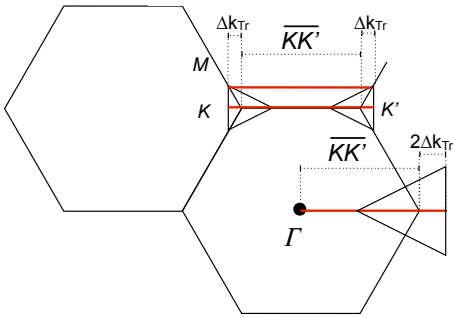

(c) *Two-dim. scattering* process

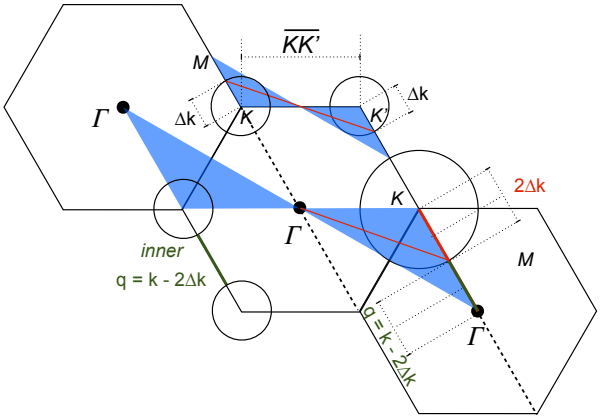

Figure 5.16: (a) shows an *outer* scattering process where the excitation takes place between the K-M direction, the electron is however scattered horizontally. (b) shows two *outer* scattering processes in the limiting case of strong trigonal warping. (c) Two-dimensional scattering process according the dominant directions of the optical matrix element along the K-M direction. The corresponding phonons stem from the high-symmetry line along the K-M direction. This process is equivalent to the *inner* process yielding exactly the same phonons independently of the extent of the trigonal warping.

5.3 Origin of the TO and LA combination mode in graphene

Theoretical descriptions of electron-phonon interactions underestimate the slope of the phonon dispersions. The inclusion of nonlocal-exchange-correlation effects within the GW approach produce good agreement with experimental phonon dispersions from inelastic X-ray scattering [56, 152, 156]. GW is a Green's function approach with screened electron-electron interactions, which is denoted as W. Inelastic X-ray scattering probes the phonon dispersion, but cannot be applied to graphene, few-layer graphene or carbon nanotubes.

Double-resonant Raman scattering, on the other hand, provides a powerful technique for probing the phonon dispersion of such nano systems. The transverse optical (TO) branch has been investigated in depth. However, other phonon branches can also be explored using the double-resonant process [84]. It is possible to combine different phonon branches in higher order Raman scattering, as in the case of the transverse optical (TO) and the longitudinal acoustic (LA) phonon, which is around ≈ 2450 cm^{-1}. Usually this mode is called G^* or (D+D") in literature. Since it is not clear from these expressions that the origin of the mode comes from different phonons it is called the TO + LA mode in the following. This combination mode has already been determined near the Dirac point by double-resonant Raman scattering for graphene and graphite [164]. The measured frequency of this mode and its dispersion can only be derived from a certain direction in the Brillouin zone reviving the discussion of dominant double-resonant processes and scattering paths. In present literature, the discussion about relevant scattering paths are usually initiated from the electronic structure [35, 36, 87, 88]. Below, the discussion is reversed and starts with the measured phonons and thus the phonon dispersion. Below it is shown that the TO + LA mode stems from the $inner$ processes, *i.e.* excitation in the electronic structure between the K-M direction. Further the scattering paths of the TO + LA mode are discussed by a careful lineshape analysis and it is shown that the main contribution comes from the high-symmetry lines. The evolution with the number of layers and with excitation energy is discussed in detail giving a comprehensive treatment of this combination mode.

5.3.1 Dispersion of the TO and LA mode

The $2D$ mode exhibits a dispersive behavior of around $100\,\mathrm{cm}^{-1}$/eV when progressing to higher excitation energies, whereas the shift of the TO and LA mode is negative and around $-25\,\mathrm{cm}^{-1}$/eV in the visible regime. This is a consequence of a negative slope of the longitudinal acoustic phonon branch, which provides the major impact on the development of the phonon dispersion. Figure 5.17 shows the measured Raman frequency of the TO + LA mode in different samples and the expected slope obtained from calculated phonon dispersions. Here, the sum of the two phonon branches is shown. The phonon wave vector is calculated from the double-resonant processes that satisfy the double-resonant condition in the bandstructure of graphene as already outlined in Chapter 5.2.2. An agreement of the measured and theoretically expected phonon frequencies can only be obtained, if the assigned phonon frequencies stem from the Γ - K direction. In Ref. [164] one TO phonon from the K-M direction and one LA phonon from the Γ - K directions were used for the assignment in the phonon dispersion. However, due to momentum conservation of the double-resonant process, a contribution of phonons from different sides of the K point is forbidden. From the assigned phonons it follows that electronic transitions are excited between the K and M direction. Hence, the origin of this peak arises from so-called *inner* processes.

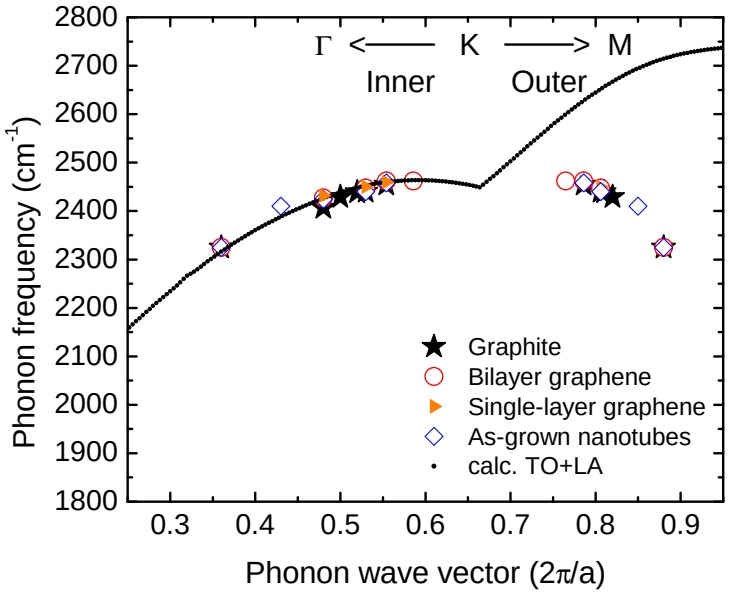

Figure 5.17: Calculation of the transverse optical (TO) and longitudinal acoustic (LA) as function of the phonon wave vector. Points are measured frequencies of different samples and assigned to the corresponding phonon wave vector of both *inner* and *outer* processes.

5.3.2 Lineshape analysis: Single-layer graphene

Here, the lineshape of the TO + LA mode is analyzed for single-layer graphene. The lineshape of the TO + LA mode exhibits one major contribution and an asymmetric tail towards higher frequencies as depicted in Fig. 5.18. In order to acquire a more quantitative picture of the asymmetry, a calculation including both the electronic and phonon density of states that satisfy the double-resonant condition at 2.33 eV is compared to the experimental spectrum. The calculation illustrates the graphene double-resonant density of states for the *inner* process wave vector along the K - M direction. A slight asymmetry towards higher frequencies is indicated, *i.e.* to higher excitation energies in the electronic structure or smaller phonon wave vectors. Both contribute to the asymmetric lineshape. The combined phonon density of states dominates over the electronic density-of states and is shown as a function of the wave vector in the inset along the Γ-K direction. This is due to the fact that at excitations in the visible range, the electronic bands still possess a linear dispersion relation.

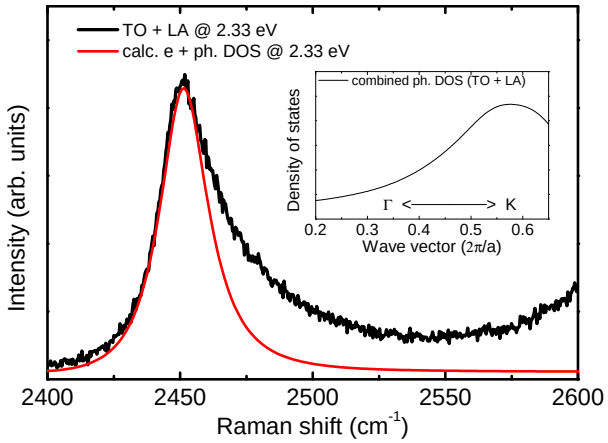

Figure 5.18: Raman spectrum of the TO + LA mode (black) and density of phonon and electronic states determined at 2.33 eV that satisfy the double-resonant condition in red. Inset shows the combined phonon density of states of the TO + LA phonon along Γ-K direction (*inner* process).

So far only scattering processes along the high-symmetry lines were considered. They give a very good approximation of both frequencies and relative intensities as outline in Chapter 5.2. However, the asymmetric tail is not reproduced by this one-dimensional consideration. In the last section it has been shown that also scattering processes are allowed for the entire Brillouin zone depending on the polarization direction. Thus two-dimensional scattering processes are analyzed in the following.

The two-dimensional scattering processes for both *inner* and *outer* processes are illustrated in Fig. 5.19. It should be noted that the rhombi indicate the area of the contributing phonons. For instance, the blue rhombi represent the contributing phonons for *inner* processes along the Γ-K direction. This implies an excitation between the K - M direction in the electronic dispersion. Since the TO + LA mode is due to an *inner* processes, only the blue rhombi have to be considered. It should be noted that after an angular segment of 120 ° the different processes are transferred into each other yielding three *inner* and three

outer scattering paths from the K point. In order to explain the asymmetry of the lineshape, the two dimensional electronic and phonon structure has to be considered. First a certain excitation energy is chosen and tracked in the electronic dispersion. This gives the angular segment of contributing electrons. The phonon dispersion will then be used for the determination of contributing frequencies.

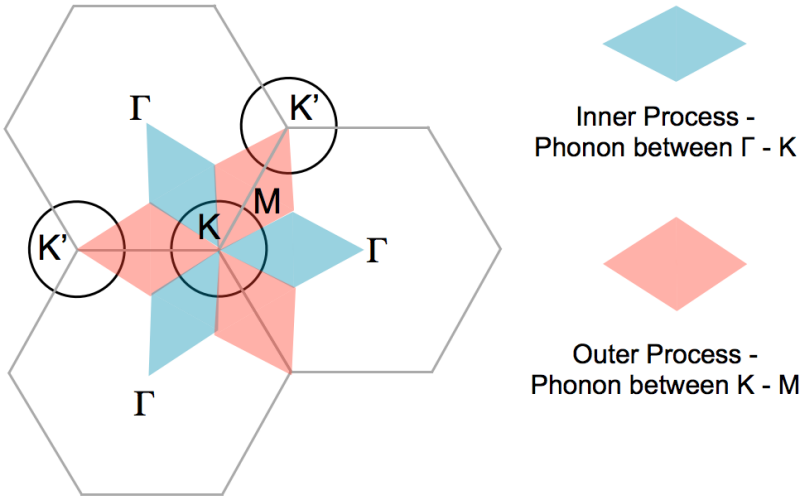

Figure 5.19: Contributing phonons in the double-resonant process around a certain K point. The blue and red rhombi illustrate *inner* and *outer* scattering processes, respectively.

Figure 5.20 shows the two-dimensional electronic dispersion including trigonal warping effects from 0.05 to $2.0\,\mathrm{eV}$. The electronic dispersion was calculated according Ref. [16]. The shadowed region highlights the angular segment in which the excitation takes place for *inner* processes. The other directions are neglected for better graphical representation but would also contribute depending on sample orientation and polarization. The white curve indicates an excitation energy at $1.9\,\mathrm{eV}$ close to our experimental values. The white curve is now transferred to the two-dimensional phonon dispersion yielding the contributing phonon frequencies in the two-dimensional Brillouin zone.
The phonon dispersions of the TO, the LA and its combination the TO + LA are shown in Fig. 5.20 (b) - (d). The trigonal warping of the TO phonon is opposite to that of the electronic dispersion. However, the electrons and phonons in the double-resonant process stem from different sides of the K point and therefore the white curve yields no angular dependence in the two-dimensional Brillouin zone which is reflected in the narrow lineshape of the $2D$ mode in single-layer graphene.
The LA phonon branch, on the other hand, exhibits a strong angular dependence and consequently a variety of phonon frequencies. Direct determination of the frequencies is represented in 5.20 (d) in which the sum of the TO and LA phonon branch is depicted. The excitation at $1.9\,\mathrm{eV}$ induces a range of phonon frequencies from $\approx 2450\,\mathrm{cm}^{-1}$ at $0\,^\circ$ which is along the high-symmetry line to $\approx 2520\,\mathrm{cm}^{-1}$

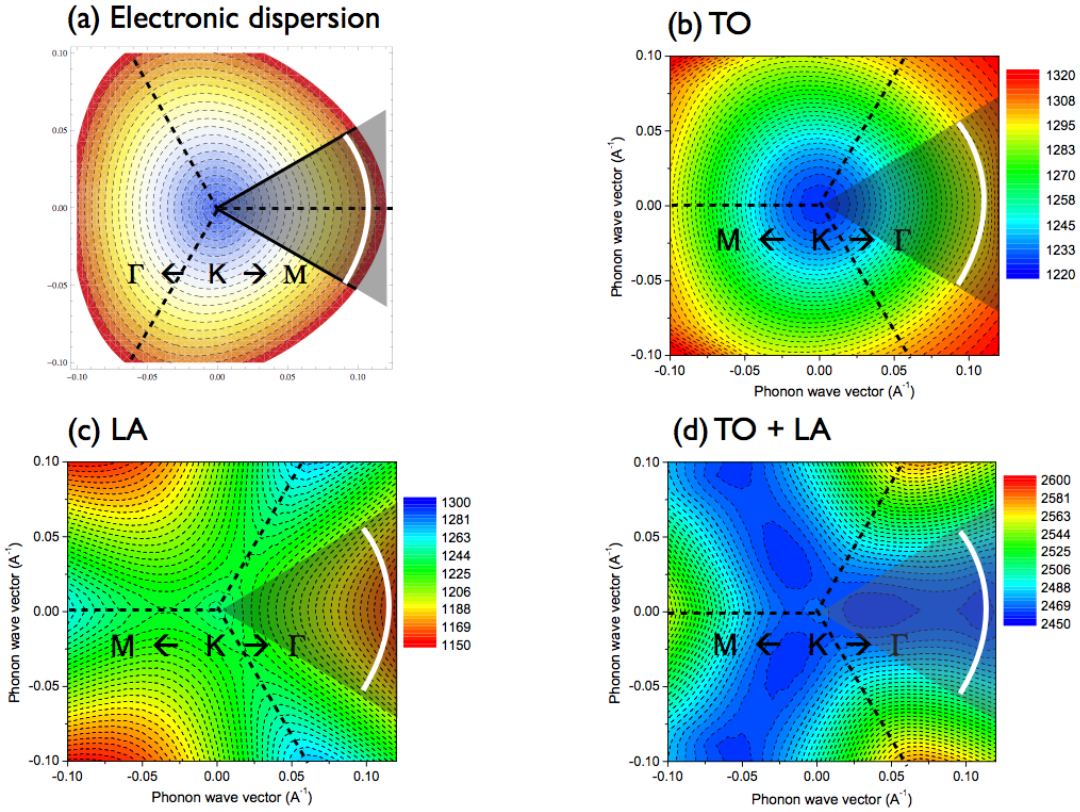

Figure 5.20: (a) Electronic dispersion of graphene including the trigonal warping effect. The shadowed triangle highlights the region of *inner* scattering processes. By rotating this triangle about 120° the other *inner* processes are obtained. The white curve represents an excitation of 1.9 eV. This excitation curve is used for the determination of Raman frequencies in the phonon dispersions. The transverse optical (TO) and longitudinal acoustic (LA) phonon branch are depicted in Fig. (b) and (c), respectively. The excitation line yields equal frequencies for the TO phonon, whereas the LA exhibits a strong angular dependence resulting in different contributing phonon frequencies. The sum of both phonon branches is shown in (d).

at 30 °. This yields the angular segment of 60 ° for *inner* processes and is in excellent agreement to the asymmetric lineshape from Fig. 5.18. However, the decreasing intensity towards higher frequencies cannot be explained by the contour plots. A very broad peak with a constant Raman intensity would be expected. The Raman intensity is mainly determined by the electron-phonon coupling and the optical matrix elements. In Ref. [164] the angular dependence of the electron-phonon matrix element of different phonon branches was discussed. However, the electron-phonon coupling of both the TO and the LA phonon branch is almost constant in the above-mentioned angular segment [164]. The optical strength of a transition is determined by the optical matrix element and the joint density of states; it is depicted for an excitation of 2.5 eV in Fig. 5.21 (a). A detailed description on the calculation method is provided in Ref. [167]. The optical matrix element shows a strong angular dependence with large

contributions along the high-symmetry lines. In Fig. 5.21 (b) the angular dependence of the matrix element is converted to phonon frequencies according the angular dependence of the TO + LA phonon branch. The progress of the optical matrix element is close to the change of the intensity as function of the phonon frequency. One should note that the optical matrix element does not vanish and increases again when turning towards *outer* processes. The TO + LA mode highlights two important things. First the importance of a contribution of *inner* processes. Though *outer* processes are allowed by symmetry for the TO + LA mode, however no such mode is observed or has been reported so far. The reason for this might arise from vanishing electron-phonon coupling. Second, due to the angular dependence of the LA phonon branch it allows to probe the double-resonant scattering paths in two dimensions. The two-dimensional phonon dispersion is also probed with the $2D$ mode, however cannot be resolved due to a missing angular dependence. However, the strongest contributions still come from the high-symmetry line.

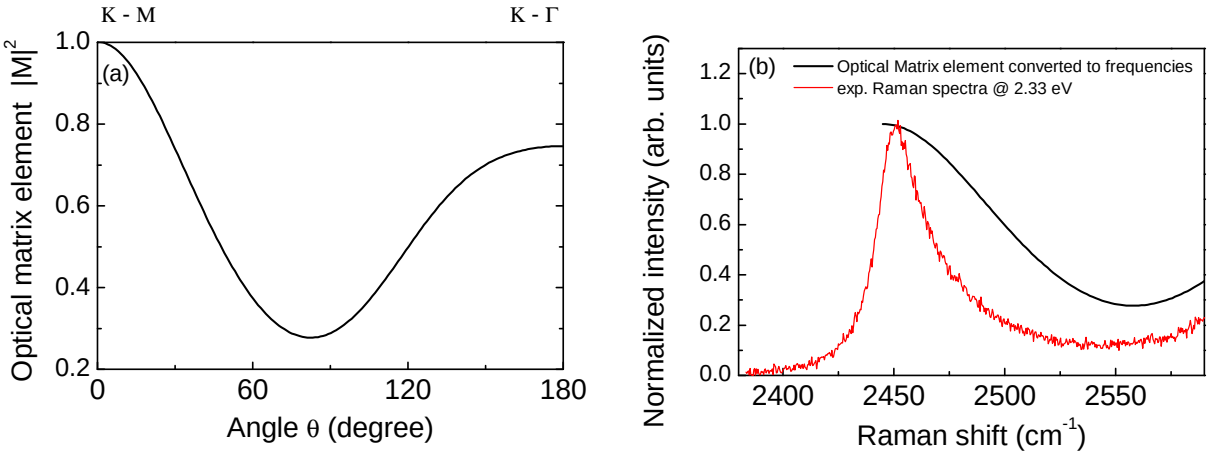

Figure 5.21: (a) Angular dependence of the optical matrix element $|M|^2$ in graphene at a distance of 2.5 eV. Zero and 180° degrees corresponds to the high symmetry line along K - Γ and K - M, respectively. (b) depicts the Raman spectrum of the TO + LA combination mode in comparison to the optical matrix element. In this figure the angle are related to Raman frequencies according the two-dimensional phonon dispersion from Fig. 5.20.

To further support the above mentioned points, a two-dimensional calculation of the TO + LA mode is considered. The calculation includes the calculation of the optical matrix elements and the electron-phonon coupling. The phonon and electronic dispersion is based on density functional theory and corrections of GW. More detailed information can be found in Ref. [88]. The comparison of experimental data of the TO + LA mode and the two-dimensional calculation is depicted in Fig. 5.22. The peak shape and the asymmetry is well reproduced by the calculation. The shoulder peak, however, at the high frequency side is a noise artefact as a consequence of the limited reciprocal space sampling.[†].

[†]Private communication with F. Mauri: Calculations are based on the method of Ref. [88] The method, however, is more precise than that of Ref. [88] and more converged in terms of reciprocal space sampling.

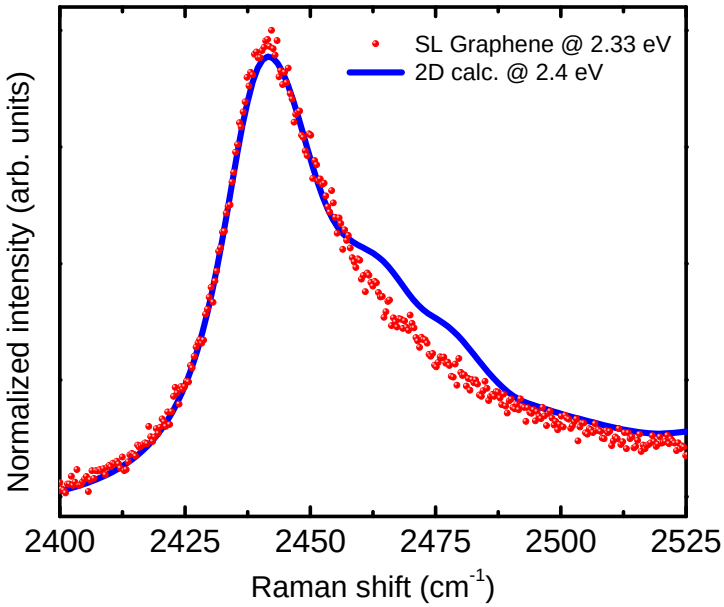

Figure 5.22: Comparison of experimental spectrum of single-layer graphene with a two-dimensional calculation of the double-resonant TO + LA mode including matrix elements. Calculation is based on the methods of Ref. [88], but more precise in terms of convergence. The calculation was provided by F. Mauri.

5.3.3 Evolution with number of layers and excitation energy

The evolution of the TO + LA mode with the number of layers is investigated. Since the bandstructure splits in two and three bands for bilayer and trilayer graphene, respectively, more contributions are expected. The TO + LA mode is shown in Fig. 5.23 at 2.33 eV excitation energy for up to three layers graphene. A broadening of the peak as a result of different contributions is observed. The red dashed line represents one-dimensional calculations of the peak. As expected the calculation shows more contributions for additional layers of graphene reflecting the splitting of the electronic structure. The calculation only includes scattering paths along the high-symmetry direction. However, they give the dominant contribution and provide insight into the different contributions of the bands. The calculation method was described in detail in Chapter 5.2.2. However, here two phonon branches were used for the calculation. Figure 5.24 shows the TO + LA mode of bilayer graphene for three different excitation energies. This Raman peak is sensitive to changes in the electronic bandstructure. At ≈ 2 eV the wave vectors satisfying the double-resonant process yield similar frequencies. Only at higher energies, additional contributions can be resolved. Therefore a change of the linewidth is expected when tuning the excitation energies in few-layer graphene samples.

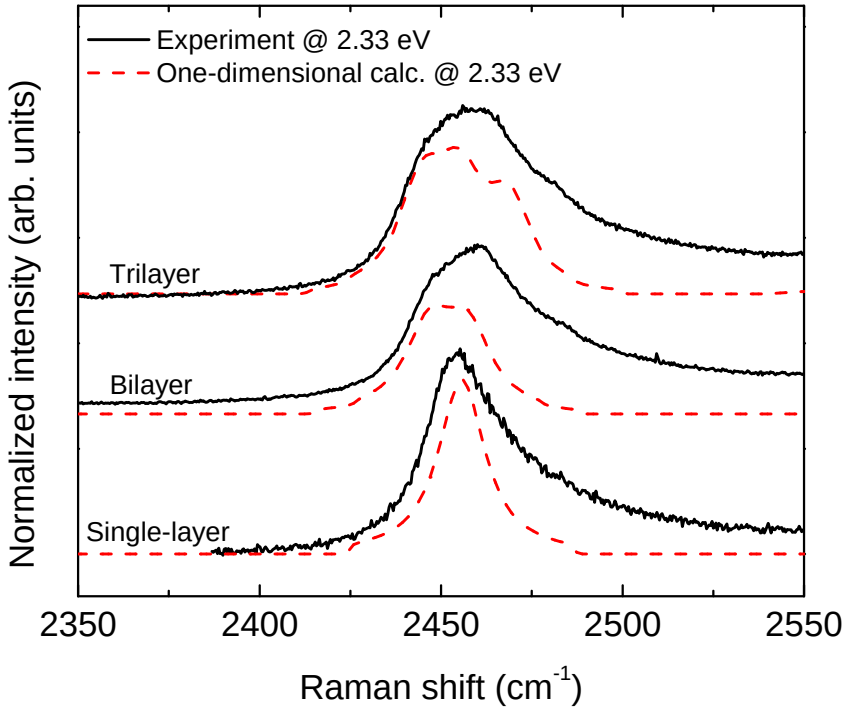

Figure 5.23: TO + LA combination mode at 2.33 eV for single-layer, bilayer and trilayer graphene compared to one-dimensional calculations.

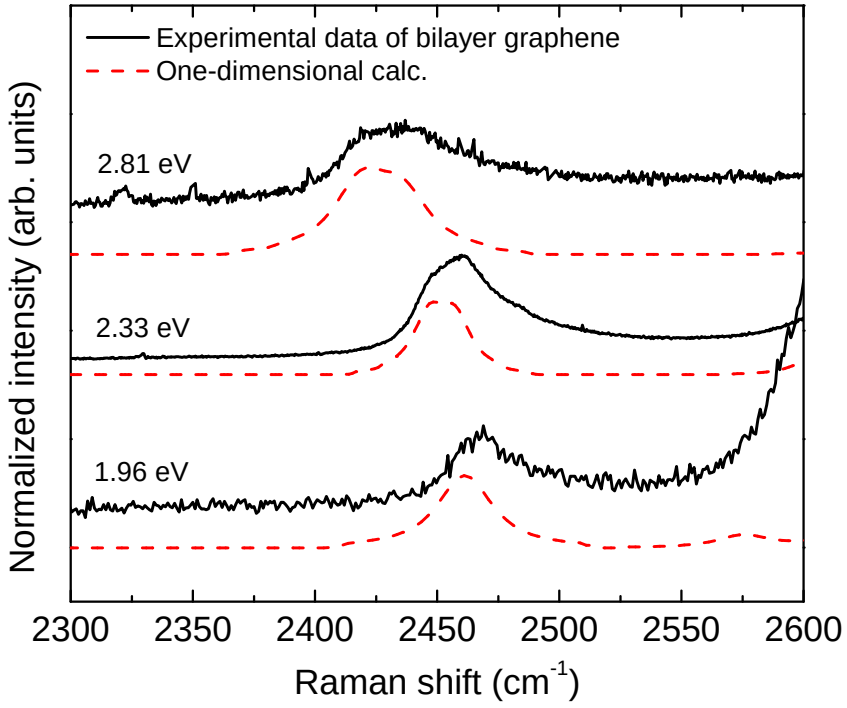

Figure 5.24: Dispersion of the TO + LA mode with increasing excitation energy for bilayer graphene. The experimental obtained spectra are illustrated by solid black lines, the one-dimensional calculation is represented by dashed red lines.

5.4 Double-resonant Raman scattering in graphite

In the previous sections the double-resonant process in single and bilayer graphene was considered. In this section the $2D$ mode in graphite is investigated and the concept of $inner$ and $outer$ processes is applied. The $2D$ mode in graphite mainly consists of two broad peaks as depicted by the red spectrum in Fig. 5.25 and compared to single (black dots) and bilayer graphene (blue) at an excitation energy of 2.33 eV.

In contrast to the approach followed up here, Reference [169] suggests a geometrical approach for the double-resonant process in few-layer graphene and graphite. Here, a quantization of the first Brillouin zone, which is caused by the finite size of the c axis, gives rise to a set of discrete peaks. For graphite an infinite number of peaks is proposed. A spectrum obtained from a one-dimensional calculation of single-layer graphene according the procedure in Chapter 5.2.2 is also shown in order to obtain accurate frequencies of $inner$ and $outer$ processes. Since the $outer$ process in the calculation exhibits a less pronounced intensity, the position is indicated by a straight line.

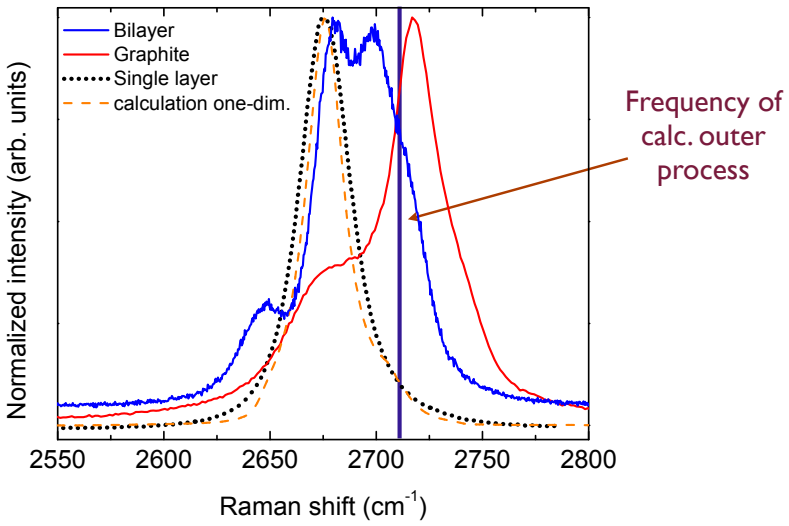

Figure 5.25: $2D$ mode of graphite (red), bilayer graphene (blue), single-layer graphene (black dots) and a one-dimensional calculation (orange dashed line) by comparison at an excitation energy 2.33 eV. Since the intensity of the calculated $outer$ process is very weak, the frequency is shown with the solid line.

The calculated contributions of single-layer graphene should in principle reproduce the phonon frequencies of graphite, since the graphite bandstructure can be very well approximated by the bandstructure of single-layer graphene. From Fig. 5.25 it can be concluded that the $2D$ mode in graphite is also composed by $inner$ and $outer$ processes. As shown in the previous section, the high intensity peaks in bilayer graphene arise from $inner$ processes in agreement with the one-dimensional calculation. How-

ever, in contrast to single- and bilayer graphene the intensities of the particular contribution in graphite are reversed. The assigned *outer* process possess a dominant intensity. This might be due to additional bands in the electronic structure resulting in additional scattering paths in two-dimensions.
In Chapter 5.3.1 the TO + LA combination mode turned out to be useful for probing the phonon dispersion. Since the dominant contribution stems from the high-symmetry line of the *inner* processes it is possible to determine which of the two phonon contributions couple to the LA phonon. The two contributions of graphite are labeled as D_1 and D_2.
The $2D$ mode is then composed as follows:

$$2\mathrm{D}_1 = 2\mathrm{TO}_1, \tag{5.4}$$

and

$$2\mathrm{D}_2 = 2\mathrm{TO}_2, \tag{5.5}$$

while the TO + LA mode consists of:

$$\mathrm{TO} + \mathrm{LA} = \mathrm{TO}_x + \mathrm{LA}, \tag{5.6}$$

and consequently the TO_1, TO_2 can be directly derived from Eq. 5.4 and Eq. 5.5. The LA phonon is derived from the following expression and assigned in the corresponding phonon dispersion:

$$\mathrm{LA} = (\mathrm{TO} + \mathrm{LA}) - \mathrm{TO}_\mathrm{x}, \tag{5.7}$$

while x is either 1 or 2 for the first or the second contribution in graphite.

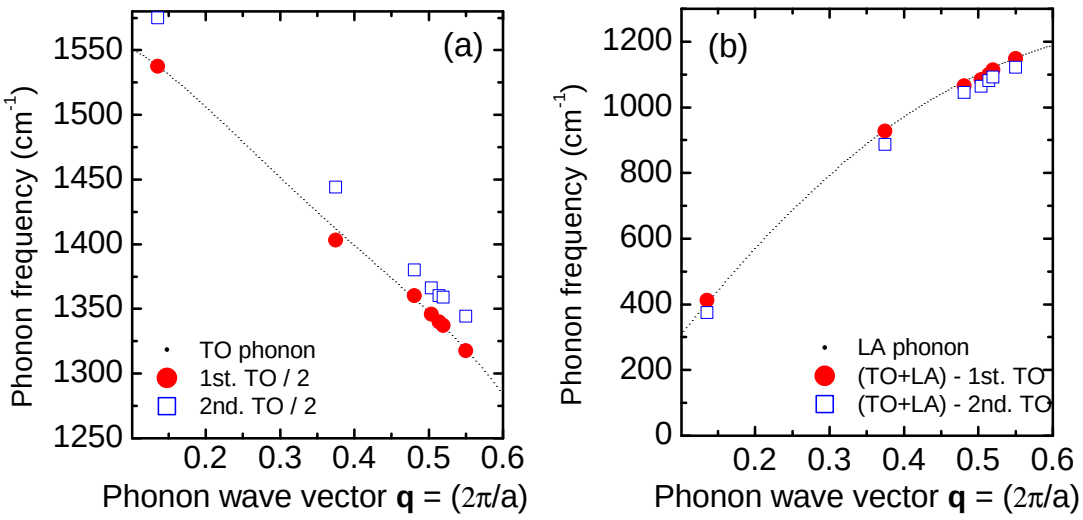

Figure 5.26: Figure (a) shows the transverse optical (TO) phonon branch along the Γ - K direction (*inner* process). The red dots and blue squares illustrate the particular TO phonon. (b) shows the longitudinal acoustic phonon branch along the Γ - K direction (*inner* process). The red dots and blue squares represent the frequency difference of the measured TO + LA mode and the TO phonon.

The frequencies of the TO_1, the TO_2 and the LA phonon are plotted in Fig. 5.26 with the phonon dispersion of the TO and LA phonon branch. The TO phonon dispersion was obtained according the procedure of Chapter 5.1.2. The LA phonon was obtained accordingly and scaled to recent results of Grüneis *et al.* [157].
The experimental data were obtained by fitting the $2D$ mode with two Lorentzians while the TO + LA mode was fitted with one Lorentzian at the main contribution, which stems from the high-symmetry line based on the conclusions drawn from Chapter 5.3.1. Since the $2D$ mode is the second order overtone of the D mode, the $2D$ mode frequency can be in a good approximation divided by two in order to obtain the first order frequency. This is shown in Fig. 5.26 (a). The theoretical obtained frequencies of TO_1 matches perfectly the TO phonon dispersion along the Γ - K direction. It should be noted that the phonon wave vectors were exclusively determined for $inner$ processes. The LA phonon is plotted in Fig. 5.26 (b). It can be concluded that TO_1 couples to the LA phonon for the TO + LA combination mode in graphite and stems from an $inner$ process. This is in agreement with the one-dimensional calculation and the comparison to single and bilayer graphene depicted in Fig. 5.25.

5.5 Inner and outer processes in the UV

Another approach for the investigation of *inner* and *outer* processes is ultraviolet (UV) Raman spectroscopy. First the double-resonant process for single-layer graphene is calculated according the procedure of Chapter 5.2.2 and then compared to the experimental measurements of graphene and graphite. Figure 5.27 shows the $2D$ mode for different excitation energies. At lower excitation energies, one can clearly distinguish two different contributions. The main contribution stems from *inner* process, while the higher frequency contribution stems from *outer* processes. When progressing to higher excitations, the intensity increases for *inner* processes as illustrated in the inset of Fig. 5.27. This can be explained with density of states arguments. The one-dimensional calculation of the Raman cross section only includes the electron and the phonon density of states while the matrix elements are taken as constant. When progressing to higher excitation energies, the slope of the bands between the K- and the M-point exhibit a much smaller slope than in the vicinity of the K-point that has a linear dispersion relation. Between the K- and the M-point the slope of the bands is less pronounced resulting in a larger electronic density of states.

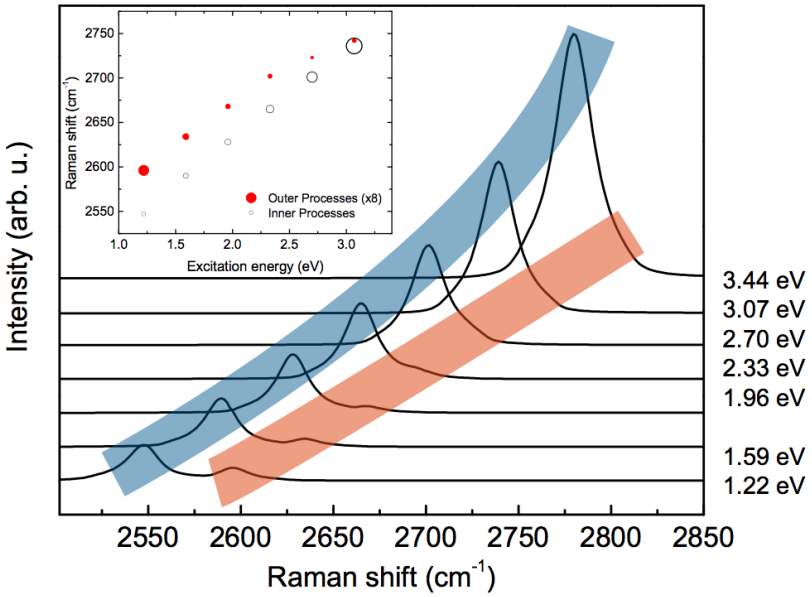

Figure 5.27: Excitation energy dependence of the calculated double-resonant process for single-layer graphene. Blue and red shaded area highlight *inner* and *outer* processes, respectively. The inset shows the relative intensities for both *inner* and *outer* processes. Note that the *outer* processes are multiplied by a factor of 8.

One may argue that all matrix elements should be taken into account and should be integrated in two-dimensions. Venezuela *et al.* [88] compared their full two-dimensional calculation including all matrix elements to a calculation with the matrix elements taken as constant. Inclusion of the matrix element yields that *inner* processes are stronger by a factor of ≈ 4 compared to a calculation without matrix

elements. This is a consequence of a two-dimensional calculation, since for *outer* processes there is a much higher density of states in two dimensions while *inner* processes are enhanced when including the optical matrix elements. This is neglected in our calculation, but gives similar ratios of *inner* and *outer* processes below 2 eV. To support this the wave vector dependence is shown in Fig. 5.28. The two contributions are depicted as function of the phonon wave vector. *Inner* processes are highlighted in blue, *outer* processes are highlighted in red. One can clearly see an increasing contribution of *inner* processes as function of increasing excitation energy. *Outer* processes, however, remain more or less constant. This is due to the fact that the electronic dispersion is approximately linear between the Γ and the K-point.

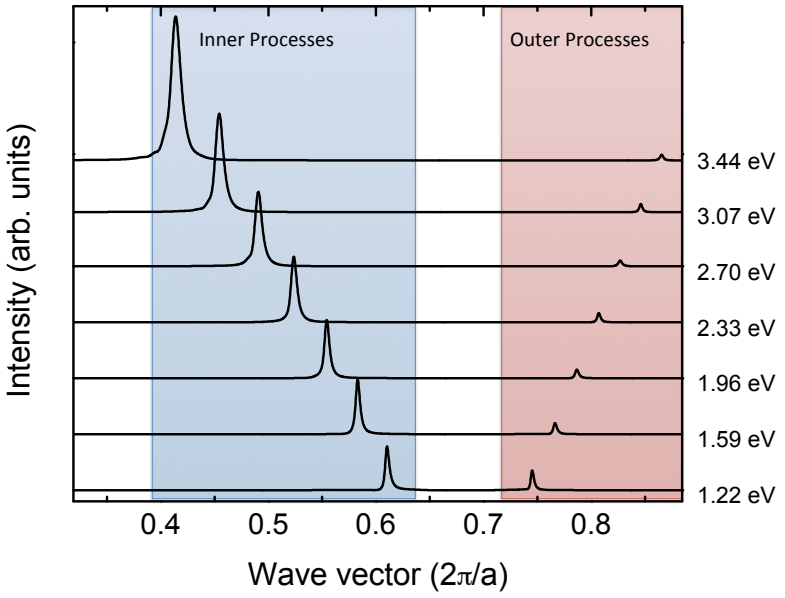

Figure 5.28: Wave vector dependence of *inner* and *outer* processes for various excitation energies. Inner and *outer* processes are highlighted in blue and red shaded areas, respectively. Intensities are a consequence of both the electronic and phonon density of states.

Further it appears from Fig. 5.27 that both contributions merge into each other. This can be clearly seen when we look at the excitation dependence. The shift of the two contributions is shown in Fig. 5.29. The excitation energy ranges from 1.2 eV up to 4.8 eV. The contributing *inner* and *outer* processes are illustrated as black squares and red rhombi, respectively. The offset in frequency between *inner* and *outer* processes might come from the one-dimensional calculation. As shown in Chapter 5.2.4, scattering paths of *outer* processes which possess an offset yield lower phonon frequencies.
Inner processes exhibit a linear relation over a broad excitation range with a shift rate of 102.5 cm^{-1}/ eV. The black squares represent *outer* processes and follow the behavior of the *inner* processes from 1.2 eV up to 2.35 eV with the same shift rate. At this energy a kink sets in changing the shift rate to 52.3 cm^{-1}/ eV, which is approximately half the value. This is due to the phonon dispersion having a less steep slope

at higher excitation energy between the K - M direction. At low excitation energies up to $2.5\,\text{eV}$, the two contributions are well separated. A crossing of *inner* and *outer* processes occurs at around $3.2\,\text{eV}$. For *outer* processes the shift rate saturates and approaches a shift rate close to $0\ \text{cm}^{-1}/\,\text{eV}$, whereas for *inner* processes the shift rate increases almost exponentially. The experimental data of graphene and graphite are illustrated by circles. The contributions of graphite are split in two main contribution. It should be noted that again without any rescaling, the absolute Raman frequencies match the calculation very well. Both the peak of graphene and the first peak of graphite can be assigned to *inner* processes within the visible excitation. Above $3\,\text{eV}$ only two excitation energies were measured, however both are closer to the *inner* process. The *outer* process is rarely visible in the Raman spectrum.

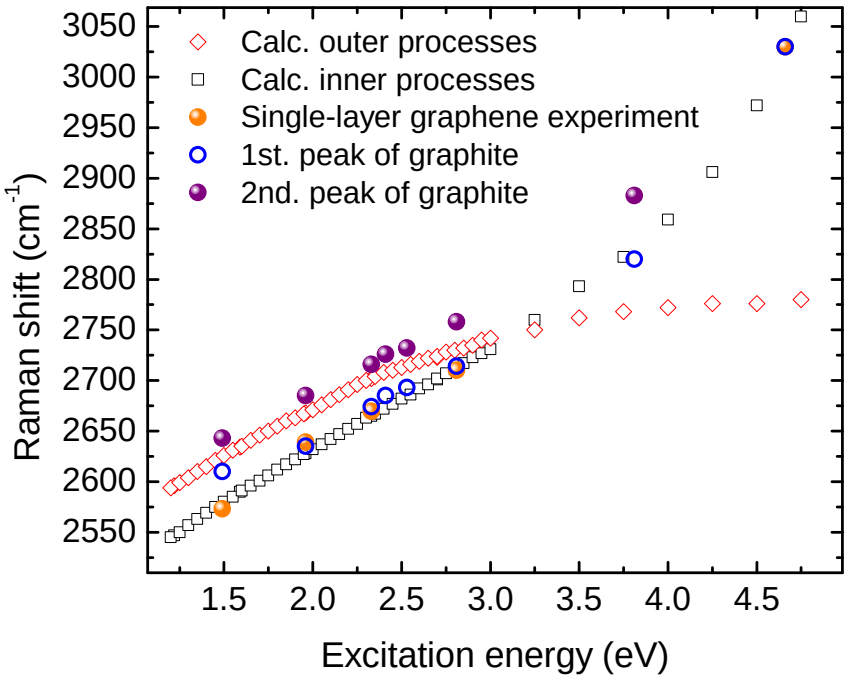

Figure 5.29: Excitation dependence of *inner* (black squares) and *outer* processes (red dots) in single-layer graphene from $1.2\,\text{eV}$ up to $4.8\,\text{eV}$. *Inner* processes exhibit a perfect linear relation over a broad excitation range up to $3.25\,\text{eV}$ with a shift rate of $102.5\ \text{cm}^{-1}/\,\text{eV}$.

The Raman spectra at $4.66\,\text{eV}$ for graphite and single/few-layer graphene are depicted in Fig. 5.30. The experimental obtained spectra are compared to one-dimensional calculations of single-layer graphene and bilayer graphene (according the calculation method of Chapter 5.2.2). The contribution of the *outer* process is highlighted by the solid line, since the intensity in both the experiment and the calculation is very weak. The graphite sample shows a very strong contribution at around $3200\ \text{cm}^{-1}$ which can be attributed to either the second order G, a combination of $D + G$ or the second order D' mode.

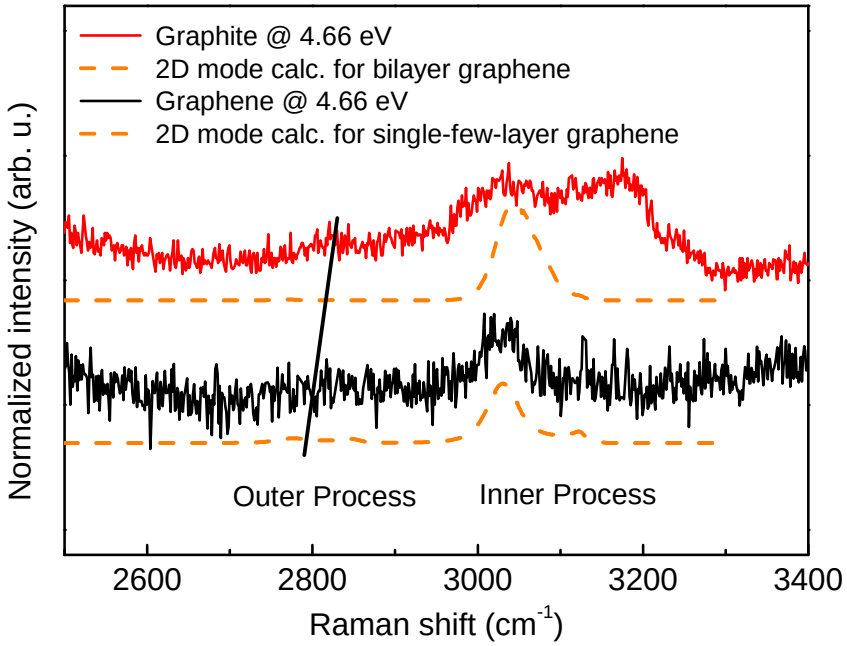

Figure 5.30: Raman spectra of graphite (red) and single / few-layer graphene (black) at $4.66\,\mathrm{eV}$ compared to one-dimensional calculations (orange dashed line) of the Raman cross section for single and bilayer graphene. The black solid line indicates the contribution of the *outer* process.

5.6 Intensity dependence on excitation energy

So far the double-resonant Raman modes were used for the determination of scattering paths, probing phonon and electronic dispersions. Here, the relative intensities of the TO + LA and the $2D$ mode are explored. It has been shown by Venezuela *et al.* [88] that the ratio of integrated intensities of the $2D$ over the TO + LA mode increases for increasing excitation energy. The broadening parameter γ_{tot} is the sum of the electron and hole linewidths and can be written as [88]:

$$\gamma_{tot} = \gamma_{electron} + \gamma_{hole}, \tag{5.8}$$

and has two contributions, an intrinsic due to electron-phonon coupling and an extrinsic which is depending on the number of defects. Since our samples are nearly defect-free, the focus is put on the electron-phonon scattering contribution in the following discussion. The Raman matrix element from Chapter 5.2.2 is considered and yields:

$$K_{2f,10} = \sum_{a,b,c} \frac{M}{(E_l - E_a - i\gamma_{tot})(E_l - \hbar\omega_{\mathbf{q}} - E_b - i\gamma_{tot})(E_l - 2\hbar\omega_{\mathbf{q}} - E_c - i\gamma_{tot})}. \tag{5.9}$$

The numerator is abbreviated and contains all matrix elements. E_l is the excitation energy and the incoming and the outgoing photon is expressed in E_l and E_l - $2\hbar\,\omega_q$, respectively. Initial, intermediate and final electronic states are represented by E_x with x being either a, b or c. The broadening parameter γ_{tot} is steadily increasing with increasing excitation energy and thus changing the condition that satisfy the double-resonance. Therefore in agreement with theoretical calculation of Ref. [88] the intensity of the $2D$ mode decreases with increasing excitation energy. The influence of the electron-phonon and impurity scattering to the electronic linewidth γ_{tot} broadening is depicted in Fig. 5.31 (a) and (b), respectively. Here the on-site and hopping defects are normalized to defect concentration and α_{hopp} is on the order of 10^{13} eV^2 cm^2 for low defect concentrations of 10^{11} cm^2.

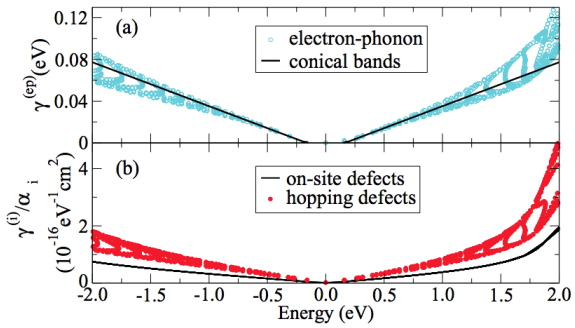

Figure 5.31

(a) Electron-phonon scattering contribution to the electronic linewidth γ_{tot} in comparison to an approximation of conic bands with two phonons. In (b) the contribution of both on-site and hopping impurity scattering is shown. The "i" refers to on-site or hopping defects and α normalizes to the defect concentration. Taken from Ref. [88]

The integrated areas are dependent on γ_{tot} in units of meV and obey the following relationships [88]:

$$A(2D) = \frac{9374}{\gamma_{tot}^2 + 48.5^2},$$
$$A(TO + LA) = \frac{438}{\gamma_{tot}^2 + 59.6^2}. \tag{5.10}$$

The ratio of integrated intensities of the (TO + LA) over the $2D$ mode for different excitation energies and hence different values of γ_{tot} and the experimental results is shown in Fig. 5.32. Though there are slight deviations, the measured ratios are in very good agreement with calculations. The deviations might partly stem from additional broadening of the electronic linewidth due to defects as shown in Fig. 5.31 (b). Therefore by comparing the ratio of the TO + LA mode and the $2D$ mode of different samples the influence of impurity scattering can be obtained directly from the Raman experiment.

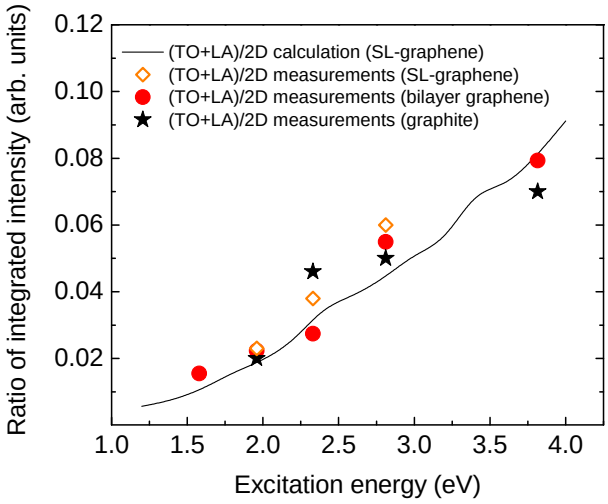

Figure 5.32

Ratio of integrated intensities of the (TO + LA) over the $2D$ mode for various excitation energies. Calculations were provided from the authors of Ref. [88]. The increase is a consequence of an increasing broadening parameter γ_{tot} towards higher excitation energies.

5.7 Summary

In this chapter the scattering paths of the double-resonant Raman process were investigated. The Raman spectra in free-standing bilayer graphene were analyzed focussing on the phonon frequency and the relative strength of the different contribution. By comparing the experimental results to one-dimensional calculation, the $2D$ mode was found to exhibit contributions of both $inner$ and $outer$ processes, *i.e.* phonon contributions from parts of the Brillouin zone on both sides of the K-point. The combination of $inner$ and $outer$ processes can qualitatively explain the relative strength of the Raman intensity of the $2D$ mode contributions. Further, the notation of $inner$ and $outer$ processes was discussed considering scattering paths in two dimensions and were found to originate from different sides of the K-point. In consequence $inner$ and $outer$ processes can be maintained under consideration of the scattering paths. The origin of the TO + LA combination mode was explored in Chapter 5.3. The discussion of $inner$ and $outer$ processes was reversed, since the discussion about scattering processes usually start from the excitation of the electrons in the two-dimensional Brillouin zone. The measured phonons were analyzed and assigned to scattering processes of the electron along the K - M direction ($inner$ processes). Further this mode exhibits an asymmetric tail towards higher frequencies. This was explained with the strong angular dependence of the longitudinal acoustic (LA) phonon branch. The decrease in intensity was attributed to the fact that the optical matrix element also shows a strong angular dependence. In consequence it was shown that the contributing processes stem from the high-symmetry direction.
The evolution with the numbers of layers and with excitation energy is determined by the unique electronic structure which changes upon stacking graphene layers on top of each other. The evolution of both the number of layers and excitation energy was simulated within a simple one-dimensional calculation. The behavior could very well be reproduced. Only a two-dimensional calculation including all matrix reproduces the asymmetric tail. This further supported the approach of an integration in one-dimension since the dominant contribution stems thereof.
The experimental $2D$ mode in the UV matches the calculated frequencies of $inner$ processes much better than $outer$ processes. Finally, the excitation dependent broadening was investigated in close agreement with theoretical studies of Venezuela *et al.* [88].

6 Summary and outlook

In this work inelastic light scattering has been applied to probe both the electronic and phonon structure of low-dimensional carbon systems. Raman spectroscopy is a sensitive tool for the investigation of electronic and vibrational properties of carbon systems. The first part dealt with the access to the exciton binding energy in metallic carbon nanotubes. Due to their reduced dimensionality, even metallic nanotubes exhibit an exciton binding energy that dominates the optical transitions at room temperature. It has been shown that by applying temperature the optical transition undergoes a shift towards lower transition energies. This behavior is found for both one metallic and one semiconducting nanotube. However, at temperatures related to the exciton binding energy a sudden upshift in the transition energy was observed. This upshift could only be observed for metallic nanotubes and was related to the dissociation of excitons. A binding energy of ≈ 50 meV was obtained which is in excellent agreement with theoretical predictions and absorption measurements. The interpretation was further supported by an analysis of the Raman intensity. Excitons enhance the optical transitions that result in an increased Raman intensity. When the excitons are dissociating the optical transition is determined by free carrier excitations and consequently the Raman susceptibility decreases.

Though a direct measurement technique was applied to obtain access to the excitonic binding energies, several fundamental questions remain. For example, how the excitonic binding energy changes in higher optical transitions. In this work, the first optical transition E_{11} of one metallic carbon nanotube were probed. Ideally, different chiralities of individual carbon nanotubes should be investigated in different environments since the dielectric environment has strong influences on the actual exciton binding energy. Then it would be possible to correctly describe many-body interactions for the first and higher transitions. However, Raman scattering has proven to be a powerful method to investigate correlated electron-hole interactions in metallic systems.

The second part revealed the scattering paths within the double-resonant Raman process for single, bilayer graphene and graphite.

The double-resonant Raman modes provide information about the number of layers, doping levels, defect densities, strain and stress and is therefore a key in the characterization of carbon systems. Therefore an understanding of the fundamental scattering processes is necessary in order to interpret changes in the Raman spectrum. Concerning the scattering processes, there is an on-going debate about the so-called $inner$ and $outer$ processes, where $inner$ ($outer$) refers to scattering by phonons with wave vectors between Γ - K (K- M). Here, the scattering processes of free-standing bilayer graphene were investigated. In free-standing graphene the environmental concerns are minimized to allow the probing of the intrinsic electronic and vibrational properties. Bilayer graphene exhibits a more complex bandstructure than

single-layer graphene providing different scattering contributions to the $2D$ mode. As a consequence of the electronic bandstructure four contributions were analyzed and compared to one-dimensional calculations of the Raman cross section. Significant evidence was discovered for a contribution of both $inner$ and $outer$ processes. This interpretation further permits the explanation of the relative strengths of the particular contributions. Further the terms of $inner$ and $outer$ processes were discussed considering scattering paths in two-dimensions. The notation of $inner$ and $outer$ processes can be maintained and extended to scattering processes on both sides of the K point.

A combination mode of a transversal optical (TO) and longitudinal acoustical (LA) mode was investigated. This mode exhibits an opposite dispersion than the 2D mode. The contributing phonons could be assigned to originate from so-called $inner$ processes, i.e. phonons along the Γ - K direction. Further the asymmetric lineshape has been analyzed and attributed to a two-dimensional contribution. This allowed a direct measurement of the two-dimensional phonon dispersion and the derivation of a lower limit of the angular segment in which the scattering processes take place. The measurement of the TO + LA mode in graphene systems permits to probe both the two-dimensional electronic structure and two-dimensional phonon dispersion due to the strong angular dependence of the contributing LA phonon.

In addition the main contribution to the double-resonant process were determined to lie along the high-symmetry directions. The evolution with the number of layers and with excitation is in excellent agreement with the one-dimensional calculation and further supports the dominant scattering processes along the high-symmetry line.

The obtained results were then applied to graphite. The TO + LA mode permits to probe the LA phonon branch dispersion. Since only $inner$ processes are able to couple to the TO and LA phonon to form the TO + LA mode, it was possible deduce the contribution of the TO phonon that couples to the LA phonon.

The progress of $inner$ and $outer$ processes towards excitation energies in the UV was considered theoretically and compared to experimental results. Here only $inner$ processes are able to explain the shift rate with excitation energies as the $outer$ process phonons saturate and exhibit a shift rate close to 0 cm^{-1} / eV. Again, the one-dimensional calculation gave a very good approximation of the absolute phonon frequencies without any rescaling.

Though strong evidences for $inner$ processes and scattering processes along the high-symmetry line were found, a full understanding of the scattering paths is still missing, since scattering paths of the entire Brillouin zone contribute to the Raman spectrum. The notation of $inner$ and $outer$ processes correctly describe the scattering paths in one-dimension and can also be applied to scattering paths in two dimensions. However, in two-dimensions this notation is restricted to electronic excitations or phonons from a distinct direction in the Brillouin zone. Here, one defines $outer$ processes as electronic excitations between the Γ and K direction, while $inner$ are electronic excitations between the K-M direction.

As a matter of fact, a consideration of scattering paths along the high-symmetry line produce very good results and simplifies the analysis of scattering paths and hence changes in both the electronic bandstructure and phonon dispersion due to external perturbations.

Bibliography

[1] S. Reich, C. Thomsen, and J. Maultzsch, *Carbon Nanotubes: Basic Concepts and Physical Properties* (Wiley-VCH, Berlin, 2004).

[2] A. Jorio, M. Dresselhaus, R. Saito, and G. F. Dresselhaus, *Raman Spectroscopy in Graphene Related Systems* (Wiley-VCH, Berlin, 2011).

[3] K. Novoselov, A. Geim, S. Morozov, D. Jiang, Y. Zhang, *et al.*, "Electric field effect in atomically thin carbon films", Science **306**(5696), 666–669 (2004).

[4] P. Wallace, "The band theory of graphite", Phys. Rev. **71** (1947).

[5] H. W. Kroto, J. R. Heath, S. C. O. Brien, R. F. Curl, and R. E. Smalley, "C60: Buckminsterfullerene", Nature **318**, 162 (1985).

[6] S. Iijima, "Helical microtubulus of graphitic carbon", Nature **354**, 56 (1991).

[7] S. Iijima and T. Ichihasi, "Single-shell carbon nanotubes of 1-nm diameter", Nature **363**, 603 (1993).

[8] J. Hone, "Phonons and thermal properties of carbon nanotubes", Topics Appl. Phys. pp. 273–286 (2001).

[9] V. Perebeinos, J. Tersoff, and P. Avouris, "Electron-phonon interaction and transport in semiconducting carbon nanotubes", Phys. Rev. Lett. **94**, 086 802 (2005).

[10] P. L. McEuen, M. Bockrath, D. H. Cobden, Y.-G. Yoon, and S. G. Louie, "Disorder, pseudospins, and backscattering in carbon nanotubes", Phys. Rev. Lett. **83**, 5098–5101 (1999).

[11] S. J. Tans, A. Verschueren, and C. Dekker, "Room-temperature transistor based on a single carbon nanotube", Nature **393**, 49–52 (1998).

[12] J. A. Misewich, R. Martel, J. C. Tsang, S. Heinze, and J. Tersoff, "Electrically induced optical emission from a carbon nanotube FET", Science **300**, 783–786 (2003).

[13] E. S. Snow, F. K. Perkins, E. J. Houser, S. C. Badescu, and T. L. Reinecke, "Chemical detection with a single-walled carbon nanotube capacitor", Science **307**, 1942–1945 (2003).

[14] P. Avouris and J. Chen, "Nanotube electronics and optoelectronics", Materials Today **9**, 46–54 (2006).

[15] P. Avouris, M. Freitag, and V. Perebeinos, "Carbon-nanotube photonics and optoelectronics", Nature Photonics **2**, 341–350 (2008).

[16] A. C. Neto, F. Guinea, N. Peres, K. Novoselov, and A. Geim, "The electronic properties of graphene", Rev. Mod. Phys. **81**(1), 109–162 (2009).

[17] A. A. Balandin, S. Ghosh, W. Bao, I. Calizo, D. Teweldebrhan, F. Miao, and C. N. Lau, "Superior thermal conductivity of single-layer graphene", Nano Letters **8**(3), 902–907 (2008).

[18] L. Changgu, W. Xiaoding, K. J. W., and H. James, "Measurement of the elastic properties and intrinsic strength of monolayer graphene", Science **321**(5887), 385–388 (2008).

[19] A. K. Geim and K. S. Novoselov, "The rise of graphene", Nature Materials **6**, 183–191 (2007).

[20] J.-H. Chen, C. Jang, S. Xiao, M. Ishigami, and M. S. Fuhrer, "Intrinsic and extrinsic performance limits of graphene devices on sio_2", Nature Nanotech. **3**(4), 206–209 (2008).

[21] J. C. Meyer, A. K. Geim, M. I. Katsnelson, K. S. Novoselov, T. J. Booth, and S. Roth, "The structure of suspended graphene sheets", Nature **446**(7131), 60–63 (2007).

[22] X. Du, I. Skachko, A. Barker, and E. Andrei, "Approaching ballistic transport in suspended graphene", Nature Nanotech. **3**(8), 491–495 (2008).

[23] K. I. Bolotin, K. J. Sikes, J. Hone, H. L. Stormer, and P. Kim, "Temperature-dependent transport in suspended graphene", Phys. Rev. Lett. **101**(9), 096 802 (2008).

[24] K. Bolotin, K. Sikes, Z. Jiang, M. Klima, G. Fudenberg, *et al.*, "Ultrahigh electron mobility in suspended graphene", Solid State Commun **146**(9-10), 351–355 (2008).

[25] "The nobel prize in physics 2010", (2011), available online at `http://www.nobelprize.org/nobel_prizes/physics/laureates/2010/`.

[26] K. Novoselov, A. Geim, S. Morozov, D. Jiang, M. Katsnelson, *et al.*, Nature **438**(7065), 197–200 (2005).

[27] M. I. Katsnelson, K. S. Novoselov, and A. K. Geim, "Chiral tunneling and the Klein paradox in graphene", Nature Physics **2**, 620–625 (2006).

[28] Y.-M. Lin, A. Valdes-Garcia, S.-J. Han, D. B. Farmer, I. Meric, *et al.*, "Wafer-scale graphene integrated circuit", Science **332**, 1294–1297 (2011).

[29] F. Xia, D. B. Farmer, Y.-M. Lin, and P. Avouris, "Graphene field-effect transistors with high on/off current ratio and large transport band gap at room temperature", Nano Lett. **10**, 715–718 (2010).

[30] Y. Zhang, T.-T. Tang, C. Girit, Z. Hao, M. C. Martin, *et al.*, "Direct observation of a widely tunable bandgap in bilayer graphene", Nature **459**(7248), 820–823 (2009).

[31] L. Ju, B. Geng, J. Horng, C. Girit, M. Martin, *et al.*, "Graphene plasmonics for tunable terahertz metamaterials", Nature Nanotechnology pp. 1748–3395 (2011).

[32] M. Jablan, H. Buljan, and S. M., "Plasmonics in graphene at infrared frequencies", Phys. Rev. B **80**, 245 435 (2009).

[33] T. Mohiuddin, A. Lombardo, R. Nair, A. Bonetti, G. Savini, *et al.*, "Uniaxial strain in graphene by Raman spectroscopy: G peak splitting, Grüneisen parameters, and sample orientation", Phys. Rev. B **79**, 205 433 (2009).

[34] M. Huang, H. Yan, C. Chen, D. Song, T. Heinz, and J. Hone, "Phonon softening and crystallographic orientation of strained graphene studied by Raman spectroscopy", Proceedings of the National Academy of Sciences **106**, 7304 (2009).

[35] M. Huang, H. Yan, T. F. Heinz, and J. Hone, "Probing strain-induced electronic structure change in graphene by Raman spectroscopy", Nano Lett. **10**(10), 4074–4079 (2010).

[36] O. Frank, M. Mohr, J. Maultzsch, C. Thomsen, I. Riaz, *et al.*, "Raman 2D-band splitting in graphene: Theory and experiment", ACS Nano **5**, 2231–2239 (2011).

[37] A. Ferrari and J. Robertson, "Interpretation of Raman spectra of disordered and amorphous carbon", Phys. Rev. B **61**, 14 095 (2000).

[38] A. G. Walsh, A. N. Vamivakas, Y. Yin, S. B. Cronin, M. S. Ünlü, B. B. Goldberg, and A. K. Swan, "Screening of excitons in single, suspended carbon nanotubes", Nano Lett. **7**, 1485–1488 (2007).

[39] A. Walsh, A. N. Vamivakas, Y. Yin, S. Cronin, M. S. Ünlü, B. Goldberg, and A. Swan, "Scaling of exciton binding energy with external dielectric function in carbon nanotubes", Physica E: Low-dimensional Systems and Nanostructures **40**, 2375–2379 (2008).

[40] C. Faugeras, M. Amado, P. Kossacki, M. Orlita, M. Kühne, *et al.*, "Magneto-Raman scattering of graphene on graphite: Electronic and phonon excitations", Phys. Rev. Lett. **107**, 036 807 (2011).

[41] S. Ryu, M. Y. Han, J. Maultzsch, T. F. Heinz, P. Kim, M. L. Steigerwald, and L. E. Brus, "Reversible basal plane hydrogenation of graphene", Nano Lett. **8**, 4597–4602 (2008).

[42] H. Telg, J. Maultzsch, S. Reich, F. Hennrich, and C. Thomsen, "Chirality distribution and transition energies of carbon nanotubes", Phys. Rev. Lett. **93**, 177 401 (2004).

[43] J. Maultzsch, H. Telg, S. Reich, and C. Thomsen, "Radial breathing mode of single-walled carbon nanotubes: Optical transition energies and chiral-index assignment", Phys. Rev. B **72**, 205 438 (2005).

[44] P. May, H. Telg, G. Zhong, J. Robertson, C. Thomsen, and J. Maultzsch, "Observation of excitonic effects in metallic single-walled carbon nanotubes", Phys. Rev. B **82**, 195 412 (2010).

[45] C. Thomsen, S. Reich, and J. Maultzsch, "Resonant Raman spectroscopy of nanotubes", Phil. Trans. R. Soc. Lond. A **362**, 2337–2359 (2004).

[46] M. S. Dresselhaus, G. Dresselhaus, R. Saito, and A. Jorio, "Exciton photophysics of carbon nanotubes", Annu. Rev. Phys. Chem. **58**, 719–47 (2007).

[47] R. Saito, M. Hofmann, G. Dresselhaus, A. Jorio, and M. S. Dresselhaus, "Raman spectroscopy of graphene and carbon nanotubes", Advances in Physics. **60**, 413–550 (2011).

[48] M. Dresselhaus, A. Jorio, and R. Saito, "Characterizing graphene, graphite, and carbon nanotubes by Raman spectroscopy", Annu. Rev. Condens. Matter Phys. **1**, 89–108 (2010).

[49] L. D. Landau, "Zur Theorie der Phasenumwandlungen,", Phys. Z. Sowjetunion **1**, 26 (1937).

[50] R. E. Peierls, "Quelques proprietes typiques des corpses solides", Ann. Inst. Henri Poincare **5**, 177 (1935).

[51] N. D. Mermin and H. Wagner, *Solid State Physics* (Brooks-Cole, Belmont, 1976).

[52] A. Fasolino, J. Los, and M. Katsnelson, "Intrinsic ripples in graphene", Nature Materials **6**, 858–861 (2007).

[53] J. M. Carlsson, "Graphene: Buckle or break", Nature Materials **6**, 801–802 (2007).

[54] C. H. Lui, Z. Li, Z. Chen, P. V. Klimov, L. E. Brus, and T. F. Heinz, "Imaging stacking order in few-layer graphene", Nano Lett. **11**, 164–169 (2011).

[55] P. Giannozzi, S. Baroni, N. Bonini, M. Calandra, R. Car, *et al.*, "QUANTUM ESPRESSO: a modular and open-source software project for quantum simulations of materials", J. Phys.: Condens. Matter **21**, 395 502 (2009).

[56] S. Piscanec, M. Lazzeri, F. Mauri, A. Ferrari, and J. Robertson, "Kohn anomalies and electron-phonon interactions in graphite", Phys. Rev. Lett. **93**, 185 503 (2004).

[57] M. Cardona, "Resonance phenomena", in *Light Scattering in Solids II*, edited by M. Cardona and G. Güntherodt (Springer, Berlin, 1982), vol. 50 of *Topics in Applied Physics*.

[58] P. H. Tan, W. P. Han, W. J. Zhao, Z. H. Wu, K. Chang, *et al.*, "The shear mode of multi-layer graphene", Nature Materials **advance online publication SP - EP -** (2012), 10.1038/nmat3245.

[59] V. Perebeinos, J. Tersoff, and P. Avouris, "Electron-phonon interaction and transport in semiconducting carbon nanotubes", Phys. Rev. Lett. **94**, 086 802 (2005).

[60] T. Odom, J. Huang, P. Kim, and C. Lieber, "Atomic structure and electronic properties of single-walled carbon nanotubes", Nature **391**, 62–64 (1998).

[61] S. Doorn, P. Araujo, K. Hata, and A. Jorio, "Excitons and exciton-phonon coupling in metallic single-walled carbon nanotubes: Resonance Raman spectroscopy", Phys. Rev. B **78**, 165 408 (2008).

[62] S. Berciaud, C. Voisin, H. Yan, B. Chandra, R. Caldwell, *et al.*, "Excitons and high-order optical transitions in individual carbon nanotubes: A rayleigh scattering spectroscopy study", Phys. Rev. B **81**, 041 414(R) (2010).

[63] S. M. Bachilo, M. S. Strano, C. Kittrell, R. H. Hauge, R. E. Smalley, and R. B. Weisman, "Structure-assigned optical spectra of single-walled carbon nanotubes", Science **298**, 2361 (2002).

[64] J. H. Davies, *Physics of low-dimensional semiconductors* (Cambridge University Press, Cambridge, UK, 1998).

[65] P. Y. Yu and M. Cardona, *Fundamentals of Semiconductors* (Springer, Berlin, 1999, 2nd ed.).

[66] N. Ashcroft and N. D. Mermin, *Solid State Physics* (Brooks-Cole, Belmont, 1976).

[67] V. Perebeinos, J. Tersoff, and P. Avouris, "Mobility in semiconducting carbon nanotubes at finite carrier density", Nano Lett. **6**, 205–208 (2006).

[68] J. Bardeen, L. N. Cooper, and J. R. Schrieffer, "Theory of superconductivity", Phys. Rev. **108**, 1175–1204 (1957).

[69] W. Kohn, "Image of the Fermi surface in the vibration spectrum of a metal", Phys. Rev. Lett. **2**, 393–394 (1959).

[70] S. Piscanec, M. Lazzeri, A. Ferrari, F. Mauri, and J. Robertson, "Kohn anomalies in graphite and nanotubes", Mater. Res. Soc. Symp. Proc. **858E** (2005).

[71] M. Lazzeri, S. Piscanec, F. Mauri, A. Ferrari, and J. Robertson, "Phonon linewidths and electron-phonon coupling in graphite and nanotubes", Phys. Rev. B **73**, 155 426 (2006).

[72] S. Piscanec, M. Lazzeri, J. Robertson, A. Ferrari, and F. Mauri, "Optical phonons in carbon nanotubes: Kohn anomalies, Peierls distortions, and dynamic effects", Phys. Rev. B **75**, 035 427 (2007).

[73] G. D. Mahan, *Many-Particle Physics, 3rd. edition* (Kluwer Academic / Plenum, New York, 2000).

[74] C. V. Raman, "A Change of Wavelength in Light Scattering", Nature **121**, 619 (1928).

[75] F. Cerdeira, E. Anastassakis, W. Kauschke, and M. Cardona, "Stress-induced doubly resonant Raman scattering in GaAs", Phys. Rev. Lett. **57**, 3209–3212 (1986).

[76] S. I. Gubarev, T. Ruf, and M. Cardona, "Doubly resonant Raman scattering in the semimagnetic semiconductor $Cd_{0.95}$ $Mn_{0.05}Te$", Phys. Rev. B **43**, 1551–1554 (1991).

[77] F. Tuinstra and L. J. Koenig, "Raman spectrum of graphite", J. Chem. Phys. **53**, 1126 (1970).

[78] I. Pocsik, M. Hundhausen, M. Koos, and L. Ley, "Raman spectrum of graphite", J. Non-Cryst. Solids **227- 230**, 227–230.

[79] C. Mapelli, C. Castiglioni, G. Zerbi, and K. Müllen, "Common force field for graphite and polycyclic aromatic hydrocarbons", Phys. Rev. B **60**, 12 710–12 725 (1999).

[80] M. J. Matthews, M. A. Pimenta, G. Dresselhaus, M. S. Dresselhaus, and M. Endo, "Origin of dispersive effects of the Raman D band in carbon materials", Phys. Rev. B **59**, R6585–R6588 (1999).

[81] C. Thomsen and S. Reich, "Double resonant Raman scattering in graphite", Phys. Rev. Lett. **85**, 5214–5217 (2000).

[82] A. Ferrari and J. Robertson, "Resonant Raman spectroscopy of disordered, amorphous, and diamondlike carbon", Phys. Rev. B **61**, 075 414 (2001).

[83] A. Grüneis, R. Saito, T. Kimura, L. G. Cançado, M. A. Pimenta, *et al.*, "Determination of two-dimensional phonon dispersion relation of graphite by Raman spectroscopy", Phys. Rev. B **65**, 155 405 (2002).

[84] R. Saito, A. Jorio, A. Souza, G. Dresselhaus, M. Dresselhaus, and M. Pimenta, "Probing phonon dispersion relations of graphite by double resonance Raman scattering", Phys. Rev. Lett. **88**, 027 401 (2002).

[85] J. Maultzsch, S. Reich, and C. Thomsen, "Double-resonant Raman scattering in graphite: Interference effects, selection rules, and phonon dispersion", Phys. Rev. B **70**, 155 403 (2004).

[86] R. Narula and S. Reich, "Double resonant Raman spectra in graphene and graphite: A two-dimensional explanation of the Raman amplitude", Phys. Rev. B **78**, 165 422 (2008).

[87] M. Mohr, J. Maultzsch, and C. Thomsen, "Splitting of the Raman 2D band of graphene subjected to strain", Phys. Rev. B **82**, 201 409 (2010).

[88] P. Venezuela, M. Lazzeri, and F. Mauri, "Theory of double-resonant Raman spectra in graphene: Intensity and line shape of defect-induced and two-phonon bands", Phys. Rev. B **84**, 035 433 (2011).

[89] R. Narula, N. Bonini, N. Marzari, and S. Reich, "Dominant phonon wavevectors of the 2D Raman mode of graphene", phys. stat. sol. (b) **248**, 2635–2638 (2011).

[90] R. Narula, N. Bonini, N. Marzari, and S. Reich, "Dominant phonon wavevectors and strain-induced splitting of the 2D graphene Raman mode", Arxiv preprint:1102.5317v2 (2011).

[91] J. Maultzsch, S. Reich, C. Thomsen, H. Requardt, and P. Ordejon, "Phonon dispersion in graphite", Phys. Rev. Lett. **92**, 075 501 (2004).

[92] D. Mafra, E. Moujaes, S. Doorn, H. Htoon, R. Nunes, and M. Pimenta, "A study of inner process double-resonance Raman scattering in bilayer graphene", Carbon **49**, 1511–1515 (2011).

[93] A. C. Ferrari, J. C, V. Scardaci, C. Casiraghi, M. Lazzeri, *et al.*, "Raman spectrum of graphene and graphene layers", Phys. Rev. Lett. **97**, 187 401 (2006).

[94] J. Kurti, V. Zolyomi, A. Gruneis, and H. Kuzmany, "Double resonant Raman phenomena enhanced by van Hove singularities in single-wall carbon nanotubes", Phys. Rev. B **65**, 165 433 (2002).

[95] F. Rossi and E. Molinari, "Coulomb-induced suppression of band-edge singularities in the optical spectra of realistic quantum-wire structures", Phys. Rev. Lett. **76**, 3642–3645 (1996).

[96] M. Damnjanović, I. Milošević, T. Vuković, and R. Sredanović, "Full symmetry, optical activity, and potentials of single-wall and multiwall nanotubes", Phys. Rev. B **60**, 2728–2739 (1999).

[97] H. Zhao and S. Mazumdar, "Electron-electron interaction effects on the optical excitations of semiconducting single-walled carbon nanotubes", Phys. Rev. Lett. **93**, 157 402 (2004).

[98] F. Wang, G. Dukovic, L. E. Brus, and T. Heinz, "The optical resonances in carbon nanotubes arise from excitons", Science **308**, 838 (2005).

[99] J. Maultzsch, R. Pomraenke, S. Reich, E. Chang, D. Prezzi, *et al.*, "Exciton binding energies in carbon nanotubes from two-photon photoluminescence", Phys. Rev. B **72**, 241 402(R) (2005).

[100] F. Wang, D. Cho, B. Kessler, J. Deslippe, P. Schuck, *et al.*, "Observation of excitons in one-dimensional metallic single-walled carbon nanotubes", Phys. Rev. Lett. **99**, 227 401 (2007).

[101] A. M. Rao, E. Richter, S. Bandow, B. Chase, P. C. Eklund, *et al.*, "Diameter-selective Raman scattering from vibrational modes in carbon nanotubes", Science **275**, 187–191 (1997).

[102] R. A. Jishi, L. Venkata Raman, M. S. Dresselhaus, and D. G., "Phonon modes in carbon nanotubes", Chem. Phys. Lett. **209**, 77 (1993).

[103] J. Kürti, G. Kresse, and H. Kuzmany, "First-principles calculations of the radial breathing mode of single-wall carbon nanotubes", Phys. Rev. B **58**, R8869–R8872 (1998).

[104] L. Henrard, E. Hernández, P. Bernier, and A. Rubio, "Van der Waals interaction in nanotube bundles: Consequences on vibrational modes", Phys. Rev. B **60**, R8521–R8524 (1999).

[105] A. Jorio, R. Saito, J. H. Hafner, C. M. Lieber, M. Hunter, *et al.*, "Structural (n, m) determination of isolated single-wall carbon nanotubes by resonant Raman scattering", Phys. Rev. Lett. **86**, 1118–1121 (2001).

[106] E. Dobardžić, J. Maultzsch, I. Milošević, C. Thomsen, and M. Damnjanović, "The radial breathing mode frequency in double-walled carbon nanotubes: an analytical approximation", phys. stat. sol. (b) **237**, R7– R10 (2003).

[107] C. Fantini, A. Jorio, M. Souza, M. Strano, M. Dresselhaus, and M. Pimenta, "Optical transition energies for carbon nanotubes from resonant Raman spectroscopy: Environment and temperature effects", Phys. Rev. Lett. **93**, 147 406 (2004).

[108] J. C. Meyer, M. Paillet, T. Michel, A. Moréac, A. Neumann, *et al.*, "Raman modes of index-identified freestanding single-walled carbon nanotubes", Phys. Rev. Lett. **95**, 217 401 (2005).

[109] P. Araujo, S. Doorn, S. Kilina, S. Tretiak, E. Einarsson, *et al.*, "Third and fourth optical transitions in semiconducting carbon nanotubes", Phys. Rev. Lett. **98**, 067 401 (2007).

[110] T. Hasan, V. Scardaci, P. Tan, F. Bonaccorso, A. Rozhin, Z. Sun, and A. Ferrari, *Nanotube and Graphene Polymer Composites for Photonics and Optoelectronics* (Springer Science+Business Media, Berlin, 2011).

[111] V. Perebeinos, J. Tersoff, and P. Avouris, "Scaling of excitons in carbon nanotubes", Phys. Rev. Lett. **92**, 257 402 (2004).

[112] T. Ando, "Excitons in carbon nanotubes", Journal of the Physical Society of Japan **66**, 1066–1073 (1997).

[113] T. Pedersen, "Variational approach to excitons in carbon nanotubes", Phys. Rev. B **67**, 073 401 (2003).

[114] C. Kane and E. Mele, "Electron interactions and scaling relations for optical excitations in carbon nanotubes", Phys. Rev. Lett. **93**, 197 402 (2004).

[115] E. Chang, G. Bussi, A. Ruini, and E. Molinari, "Excitons in carbon nanotubes: An ab initio symmetry-based approach", Phys. Rev. Lett. **92** (2004).

[116] C. Spataru, S. Ismail-Beigi, L. Benedict, and S. Louie, "Excitonic effects and optical spectra of single-walled carbon nanotubes", Phys. Rev. Lett. **92**, 077 402 (2004).

[117] V. Perebeinos and P. Avouris, "Impact excitation by hot carriers in carbon nanotubes", Phys. Rev. B **74**, 121 410 (2006).

[118] M. Hugues, B. Damilano, J.-Y. Duboz, and J. Massies, "Exciton dissociation and hole escape in the thermal photoluminescence quenching of (Ga,In)(N,As) quantum wells", Phys. Rev. B **75**, 115 337 (2007).

[119] J. Robertson, G. Zhong, H. Telg, C. Thomsen, J. H. Warner, *et al.*, "Growth and characterization of high-density mats of single-walled carbon nanotubes for interconnects", Appl. Phys. Lett. **93**, 163 111 (2008).

[120] G. Zhong, S. Hofmann, F. Yan, H. Telg, J. H. Warner, *et al.*, "Acetylene: A key growth precursor for single-walled carbon nanotube forests", J. Phys. Chem. C **113**, 17 321–17 325 (2009).

[121] H. Telg, C. Thomsen, and J. Maultzsch, "Raman intensities of the radial-breathing mode in carbon nanotubes: the exciton-phonon coupling as a function of (n_1, n_2)", Journal of Nanophotonics (4), 041 660 (2010).

[122] M. Cardona, T. Meyer, and M. Thewalt, "Temperature dependence of the energy gap of semiconductors in the low-temperature limit", Phys. Rev. Lett. **92**, 196 403 (2004).

[123] R. Capaz, C. Spataru, P. Tangney, M. Cohen, and S. Louie, "Temperature dependence of the band gap of semiconducting carbon nanotubes", Phys. Rev. Lett. **94**, 036 801 (2005).

[124] O. Madelung, *Semiconductors: Group IV Elements and III-V Compounds* (Springer, Berlin, 1991).

[125] R. Capaz, C. Spataru, P. Tangney, M. Cohen, and S. Louie, "Temperature dependence of the band gap of semiconducting carbon nanotubes", Phys. Rev. Lett. **94**, 036 801 (2005).

[126] S. Cronin, Y. Yin, A. Walsh, R. Capaz, A. Stolyarov, *et al.*, "Temperature dependence of the optical transition energies of carbon nanotubes: The role of electron-phonon coupling and thermal expansion", Phys. Rev. Lett. **96**, 127 403 (2006).

[127] J. Deslippe, C. D. Spataru, D. Prendergast, and S. G. Louie, "Bound excitons in metallic single-walled carbon nanotubes", Nano Lett. **7**, 1626–1630 (2007).

[128] P. Schelling and P. Keblinski, "Thermal expansion of carbon structures", Phys. Rev. B **68**, 035 425 (2003).

[129] J. Lefebvre, P. Finnie, and Y. Homma, "Temperature-dependent photoluminescence from single-walled carbon nanotubes", Phys. Rev. B **70**, 045 419 (2004).

[130] E. Malic, J. Maultzsch, S. Reich, and A. Knorr, "Excitonic absorption spectra of metallic single-walled carbon nanotubes", Phys. Rev. B **82**, 035 433 (2010).

[131] K. Sato, R. Saito, J. Jiang, G. Dresselhaus, and M. Dresselhaus, "Discontinuity in the family pattern of single-wall carbon nanotubes", Phys. Rev. B **76**, 195 446 (2007).

[132] C. Spataru, S. Ismail-Beigi, R. Capaz, and S. Louie, "Theory and ab initio calculation of radiative lifetime of excitons in semiconducting carbon nanotubes", Phys. Rev. Lett. **95**, 247 402 (2005).

[133] F. Wang, G. Dukovic, L. Brus, and T. Heinz, "Time-resolved fluorescence of carbon nanotubes and its implication for radiative lifetimes", Phys. Rev. Lett. **92**, 177 401 (2004).

[134] V. Perebeinos, J. Tersoff, and P. Avouris, "Radiative lifetime of excitons in carbon nanotubes", Nano Lett. **5**, 2495–2499 (2005).

[135] H. Telg, J. Maultzsch, S. Reich, and C. Thomsen, "First and second optical transitions in single-walled carbon nanotubes: a resonant Raman study", phys. stat. sol. (b) **244**, 4006–4010 (2007).

[136] J. Jiang, R. Saito, K. Sato, J. Park, G. Samsonidze, *et al.*, "Exciton-photon, exciton-phonon matrix elements, and resonant Raman intensity of single-wall carbon nanotubes", Phys. Rev. B **75**, 035 405 (2007).

[137] M. Steiner, M. Freitag, V. Perebeinos, J. Tsang, J. Small, *et al.*, "Phonon populations and electrical power dissipation in carbon nanotube transistors", Nature Nanotech. **4**, 320–324 (2009).

[138] S. Reich, C. Thomsen, and J. Robertson, "Exciton resonances quench the photoluminescence of zigzag carbon nanotubes", Phys. Rev. Lett. **95**, 077 402 (2005).

[139] B. Schulz, J. Backstrom, D. Budelmann, R. Maeser, M. Rubhausen, *et al.*, "Fully reflective deep ultraviolet to near infrared spectrometer and entrance optics for resonance Raman spectroscopy", Rev. Scientific Instruments **76**, 073 107 (2005).

[140] F. Wang, W. Liu, Y. Wu, M. Sfeir, L. Huang, *et al.*, "Multiphonon Raman scattering from individual single-walled carbon nanotubes", Phys. Rev. Lett. **98**, 047 402 (2007).

[141] Y. Kawashima and G. Katagiri, "Fundamentals, overtones, and combinations in the Raman spectrum of graphite", Phys. Rev. B **52**, 10 053–10 059 (1995).

[142] A. C. Albrecht, R. J. H. Clark, D. Oprescu, S. J. R. Owens, and C. Svendsen, "Overtone resonance Raman scattering beyond the Condon approximation: Transform theory and vibronic properties", The Journal of Chemical Physics **101**, 1890–1903 (1994).

[143] V. Perebeinos, J. Tersoff, and P. Avouris, "Effect of exciton-phonon coupling in the calculated optical absorption of carbon nanotubes", Phys. Rev. Lett. **94**, 027 402 (2005).

[144] M. Machon, S. Reich, H. Telg, J. Maultzsch, P. Ordejon, and C. Thomsen, "Strength of radial breathing mode in single-walled carbon nanotubes", Phys. Rev. B **71**, 035 416 (2005).

[145] D. L. Mafra, L. M. Malard, S. K. Doorn, H. Htoon, J. Nilsson, A. H. C. Neto, and M. A. Pimenta, "Observation of the Kohn anomaly near the K point of bilayer graphene", Phys. Rev. B **80**, 241 414(R) (2009).

[146] P. Blake, E. W. Hill, A. H. C. Neto, K. S. Novoselov, D. Jiang, *et al.*, "Making graphene visible", Appl. Phys. Lett. **91**, 063 124 (2007).

[147] A. Gupta, G. Chen, P. Joshi, S. Tadigadapa, and P. C. Eklund, "Raman scattering from high-frequency phonons in supported n-graphene layer films", Nano Lett. **6**, 2667–2673 (2006).

[148] D. Yoon, H. Moon, Y.-W. Son, J. S. Choi, B. H. Park, *et al.*, "Interference effect on Raman spectrum of graphene on SiO_2/Si", Phys. Rev. B **80**, 125 422 (2009).

[149] A. M. Rappe, K. M. Rabe, E. Kaxiras, and J. D. Joannopoulos, "Optimized pseudopotentials", Phys. Rev. B **41**, 1227 – 1230 (1990).

[150] J. P. Perdew, K. Burke, and M. Ernzerhof, "Generalized Gradient Approximation Made Simple", Phys. Rev. Lett. **77**, 3865 – 3868 (1996).

[151] M. Methfessel and A. T. Paxton, "High-precision sampling for Brillouin-zone integration in metals", Phys. Rev. B **40**, 3616 (1989).

[152] M. Mohr, J. Maultzsch, E. Dobardzic, S. Reich, I. Milosevic, *et al.*, "Phonon dispersion of graphite by inelastic X-ray scattering", Phys. Rev. B **76**, 035 439 (2007).

[153] R. Godby, M. Schlüter, and L. Sham, "Accurate exchange-correlation potential for silicon and its discontinuity on addition of an electron", Phys. Rev. Lett. **56**, 2415–2418 (1986).

[154] K. F. Mak, J. Shan, and T. Heinz, "Seeing many-body effects in single- and few-layer graphene: Observation of two-dimensional saddle-point excitons", Phys. Rev. Lett. **106**, 046 401 (2011).

[155] D. Chae, T. Utikal, S. Weisenburger, H. Giessen, K. Klitzing, M. Lippitz, and J. Smet, "Excitonic Fano resonance in free-standing graphene", Nano Lett. **11**, 1379–1382 (2011).

[156] M. Lazzeri, C. Attaccalite, L. Wirtz, and F. Mauri, "Impact of the electron-electron correlation on phonon dispersion: Failure of LDA and GGA DFT functionals in graphene and graphite", Phys. Rev. B **78**, 081 406(R) (2008).

[157] A. Grueneis, J. Serrano, A. Bosak, M. Lazzeri, S. L. Molodtsov, *et al.*, "Phonon surface mapping of graphite: Disentangling quasi-degenerate phonon dispersions", Phys. Rev. B **80**, 085 423 (2009).

[158] D. Yoon, Y.-W. Son, and H. Cheong, "Strain-dependent splitting of the double-resonance Raman scattering band in graphene", Phys. Rev. Lett. **106**, 155 502 (2011).

[159] A. Das, B. Chakraborty, S. Piscanec, S. Pisana, A. Sood, and A. Ferrari, "Phonon renormalization in doped bilayer graphene", Phys. Rev. B **79**, 155 417 (2009).

[160] Y. Shi, X. Dong, P. Chen, J. Wang, and L.-J. Li, "Effective doping of single-layer graphene from underlying SiO_2 substrates", Phys. Rev. B **79**, 115 402 (2009).

[161] M. Mohr, K. Papagelis, J. Maultzsch, and C. Thomsen, "Two-dimensional electronic and vibrational band structure of uniaxially strained graphene from ab initio calculations", Phys. Rev. B **80**, 205 410 (2009).

[162] S. Berciaud, S. Ryu, L. E. Brus, and T. F. Heinz, "Probing the intrinsic properties of exfoliated graphene: Raman spectroscopy of free-standing monolayers", Nano Lett. **9**, 346–352 (2009).

[163] D. Yoon, H. Moon, Y.-W. Son, G. Samsonidze, B. H. Park, *et al.*, "Strong polarization dependence of double-resonant Raman intensities in graphene", Nano Lett. **8**, 4270–4274 (2008).

[164] D. Mafra, G. Samsonidze, L. Malard, D. Elias, J. Brant, *et al.*, "Determination of LA and TO phonon dispersion relations of graphene near the dirac point by double resonance Raman scattering", Phys. Rev. B **76**, 233 407 (2007).

[165] D. M. Basko, "Theory of resonant multiphonon Raman scattering in graphene", Phys. Rev. B **78**, 125 418 (2008).

[166] D. M. Basko, S. Piscanec, and A. C. Ferrari, "Electron-electron interactions and doping dependence of the two-phonon Raman intensity in graphene", Phys. Rev. B **80**, 165 413 (2009).

[167] E. Malic, T. Winzer, E. Bobkin, and A. Knorr, "Microscopic theory of absorption and ultrafast many-particle kinetics in graphene", Phys. Rev. B **84**, 205 406 (2011).

[168] E. Malić, M. Hirtschulz, F. Milde, A. Knorr, and S. Reich, "Analytical approach to optical absorption in carbon nanotubes", Phys. Rev. B **74**, 195 431 (2006).

[169] L. G. Cancado, A. Reina, J. Kong, and M. S. Dresselhaus, "Geometrical approach for the study of G' band in the Raman spectrum of monolayer graphene, bilayer graphene, and bulk graphite", Phys. Rev. B **77**, 245 408 (2008).

Acknowledgments

This work would not have been possible without the help of many people. I would like to thank specially...

my advisor Prof. Dr. Janina Maultzsch, whose encouragement, guidance and support from the initial to the final level allowed me to get a deeper understanding of the carbon world. Thank you for your excellent supervision.

Prof. Dr. Konstantinos Papagelis for reviewing this thesis and for traveling the long way to the defense.

Prof. Dr. Michael Lehmann for being the chairman of my thesis committee.

Prof. Dr. Christian Thomsen for support and the outstanding collaboration.

Prof. Dr. Milan Damnjanović and his group for continuous exchange. I really enjoyed the time in Belgrade.

Prof. Dr. John Robertson and G. Zhong for the fruitful scientific collaboration.

Prof. Dr. Michael Rübhausen and his group for the lab-time at the UT3 in Hamburg.

Prof. Dr. F. Mauri for providing and sharing data concerning the two-dimensional calculation of the double-resonance in graphene.

Dr. Hagen Telg for introducing me to the world of resonant Raman spectroscopy.

Dr. Marcel Mohr for the calculation of the electronic bandstructures.

Dr. Ermin Malic for the calculation of the optical matrix elements.

Dr. Holger Lange for proofreading parts of this thesis.

Felix Herziger for the preparation of free-standing graphene, for providing a continuous support of SiO_2 substrates with trenches and for some good measurments.

Sebas Reparaz and Gordon Callsen for numerous mutually lab times.

Anja Saathoff for her help in surviving the bureaucracy.

All the colleagues in the groups of Thomsen, Maultzsch, and Hoffmann for the great atmosphere.

Special thanks go to my room mates Jan and Mastaiger for having lots of fun during the last months and years.

Eidesstattliche Versicherung

Hiermit erkläre ich an Eides statt, dass ich die vorliegende Dissertation "*Electronic and vibrational properties of low-dimensional carbon systems*" selbständig verfasst sowie die benutzten Quellen und Hilfsmittel vollständig angegeben habe. Teile der Dissertation wurden schon veröffentlicht.

Berlin, 3rd May 2012

Patrick May
Eichendorffstr. 20
10115 Berlin